A photon counting pixel detector for X-ray imaging

John Watt

Experimental Particle Physics Group
Detector Development Laboratory
Dept. of Physics and Astronomy
University of Glasgow
Glasgow
G12 8QQ

Thesis submitted for the degree of Doctor of Philosophy

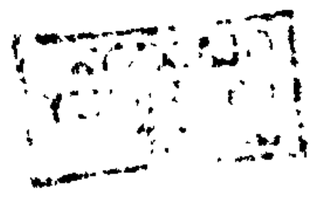

Abstract

Hybrid semiconductor pixel detector technology is presented in this thesis as an alternative to current imaging systems in medical imaging and synchrotron radiation applications. The technology has been developed from research performed in High Energy Physics, in particular, for the ATLAS experiment at the LHC, planned for 2005. This thesis describes work done by the author on behalf of the MEDIPIX project, a collaboration between 13 international institutions for the development of hybrid pixel detectors for non-HEP applications.

Chapter 1 describes the motivation for these detectors, the origin of the technology, and the current state of the art in imaging devices. A description of the requirements of medical imaging on X-ray sensors is described, and the properties of film and CCDs are discussed. The work of the RD19 collaboration is introduced to show the evolution of these devices. Chapter 2 presents the basic semiconductor theory required to understand the operation of these detectors, and a section on image theory introduces the fundamental parameters which are necessary to define the quality of an imaging device.

Chapter 3 presents measurements made by the author on a photon counting detector (PCD1) comprising a PCC1 (MEDIPIX1) readout chip bump-bonded to silicon and gallium arsenide pixel detectors. Tests on the seperate readout chip and the bump-bonded assembly are shown with comparisons between the performance of the two materials. Measurements of signal-to-noise ratio, detection efficiency and noise performance are presented, along

with an MTF measurement made by the Freiburg group. The X-ray tube energy spectrum was calibrated by REGAM.

The performance of the PCD in a powder diffraction experiment using a synchrotron radiation source is described in chapter 4. This chapter reports the first use of a true 2-D hybrid pixel detector in a synchrotron application, and a comparison with the existing scintillator based technology is made. The measurements made by the author have been presented at the 1st International Workshop on Radiation Imaging Detectors at Sundsvall, Sweden, June 1999.

The PCD1 operates in single photon counting mode, which attempts to overcome the limitations of charge integrating devices such as CCDs. The pros and cons of the two detection methods are discussed in chapter 5, and a comparison was made of the PCD1 performance with the performance of a commercial dental X-ray sensor. The two detectors are compared in terms of contrast and signal-to-noise ratio for identical X-ray fluences. The results were presented at the 2nd International Workshop on Radiation Imaging Detectors, Freiburg, Germany, 2nd-6th July 2000.

The author was involved in the conversion of the LabWindows MRS software to a LabView platform, which was presented in an MSc. thesis in the University of Glasgow by F. Doherty. All image processing, data manipulation and analysis code was written by the author.

Contents

Contents

List of Figures

List of Tables

Preface

The photon counting detector studied in this thesis was developed within the framework of the MEDIPIX collaboration, formed by CERN, the Universities of Glasgow (Scotland); Freiburg (Germany); and INFN Pisa and Napoli (Italy). The collaboration has expanded over the past three years to 13 institutions. The detector was realised from technology developed by the CERN RD19 collaboration (established 1990), which also included the University of Glasgow. The results in this thesis are presented also as part of the XIMAGE project, supervised by Dr. C. Fröjdh of REGAM, Sweden.

The initial characterisation and wafer probing carried out at CERN was performed in collaboration with Drs. E. Heijne and M. Campbell of the CERN Microelectronics group. Wafer probing was also performed at NIKHEF, Amsterdam under the guidance of Dr. J. Visschers.

The synchrotron radiation studies presented in this thesis would not have been possible without the aid of Drs. G. Derbyshire and M. Roberts of Daresbury Laboratory, Cheshire, England. The synchrotron work was presented at the 1st International Workshop on Radiation Imaging Detectors in Sundsvall, Sweden in June 1999.

The experiments comparing photon counting and charge integrating systems were presented at the 2nd International Workshop on Radiation Imaging Detectors in Freiburg im Breisgau, Germany in July 2000.

The author wishes to acknowledge the support of EPSRC and Rutherford Appleton Laboratory for their CASE studentship, without whom this work would never have been carried out.

Acknowledgements

I would like to thank Prof. David Saxon for accepting me into the Experimental Particle Physics group of the Department of Physics and Astronomy at Glasgow. I gratefully acknowledge the financial assistance of EPSRC and a CASE award from RAL, UK.

I must begin by thanking my supervisor Professor Kenway Smith for accepting me as one of his research students back in June 1997. Always a source of suggestions, ideas and encouragement, his high standard of supervision and expertise has ensured the success of my studies as well as the success of the collaboration as a whole. In his role as my backup supervisor, Dr. Rick St.Denis has been an enthusiastic champion of the HEP aspects of the project, which is gratefully acknowledged.

In Glasgow, I would like to thank Val O'Shea and Richard Bates for their help with hardware and suggestions for measurements. Thanks to Fred Docherty, Drew Meikle and the rest of the technical staff for the smooth running of things, and also thanks to Spyros Manolopoulos, now of RAL, for all his help in the early stages. I have to thank the group secretary Catherine MacIntyre for her tireless help in dealing with the travel and finance people. I also wish to acknowledge the help of the late Colin Raine in introducing me to setting up the hardware for MEDIPIX, and interfacing systems in general, which has become a large part of my current employment responsibilities. Finally, thanks to Steve Passmore, Steve Devine, Liam Cunningham and Julien Marchal, not forgetting Lee Curtis for the LATEX help, and Stan Thompson for C debugging and Tennents at 5 on Fridays.

During stays in Geneva, I was lucky enough to work with Michael Campbell, the chief designer of the MEDIPIX, who managed to elevate a sideline project into one of the most promising R & D spinoffs at CERN. Many thanks to Bettina Mikulec for her help (especially at Daresbury) and sharing her thorough knowledge of the subject. Elena Pernigotti was a great help when I first joined the project, and a mention must go to Iztok, Paul, Eugenio, Cinzia and everyone else in Building 14. In the Freiburg group, many thanks to Christoph Schwarz and Prof. Jens Ludwig for device data. At NIKHEF in Amsterdam, I want to thank Dr. Jan Visschers for his hospitality (and letting me rifle through his record collection!) and David Calvet for his help with the probe station. I also must thank Prof. Stanislav Pospisil of the Czech Technical University in Prague, for his hospitality on my two very enjoyable visits.

Finally I would like to cheer my office mates Keith Mathieson and Craig Whitehill, who have made the last 4 years as educational, entertaining and friendly as I could have hoped for. I don't think i'll ever forget the piano bar in Sundsvall, vegetarian chicken in Istanbul, absinthe in the Chapeau Rouge, and mini-karting round a hotel's underground car park in Prague at 2am.

The following people have definitely earned a big shout: Steve, Iain, Stu, Nik, Jane, Sue, Nikki, DJ MJC and Nicole, Rachel, Nicola, Letti, Alison, Jean, Raymond, Caroline, Chris and everyone at Kymata. Big up to the Wavemaker guys and HoustonStarlaw...

This thesis is dedicated to Kate, Michael, Christopher and the rest of my family.

Except where explicit reference is made to the work of others, this dissertation is the result of my own work. None of this material has been submitted for any other degree at the University of Glasgow or any other institution.

John Watt

"The past was eagle-eyed, the future's pixellised..."
- Super Furry Animals, "Frisbee".

Chapter 1

Introduction

The detection of light has been of utmost importance to mankind since his first appearance on Earth. Up until the end of the 19^{th} century, humans have relied on the only photon detector available to them - the eye. The human eye is a highly pixellated, extremely sensitive imaging device, equipped with over 10^8 pixels, with a spatial resolution of down to 2 μm [1]. Together with high spectral resolution (colour separation), these features are very attractive in a photon imaging device. It is also interesting to note that as recently as the 1920's, the first experiments in gamma coincidence carried out by Geiger and Rutherford employed the eye as their detecting medium [2][3].

During the 19^{th} Century, the invention of the photographic plate allowed man to *record* images for the first time and store them indefinitely. The discovery that these plates were also sensitive to X-ray photons and some charged particles heralded the beginning of radiography which was to revolutionise diagnostic medicine in the 20^{th} Century. Photographic emulsions are still in use today, but are being replaced by more sensitive, digital imaging systems. These new sensors eliminate the need for processing, purchasing of chemicals, availability of dark rooms etc.

CCDs (Charge Coupled Devices) represent the state of the art in medical imaging and commercial cameras at the end of the 20^{th} century. The high spatial resolution, quick readout, and the large areas achievable at reasonable

cost make them desirable as all purpose imaging devices. There is, however, a fundamental limit on the minimum dose for these devices to form useful images. The aim of this thesis is to introduce the Photon Counting Detector (PCD), which will be presented as a candidate for the next generation of imaging sensors that will improve upon the performance of CCD-based technology [4]. This new sensor has its roots in high energy physics,whose requirements, although more stringent, are similar to the requirements of medical imaging.

1.1 Medical imaging

In medicine, two diagnostic imaging techniques are widely used [5]:

- **X-ray radiology** Patient is illuminated with an X-ray beam and an image of the absorption of the photons in different parts of the body is taken.
- **Nuclear medicine** Patient is injected with a drug with a radioactive tracer (gamma emitting isotope). This drug is chosen to match the metabolism of the subject organ, and an image of the distribution of the isotope is recorded.

Autoradiography is a technique used in biological research in order to detect the distribution and measure the quantity of a radioisotope that is detected in a specimen. This is commonly used in imaging the internal structure and processes within cells.

Within X-ray radiology, there are many different types of imaging modes (mammography, dental, chest). *Digital radiography* allows for different types of imaging techniques, the most important being subtraction imaging.

Subtraction angiography may be performed in two ways. *Digital subtraction angiography*(DSA) is a technique where an initial image of the region of interest is taken before the introduction of an iodinated contrast agent. This is used as a mask for subtraction from the contrast agent enhanced

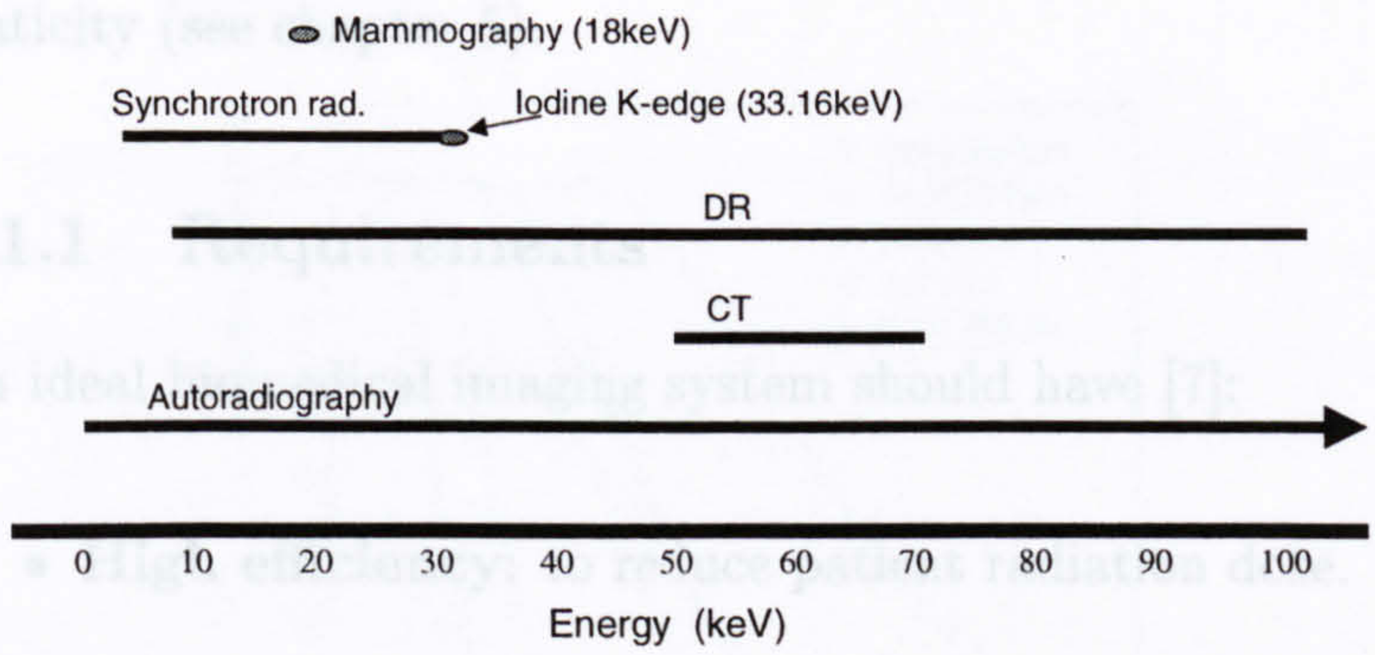

Figure 1.1: X-ray energy range for most medical imaging modalities. (DR - Digital radiology; CT - Computed Tomography.)

image. In this way, the blood vessels may be distinguished from the complex tissue background. In a similar way, *Dual-subtraction angiography* involves the acquisition of two images taken with two different radiopharmaceuticals labelled with different radioisotopes.

Computed tomography (sometimes known as a CAT scan) allows a 3-D image of a patient to be reconstructed from multiple X-ray images. A CT scanner consists of a rotating frame of 60-70cm diameter, with the X-ray tube mounted on one side, and detectors mounted on the other. In each 360^o rotation, about 1000 profiles are sampled. Each profile is back-projected to reconstruct a slice through the patient's body. State of the art systems can collect 4 whole slices of data in 350ms, so a full chest scan can be done in 5 seconds.

Figure 1.1 [6] shows the different methods ordered according to X-ray energy. Most nuclear medicine applications (mainly PET (Positron Emission Tomography) and SPECT (Single Photon Emission Computed Tomography)) are above the 100keV point up to 511keV, however autoradiography covers almost the whole spectrum with many useful radioisotopes (I^{125} at 35keV for example). Synchrotron radiation sources are at present not available in hospitals, but are the ideal X-ray source due to their high monochro-

maticity (see chapter 5).

1.1.1 Requirements

An ideal biomedical imaging system should have [7]:

- **High efficiency**: to reduce patient radiation dose.
- **Good resolution**: though typically not less than 50μm (mammography).
- **Large area**: ideally as large as the imaged object.
- **Linear dynamic range**: no fog at low dose (or saturation at high dose).
- **Low noise**: to eliminate false diagnoses.

The spatial resolution required for applications such as mammography and dental radiography is governed by the size of microcalcifications that need to be found at as early a stage as possible. In mammography, a pixel size of 50μm is by far enough to detect a microcalcification which may develop later into a breast tumour. For angiography, around 200μm will suffice. The primary concern is the reduction of dose to the patient, which may be achieved through the use of materials with high detection efficiencies. Figure 1.2 shows the absorption efficiencies of different materials as a function of incident photon energy. GaAs looks promising as a semiconductor detector because of its high efficiency at low energy. CdTe is a candidate for future detectors when the homogeneity and cost become more viable.

Medical imaging is still dominated by the use of film for X-ray radiology. Film is a *charge integrating* system, where the total signal induced by incident radiation is accumulated in regions of the sensor with no information on the nature of the incoming radiation.

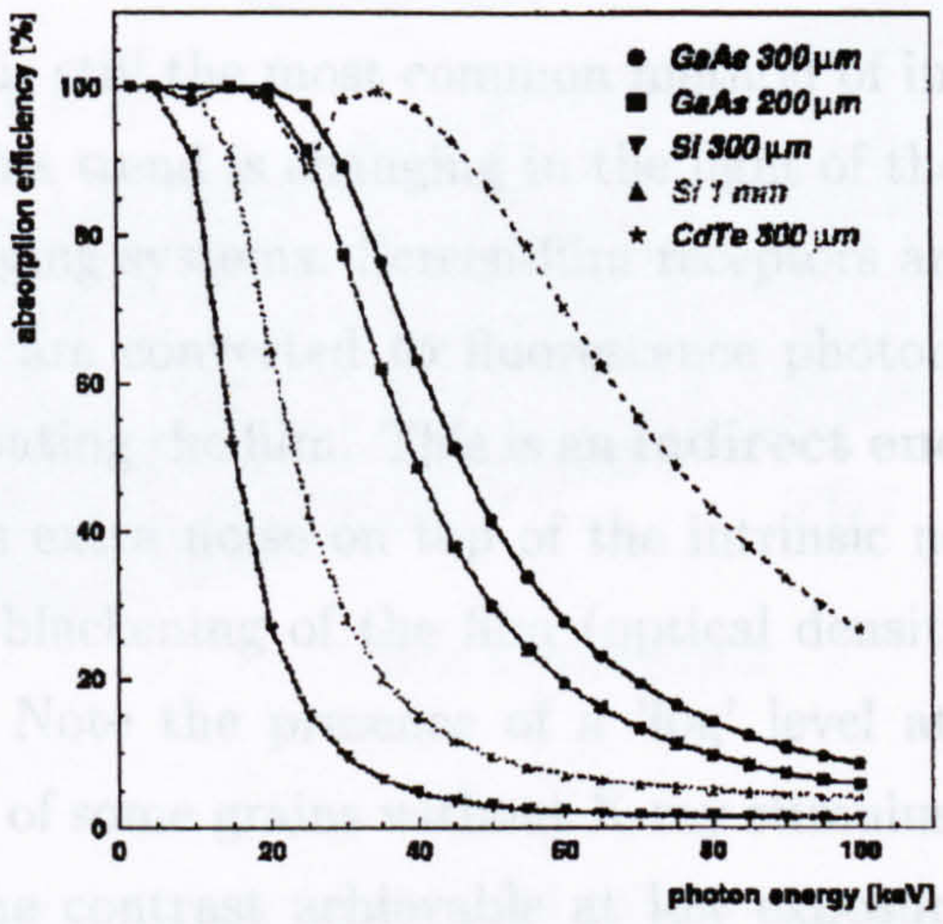

Figure 1.2: Absorption efficiencies of various media in the X-ray radiology range [50]

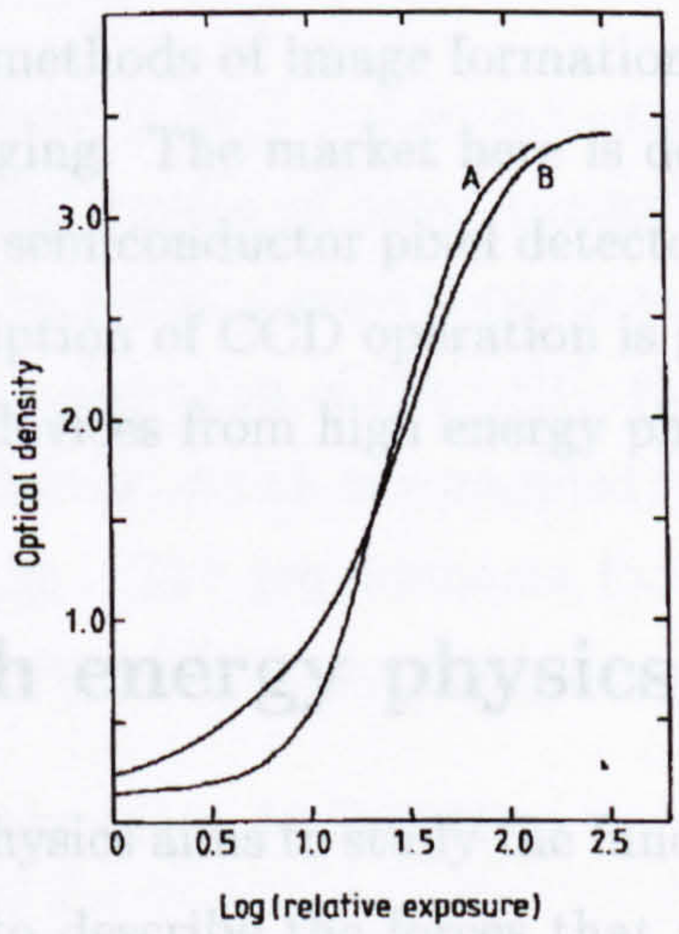

Figure 1.3: Characteristic curve for direct-exposure X-ray film (A) and a screen-film system (B) [5]

1.1.2 Film

X-ray film is still the most common method of image formation and display, although this trend is changing in the light of the cheap availability of CCD digital imaging systems. Screen-film receptors are the most common, where the X-rays are converted to fluorescence photons through active phosphor particles coating the film. This is an **indirect energy conversion** technique which adds extra noise on top of the intrinsic noise of the film. Figure 1.3 shows the blackening of the film (optical density) as a function of relative exposure. Note the presence of a 'fog' level at zero exposure due to the blackening of some grains without X-ray stimulus, which fixes a fundamental limit on the contrast achievable at low exposure. The digitisation of film also introduces more noise to the image, which becomes problematic at low dose [5]. The absorption efficiency of film is very low (about 5%), requiring relatively high doses compared to digital methods to achieve useful contrast.

1.1.3 Digital imaging

Faster, digital methods of image formation are beginning to gain popularity in medical imaging. The market here is dominated by the use of CCD sensors, which are semiconductor pixel detectors operating in charge integration mode. A description of CCD operation is given in section 1.3, where related pixel detector devices from high energy physics are introduced.

1.2 High energy physics detectors

High Energy Physics aims to study the fundamental building blocks of matter and attempts to describe the forces that act between them. The Standard Model of particle physics successfully describes physical processes down to a very small scale, and has survived every experimental test so far. However, it predicts the existence of some particles that cannot be observed with current technology. To test these predictions, bigger, higher energy machines must

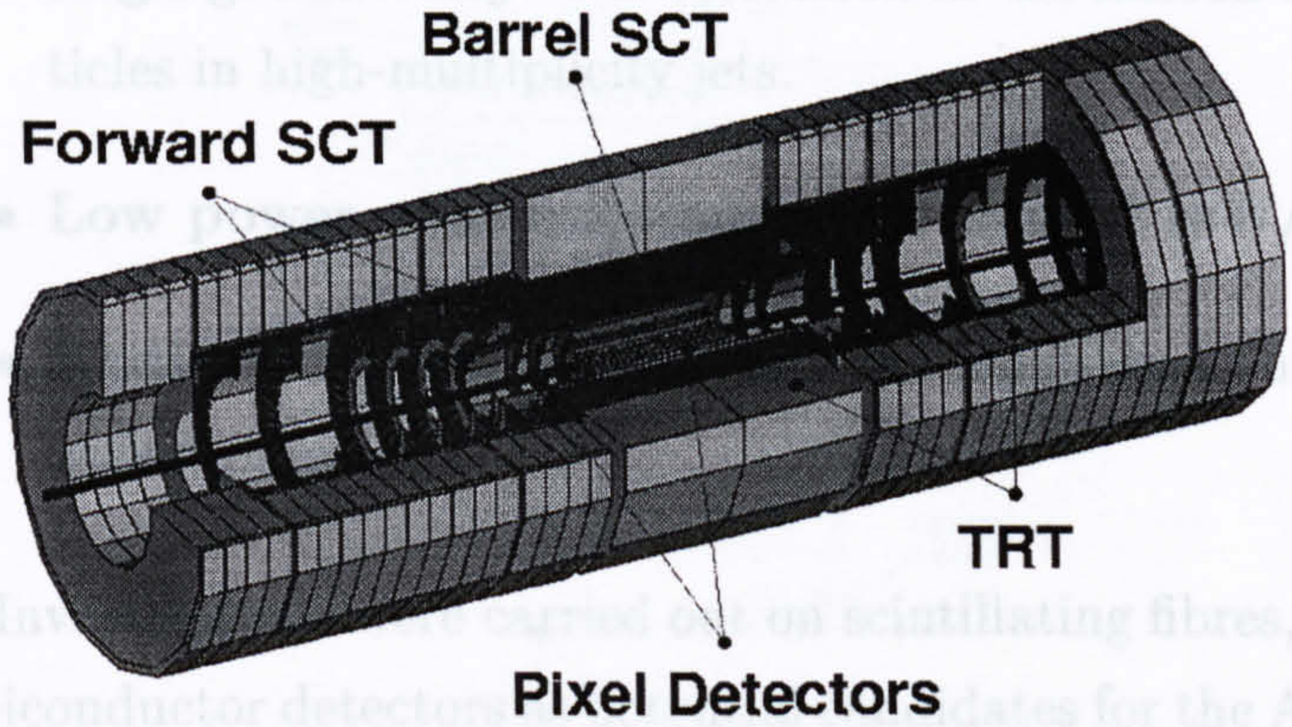

Figure 1.4: The inner detector for the ATLAS experiment at the LHC collider [8]

be made either to confirm theoretical calculations, or point the way to new physics.

1.2.1 Requirements

The Large Hadron Collider (LHC) is due to be completed in 2005, and will collide protons at a total centre of mass energy of 14 TeV. The ATLAS Collaboration [8] aims to build a general-purpose p-p detector designed to exploit the full discovery potential of the LHC. Figure 1.4 shows a diagram of the ATLAS inner detector, which is contained within a cylinder of length 6.8 m and radius 1.15 m. The requirements for the SCT pixel detectors, which are located approximately 10 cm away from the beam, are as follows:

- **High speed**: in the range 10-100MHz.
- **Large area**: to give full coverage around the interaction point (hermiticity).
- **Low mass**: to reduce the amount of material in the semiconductor tracker.

- **High granularity**: 3-D resolution in the micron range to resolve particles in high-multiplicity jets.
- **Low power consumption**: of the order of $1kW/m^2$.
- **Radiation hard**: to cope with the harsh environment near the interaction point.

Investigations were carried out on scintillating fibres, drift chambers, and semiconductor detectors as potential candidates for the ATLAS inner tracker. The requirements listed above were most effectively met by semiconductor pixel detectors [9], the design of which was the focus of the CERN RD19 collaboration.

1.3 Pixel detectors

Semiconductor detectors operate by sensing the charge generated in the semiconductor material when an ionising particle is incident on it. By segmenting the detector, one can reconstruct in two dimensions the position of the incident particle. The details of the operation of these devices are presented in chapter 2. The detector may be realised in two ways: **monolithic**, where the readout electronics are fabricated on the detector material (as in the case of CCDs), or **hybrid** where the detecting pixel material is connected to separate readout electronics through some sort of conducting metal bond. The design of the detectors and readout chips are presented in chapter 3, but an overview of the device characteristics is necessary at this point.

1.3.1 Charge coupled devices (CCDs)

CCDs are essentially monolithic semiconductor detectors, as the electronics and detecting material are on the same material, however CCDs do not have the degree of on-pixel logic that monolithic pixel detectors have. This simplicity means CCDs have very good spatial resolution, usually of the

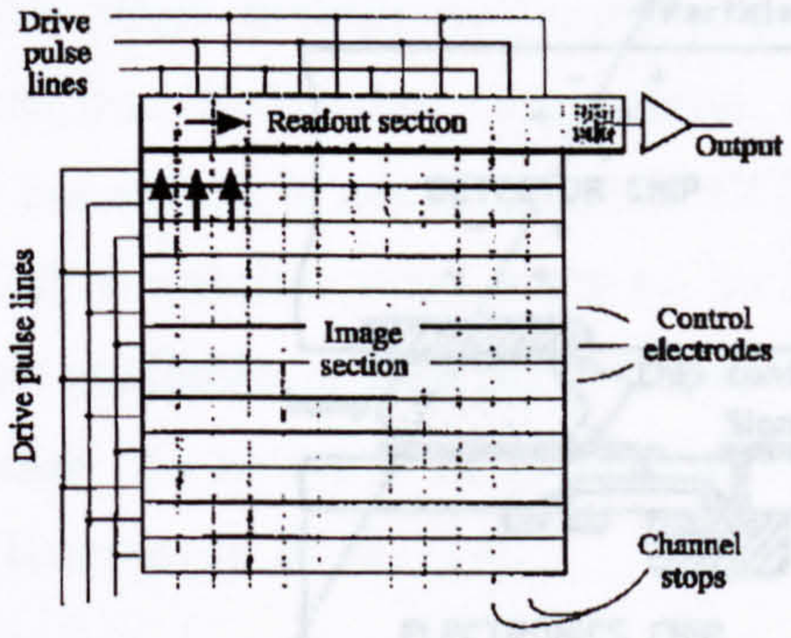

Figure 1.5: Layout of the surface of a charge coupled device (CCD) [10]

order of 25μm pixel size. Figure 1.5 shows the layout of a typical CCD [10]. They are normally fabricated on silicon a few hundred microns thick, with dimensions of 1-2cm on a side. An applied voltage forms a depletion region just below the surface, causing individual potential wells to be created for each pixel. Any free electrons liberated by the passage of ionising radiation within that pixel are accumulated in the well. The device is read out by clocking voltages along the drive pulse lines which 'tip' the well in a preferred direction. One row is read out in this way, and then the rows clocked upward for the next row to be read out. The charge transfer efficiency is very good even with thousands of transfers, however the read out speed is typically slower than hybrid systems (order of ms).

CCDs are susceptible to leakage current which is seen by all pixels. This manifests itself as a 'fog' level analogous to that of film, placing a limit on the image contrast at low dose. The analogue output is more easily digitised than film, allowing digital radiography to be efficiently performed, although the process of digitisation itself always introduces a 'filtering' effect. Solutions to some of these problems have been addressed by detectors for high energy physics, the technology for which will now be introduced.

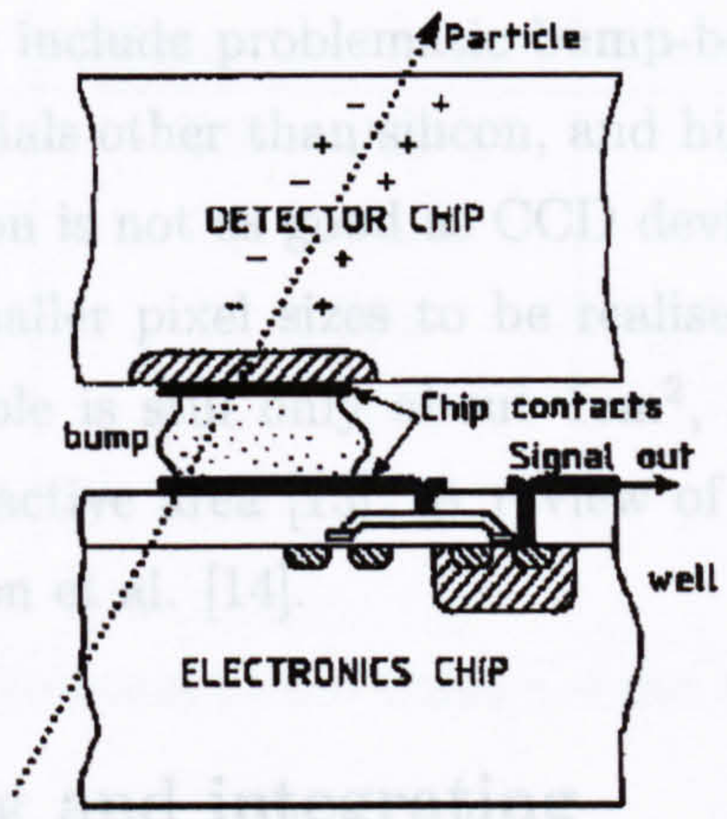

Figure 1.6: Schematic of a hybrid semiconductor pixel detector [11]

1.3.2 Hybrid semiconductor pixel detectors

Figure 1.6 shows a basic schematic of the operation of a hybrid semiconductor detector, with electron-hole pairs being generated in the material, and the motion of these charges sensed at the detector electrode. The signal then passes through a bump-bond to the readout chip bump pad, where a preamp amplifies the signal for subsequent processing by the electronics [11]. Hybrid pixel detectors have many advantages which make them attractive for varied applications [12]:

- Choice of detecting medium (Si, GaAs or others depending on architecture)
- Fast readout of electronics (dependent on size and number of pixels - typically less than 0.5ms)
- Leakage current insensitive logic (no fog level)
- Separate optimisation and testing of detector and electronics (better yield of completed assemblies)
- Single photon counting (Linear and extendable dynamic range)

Disadvantages at this stage include problematic bump-bonding, lack of completely homogeneous materials other than silicon, and high bias voltage operation. The spatial resolution is not as good as CCD devices, but better CMOS processes will allow smaller pixel sizes to be realised (PCC2 - see conclusions). The area available is still only about 1cm^2, although tiling several chips will increase the active area [13]. A review of bump-bonding technology is given in Humpston et al. [14].

1.3.3 Photon counting and integrating

As mentioned before, there are two methods of acquiring an image from the detection of incoming particles: photon counting; and charge integration. Photon counting is achieved by tagging all events that are sensed by the readout electronics, provided the signal exceeds a preset threshold. In this way, each photon above a certain energy is registered as an event. Charge integration works by collecting all the charge generated by incident radiation over a preset period of time. This method allows for smaller pixel sizes at the expense of low dose sensitivity and lack of ability to exclude unwanted parts of the X-ray spectrum.

An investigation of the comparison between integrating and photon counting systems will be made later in this thesis (chapter 5).

1.3.4 The RD19 collaboration

The design of pixel detectors for LHC experiments was the focus of the CERN RD19 collaboration [15]. The realisation of a pixellated, two-dimensional silicon sensor was considered a dream in 1988 [16]. From 1991, the Omega series of readout chips utilised state-of-the-art VLSI technology to produce pixel detectors with small cell size, high uniformity, fast electronics and large area coverage. Table 1.3.4 shows the evolution of the Omega series over the last ten years [17]. The work of the collaboration culminated in the LHC1/Omega3 chip in 1995. The success of this chip in experiments led

	year	cell size [μm $\times$ μm]	transistors/cell	matrix
LAA	1988	200 $\times$ 200	40	9 $\times$ 12
OmegaD	1991	75 $\times$ 500	81	16 $\times$ 63
Omega2	1993	75 $\times$ 500	81	16 $\times$ 63
Omega3/LHC1	1995	50 $\times$ 500	395	16 $\times$ 127
PCC1	1997	170 $\times$ 170	400	64 $\times$ 64

Table 1.1: Evolution of the Omega series readout chips

to the reshaping of the pixels and functionality to create a two-dimensional matrix of square pixels suitable for object imaging. The PCC1 appeared in 1997, and has been successfully bump-bonded to several detector materials. The evaluation of such hybrid pixel detectors forms the basis for the work presented by the author in the following chapters.

Chapter 2

Theory

The theory of semiconductor device operation and image characterisation is described in the following chapter. Semiconductor properties [18] and a description of basic semiconductor devices [19] will be followed by a summary of photon interactions and the collection of charge in the material. A section on the types of material studied in this thesis will be presented and, finally, two sections on the fundamental principles of imaging describe some of the important parameters necessary for the characterisation of any X-ray detector system.

2.1 Semiconductors

Solid state materials are generally grouped into three types depending on their electrical conductivity σ (and resistivity $\rho \equiv \sigma^{-1}$). Insulators and conductors comprise a set of materials with, respectively, low and high conductivity, and semiconducting materials are found in the conductivity region between these two. The conductivity of a semiconductor is sensitive to external effects such as temperature, illumination, magnetic field and impurities, making it one of the most important classes of materials for electronics.

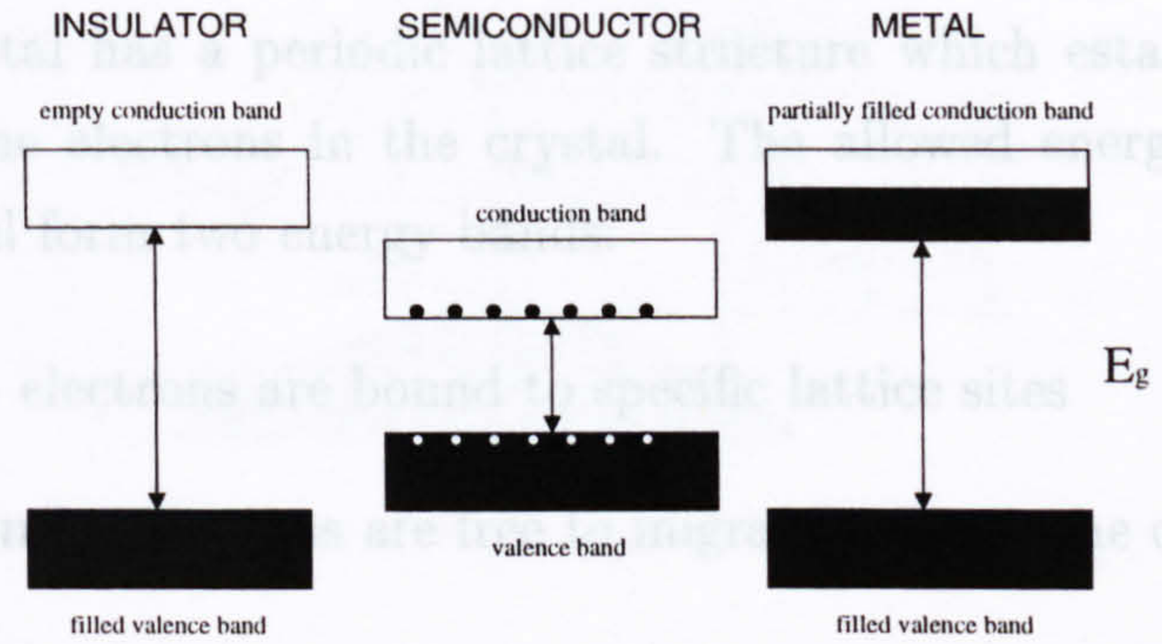

Figure 2.1: Energy band schematics for metals, insulators and semiconductors.

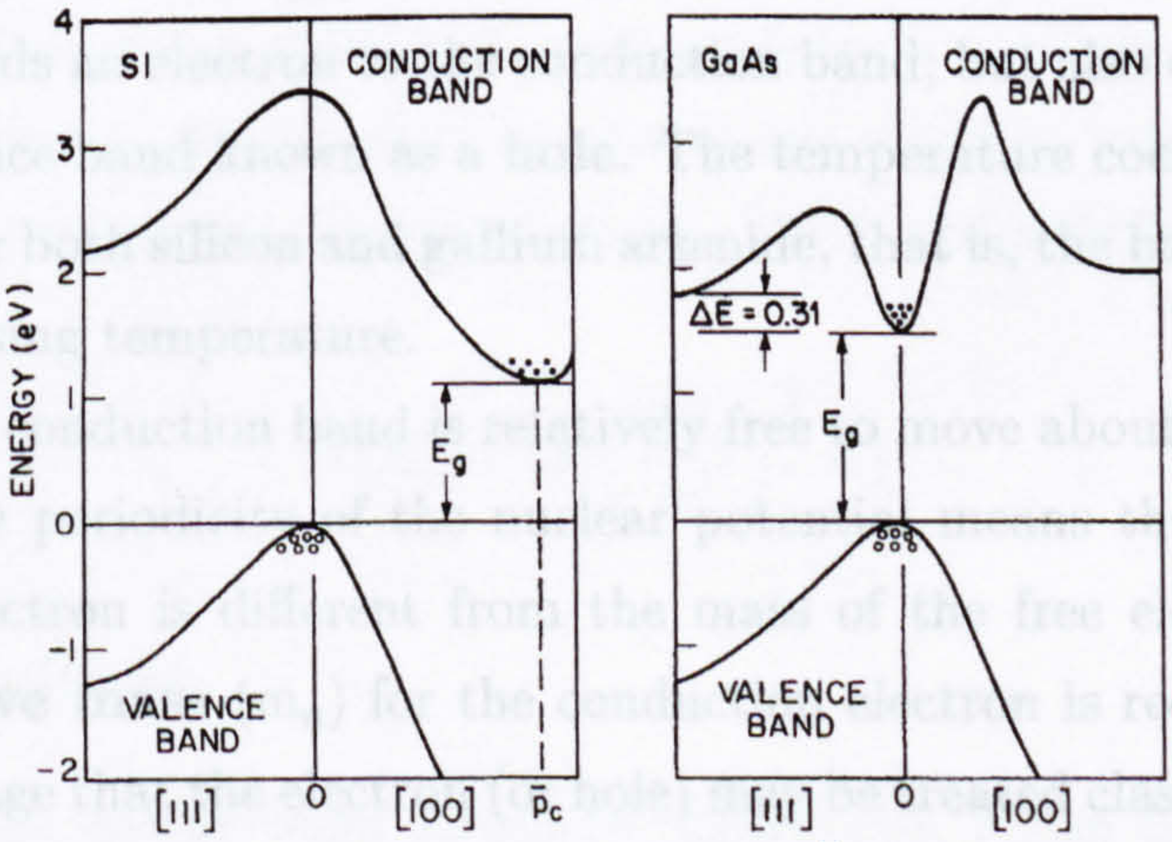

Figure 2.2: Energy band structure for (a) Si and (b) GaAs. Circles indicate holes in the valence band, and dots indicate electrons in the conduction bands. [18]

2.1.1 Energy bands

A semiconductor crystal has a periodic lattice structure which establishes certain energies for the electrons in the crystal. The allowed energies for electrons in the crystal form two energy bands:

- **valence band** - electrons are bound to specific lattice sites
- **conduction band** - electrons are free to migrate through the crystal

The separation between these two bands is known as the *bandgap*, E_g, and is the defining property of the material. Figure 2.1 shows a representation of these energy bands for metals, semiconductors and insulators. In an insulator (and semiconductor), the valence band is just filled by the electrons in the crystal, and in the absence of thermal excitation would theoretically show no electrical conductivity. However, if an electron receives enough energy, it may be elevated across the bandgap and be available for conduction. This excitation not only adds an electron to the conduction band, but also creates a vacancy in the valence band known as a **hole**. The temperature coefficient dE_g/dT is negative for both silicon and gallium arsenide, that is, the bandgap decreases with increasing temperature.

An electron in the conduction band is relatively free to move about in the material, however the periodicity of the nuclear potential means the mass of the conduction electron is different from the mass of the free electron. Therefore, an **effective mass** (m_n) for the conduction electron is required, which has the advantage that the electron (or hole) may be treated classically. The energy-momentum relation for a conduction band electron may be given by the classical expression:

$$E = \frac{\bar{p}^2}{2m_n} \tag{2.1}$$

where $\bar{p}$ is the **crystal momentum**, which is analogous to the particle momentum for a free electron. A similar expression may be written for holes (with effective mass m_p). Figure 2.2 [18] shows the energy band diagrams

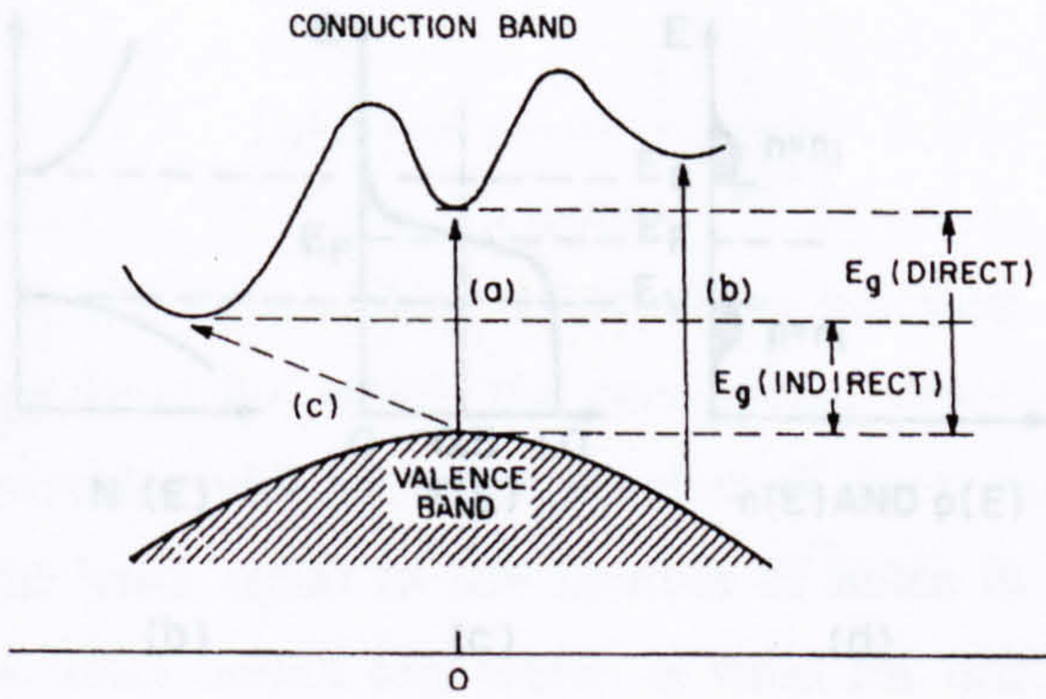

Figure 2.3: Optical transitions: (a) and (b) direct transitions; (c) indirect transition involving lattice vibrations (phonons). [19]

for Si and GaAs where energy is plotted against crystal momentum for two crystal directions.

Because the movements of electrons may be described by standing wave oscillations (periodicity of lattice), we may define a quantity that describes the whereabouts of allowed energy states in one standing wave period. This quantity is known as the *density of states* , N(E), and is defined as:

$$N(E) = 4\pi \left(\frac{2m_n}{h^2}\right)^{\frac{3}{2}} E^{\frac{1}{2}} \tag{2.2}$$

Optical transitions

Considering the energy band structure (figure 2.2), it can be seen that for silicon, the minimum of the conduction band occurs at a different crystal momentum value than the maximum of the valence band. Silicon is said to be an **indirect bandgap semiconductor**. In GaAs, the maximum of the valence band and minimum of the conduction band occur at the same crystal momentum value, and so GaAs is known as a **direct bandgap semiconductor**. Figure 2.3 [19] shows some of the transitions possible between the valence and conduction bands.

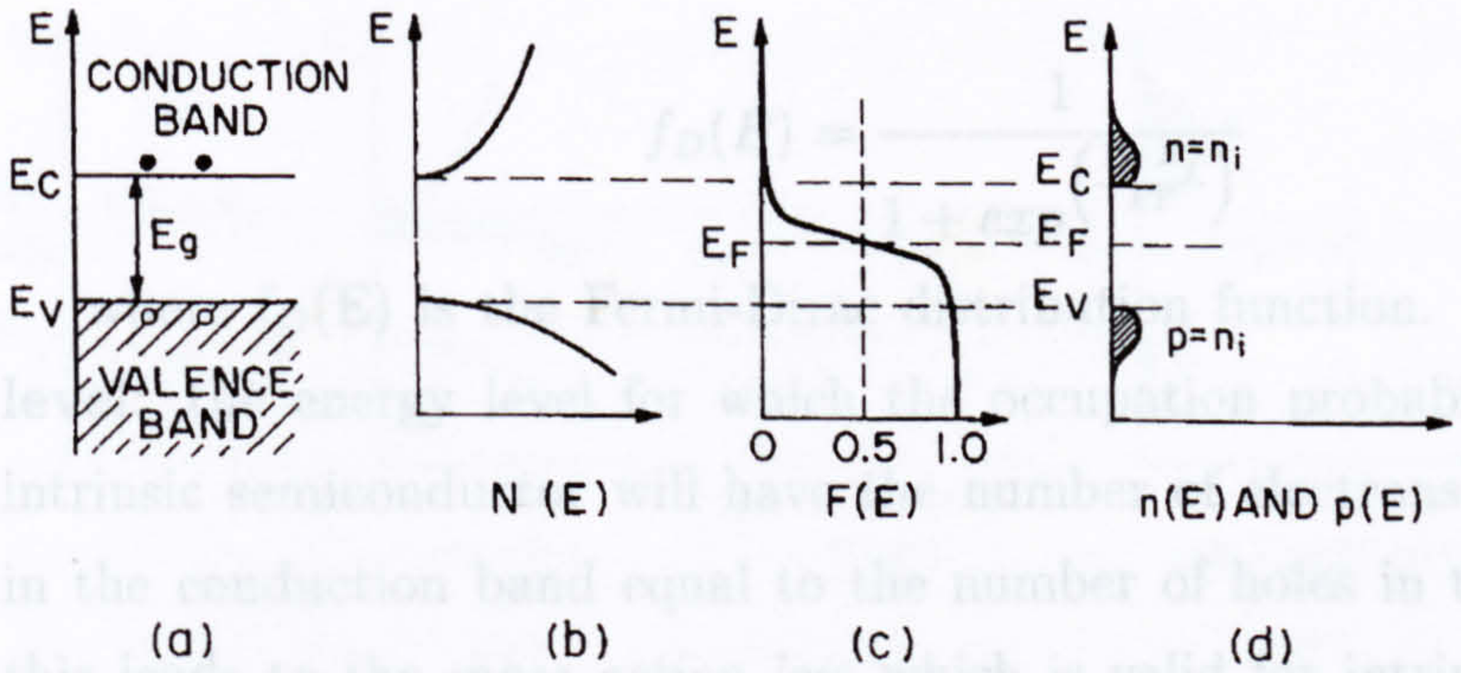

Figure 2.4: Schematics of intrinsic semiconductor parameters. (a) Band diagram. (b) Density of states N(E). (c) Fermi distribution function $f_D(E)$. (d) Carrier concentrations n and p. [19]

2.1.2 Carriers

Thermal excitation elevates electrons from the valence band to the conduction band, and leaves an equal number of holes in the valence band. A pure semiconductor (**intrinsic semiconductor**) contains few impurities compared to the electrons and holes that are generated thermally. The electron density n(E) in energy range dE may be evaluated by the product of the density of states (N(E)) and the state occupation probability ($f_d(E)$). Therefore the electron density in the conduction band (n) is:

$$n = \int_0^{E_{top}} n(E)dE = \int_0^{E_{top}} N(E)F(E)dE \tag{2.3}$$

where E_{top} = energy at the top of the conduction band, and the energy at the bottom of the conduction band is zero. A similar expression for the hole density p may be derived by integrating equation 2.3 across the valence band.

The probability of an electron being found in a state with energy E is given by:

$$f_D(E) = \frac{1}{1 + exp\left(\frac{E - E_f}{kT}\right)} \tag{2.4}$$

where $f_D(E)$ is the Fermi-Dirac distribution function. E_f is the **Fermi level**: the energy level for which the occupation probability is 50%. An intrinsic semiconductor will have the number of electrons per unit volume in the conduction band equal to the number of holes in the valence band, this leads to the *mass action law* which is valid for intrinsic and extrinsic semiconductors:

$$n = p = n_i \ , \ np = n_i^2 \tag{2.5}$$

where n_i is the **intrinsic carrier density**. An extrinsic semiconductor increases the concentration of one type of carrier, which tends to reduce the number of the other type through recombination. Thus, equation 2.5 remains constant for a given temperature. All the above quantities are summarised in figure 2.4 [19].

2.1.3 Doping

For an intrinsic semiconductor, the Fermi level is found in the middle of the bandgap, however the introduction of dopants can move the Fermi level towards the conduction band or the valence band. These impurity atoms introduce new energy levels to the semiconductor, which may lie within the band gap, and will change the relative carrier concentrations of holes and electrons. The semiconductor is said to be *extrinsic* . The process of doping involves replacing some of the atoms in the semiconductor lattice with dopant atoms with a different number of valence electrons. Depending on the semiconductor, the dopant atoms can be **donors** or **acceptors**. A donor is an atom which has one more covalent electron than the intrinsic semiconductor, hence this electron is available for conduction at room temperature. Donor atoms provide a high density of electrons in the conduction band, hence the electrons are **majority carriers** and the semiconductor is said to

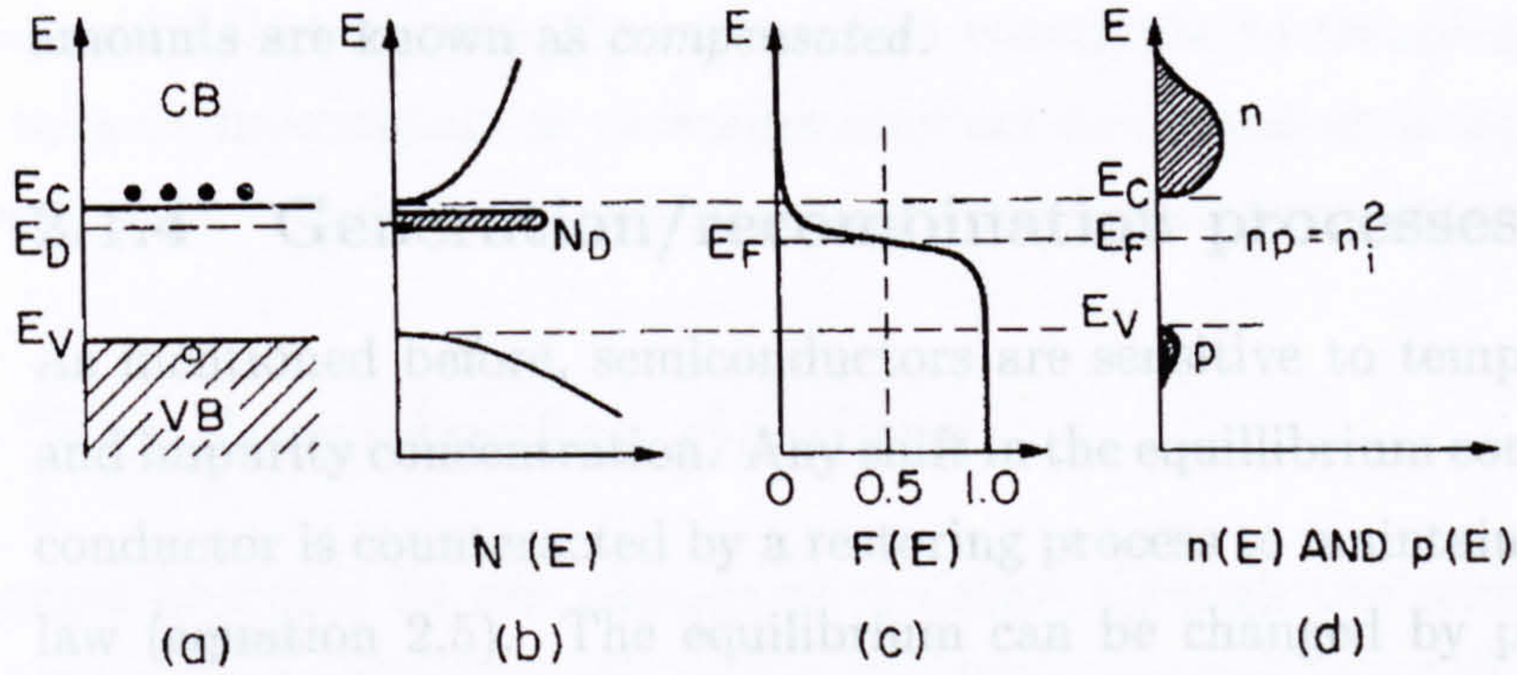

Figure 2.5: Schematics of extrinsic (n-type) semiconductor parameters. (a) Band diagram. (b) Density of states N(E). (N_D is the donor concentration) (c) Fermi distribution function f_D. (d) Carrier concentrations n and p. Note $np=n_i^2$ [19].

be **n-type**. The schematics for n-type semiconductor parameters are shown in figure 2.5 [19]. Conversely, an acceptor atom has one less covalent electron than the semiconductor atoms, and a hole vacancy is formed which migrates through the material like a positive carrier in a sea of fixed electrons. Holes are said to be the majority carriers in this case and the semiconductor is said to be **p-type**.

In the calculation of the impurity energy levels, we consider the ionisation energy for the donor atom. At room temperature, there is enough thermal energy to ionise completely all the shallow donors, and so the electron density n is equal to the donor concentration N_D. Similarly for holes, $p = N_A$, where N_A is the acceptor concentration. It is clear that the higher the donor concentration, the smaller the energy difference between the conduction band edge and the Fermi level. The Fermi level adjusts to preserve charge neutrality between electrons and holes, and ionised donors and acceptors. If both donor and acceptor impurities are present simultaneously, the impurity that is present in greater concentration will determine the type of conductivity. Materials in which the donor and acceptor impurities are present in equal

amounts are known as *compensated*.

2.1.4 Generation/recombination processes

As mentioned before, semiconductors are sensitive to temperature, current and impurity concentration. Any shift in the equillibrium condition of a semiconductor is counteracted by a restoring process to maintain the mass-action law (equation 2.5). The equilibrium can be changed by particles incident on the material, where *charge generation* takes place at a rate G. To restore the disturbance, *carrier recombination*, essentially the annihilation of electron-hole pairs, takes place at a rate R. Similarly, when a semiconductor is connected to an external circuit (e.g. pn junction - section 2.1), carrier extraction is balanced by charge regeneration, and charge injection is balanced by recombination processes.

Recombination and traps

Theoretically, the average lifetime of carriers before recombination in a pure semiconductor should be of the order of seconds [20]. In reality this is not the case due to impurities present in the semiconductor. Impurities such as gold, zinc or other metallic atoms occupying substitutional positions in the crystal lattice will introduce new energy levels near the centre of the bandgap. These are called *deep impurities* , as opposed to the shallow impurities of acceptors and donors which introduce energy levels near the edges of the bandgap. Deep impurities may act as *traps* for carriers which become captured by the centre and immobilised for a period of time. If this period of time is long enough, the carrier cannot contribute to the measured signal.

A deep impurity may capture majority *and* minority carriers and cause them to annihilate. The impurity is said to be acting as a *recombination centre*, and is the predominant form of electron-hole recombination. If the collection time of carriers is less than the average lifetime, almost all the carriers will be able to contribute to the signal before recombination, making this a desirable parameter for a good radiation detector.

Structural defects within the crystal also contribute to trapping. Point defects such as interstitials or vacancies may act as donors or acceptors respectively, while line defects and dislocations may act as trapping centres.

2.2 Semiconductor devices

The charges liberated by the passage of radiation through the semiconductor may be used to "detect" the radiation. This requires some method of measuring the deposited charge in the material. The quick solution would seem to suggest two metal contacts on opposite faces, but the leakage current at room temperature means this method is only suitable for insulators and very high resistivity semiconductors. A region of internal electric field with no charge carriers would give a low enough leakage current to allow electron-hole pairs to be sensed. This is achieved through the creation of a *reversed-biased junction*, and may be realised by two detector structures: a p-i-n diode (p-n junction with intrinsic layer between); and a Schottky diode (metal on semiconductor contact). The ideal p-n juction will be described, and using this model the properties of a Schottky contact formulated.

2.2.1 The p-n junction

A p-n junction may be fabricated by diffusion of p and n regions into a high resistivity substrate. Because of the differing carrier concentrations on either side of the junction, these carriers diffuse across the interface. The n-type region, which has electrons as majority carriers, will see these carriers diffuse across the junction to the p-type side, leaving behind an area of donor ions which leave a region of positive fixed space charge. The electrons which diffused through to the p-type region will annihilate with the holes (p-type majority carriers). The opposite is true for the holes in the p-type material, resulting in a net negative space charge region in the p-type material. These regions cause the energy levels and the Fermi level in the p-side to be raised, with a corresponding lowering of the n-side levels. The electric field estab-

lished by these space charge regions prevents the flow of majority carriers, but allows the flow of minority carriers in the opposite direction. Eventually, the two current flows are equal and the net current flow across the junction becomes zero. The potential difference which causes the equalisation of the Fermi levels and the restriction of current flow is called the **built-in potential**.

If N_A and N_D are the acceptor and donor impurity concentrations, the depletion layer thicknesses for a one sided junction are [19]:

$$W = \sqrt{\frac{2\varepsilon_s}{qN_B}\left(V_{bi} - \frac{2kT}{q}\right)} \tag{2.6}$$

where N_B is N_A or N_D, depending on whether $N_A \gg N_D$ or vice versa, and ε_s is the permittivity of the material. If an external voltage (V) is applied to the junction, the built-in potential will be increased if the junction is **reversed biased** (i.e. the n-side is positive and the p-side negative - reinforcing the oppositely charged space-charge regions which have formed). Hence the depletion layer thickness increases with increasing reverse bias.

2.2.2 The p-i-n diode

The silicon detectors studied in this thesis are *p-i-n* diodes of 300μm thickness. A p-i-n diode is a high resistivity intrinsic region provided with p and n non-injecting contacts at either surface. This reduces the leakage current sufficiently to allow X-ray spectroscopy up to about 30keV. The behaviour is similar to that of an ideal pn junction.

2.2.3 Schottky contact

When a metal makes contact with a semiconductor, a potential barrier (Schottky barrier) is formed at the interface. The metal and semiconductor have different *work functions* $q\phi_m$ and $q\phi_s$ which are defined as the difference in energy between the Fermi level and the **vacuum level** (state outside the surface of the metal). The semiconductor has an electron affinity

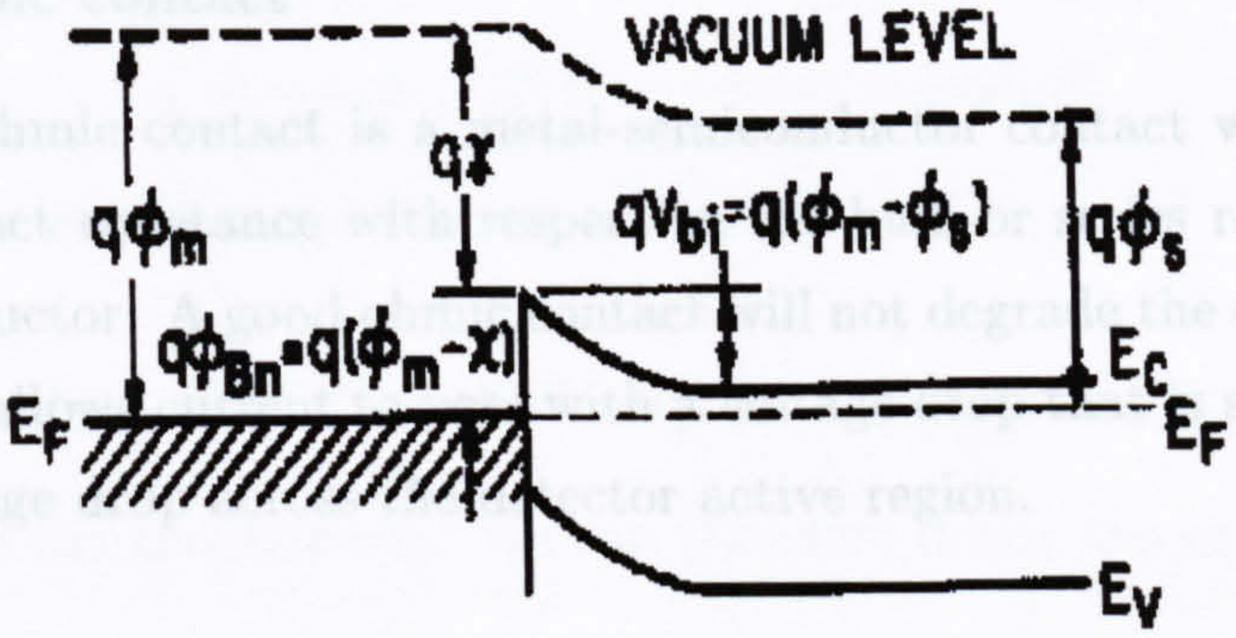

Figure 2.6: Energy band diagram of Schottky contact in thermal equilibrium. q (= e = 1.6×10^{-19} C) gives all parameters units of electron-volts [19]

$q\chi$, which is the difference between the vacuum level and the conduction band edge. When these two materials are put into contact, the Fermi levels must be equal at thermal equilibrium, and the vacuum level must be continuous. These requirements force a unique energy band diagram for an ideal metal/semiconductor contact (Figure 2.6). Here, the barrier height is the difference between the metal work function $q\phi_m$ and the electron affinity $q\chi$ of the semiconductor. This barrier is similar to that of an abrupt one-sided pn junction, and if an external reverse bias V is applied, the depletion width W is [19]:

$$W = \sqrt{\frac{2\epsilon_s(V_{bi} - V)}{qN_d}} \tag{2.7}$$

The ease of fabrication of the Schottky contact, particularly in GaAs, makes it an ideal candidate for radiation detection. The SI-GaAs detectors studied in this thesis are Schottky diode devices with an *ohmic* contact on the back side. At typical Schottky barrier is formed by a multilayer Pt-Ti-Au contact.

Ohmic contact

An ohmic contact is a metal-semiconductor contact which has a negligible contact resistance with respect to the bulk or series resistance of the semiconductor. A good ohmic contact will not degrade the detector performance, and allows current to pass with a voltage drop that is small compared to the voltage drop across the detector active region.

2.2.4 Motion of charge carriers

Free charges generated by incident radiation in a semiconductor are transported through the material in two ways. *Diffusion* occurs due to carrier concentration gradients, and *drift* takes place when the electric field formed inside the semiconductor (by reverse biasing e.g.) moves the charges to their corresponding electrodes.

Diffusion

Diffusion current flows from regions of high carrier concentration to regions of low carrier concentration, and is proportional to the electron density gradient and diffusivity (D_n):

$$J_n^{diff} = qD_n\frac{dn}{dx}\ ,\ D_n = \left(\frac{kT}{q}\right)\mu_n \tag{2.8}$$

where μ_n is the electron *mobility* (assuming $n \ll N_C$). It can be seen that the drift current is directly proportional to the mobility. Equation 2.8 also holds for holes.

Drift

The application of an electric field E causes each electron to feel a force $-qE$ in the opposite direction. Using τ_c as the mean free time between collisions and electron momentum $-qE\tau_c$, we may define the *drift velocity* v_n and then the drift current density J_n^{drift} as:

$$v_n = -\mu_n E \ , \ J_n^{drift} = -qnv_n = qn\mu_n E \tag{2.9}$$

Adding the electron and hole contributions:

$$J_{drift} = J_n^{drift} + J_n^{drift} = (qn\mu_n + qp\mu_p)E = \sigma E \tag{2.10}$$

where σ is the *conductivity*. We can therefore define the resisitivity ρ:

$$\rho = \frac{1}{\sigma} = \frac{1}{qn\mu_n + qp\mu_p} \tag{2.11}$$

2.2.5 Charge collection in semiconductors

Under an electric field, the electrons and holes created by the interaction of photons with the material are separated and drift to their corresponding electrode. This drift of mobile carriers causes charge to be induced on the electrodes which may be measured by the readout electronics and is equivalent to the charge generated in the semiconductor. Ramo's Theorem [21][22] relates the charge dQ induced by the motion of q charge carriers through a distance dx. For a detector of thickness W:

$$dQ = q \times \frac{dx}{W} \tag{2.12}$$

The charge collection efficiency, (η) is defined as the ratio of observed collected charge to the expected charge. Full charge collection is achieved when the carriers reach the electrodes, however charge will be lost if the carriers become trapped by deep levels in the band gap of the semiconductor, or if the depletion region does not extend across the whole detector thickness. Trapping in SI-GaAs is due mostly to the EL2 defect [23].

2.2.6 Interaction of X-rays in semiconductors

The interactions of X-rays in semiconducting materials in the energy region of interest (10keV to 60keV) is dominated by the *photoelectric effect*. The

X-ray interacts with one of the atoms in the lattice and a photoelectron is liberated. If the energy of the incident photon is E_γ, and E_b is the binding energy of the electron to its atom, the energy of this photoelectron is given by:

$$E_p = E_\gamma - E_b \tag{2.13}$$

However, in the ensuing atomic rearrangement, fluorescence photons may be produced which are emitted isotropically, predominantly with an energy of the K series of the semiconductor material. The liberated photoelectron undergoes multiple scattering through the material where it may interact by one of two processes.

- **Electron-phonon scattering**: The photoelectron scatters off a lattice site which is oscillating around its zero energy point.

- **Excitation**: The photoelectron collides with a valence band electron and excites it over the bandgap.

The latter effect is basically electron-hole pair-production, as the creation of the electron in the conduction band is matched by the corresponding creation of a hole in the valence band. Experimentally it has been observed that the energy required to form an electron-hole pair is greater than the bandgap. This is due to the probabilities of the two processes occurring being dependent on the cross-section energy dependence and the density of phonon mode states. The fraction of energy converted into electron-hole pair creation is a property of the detector material. For a given deposit of radiation energy, the signal generated will fluctuate around a mean number of charge carriers N given by:

$$N = \frac{E}{\varepsilon} \tag{2.14}$$

where E is the energy absorbed in the detector, and ε is the mean energy for e-h pair creation or ionisation energy, which is observed to be largely

Semiconductor	Silicon (Si)	Gallium arsenide (GaAs)
atomic number (Z)	14	31/33
structure	diamond	zincblende
type	indirect	direct
bandgap at 300K (eV)	1.12	1.42
mobilities at 300K (cm^2/Vs)		
electrons	1500	8500
holes	450	400
Fano Factor (F)	0.12	0.18
E (e-h pair) (eV)	3.61	4.27

Table 2.1: Properties of silicon and gallium arsenide.

independent of the energy and type of incident radiation. The *observed* mean energy has a variance (σ) that is less than the variance predicted from Poisson statistics, due to the events along the particle track not being independent. The Fano factor [24] relates the observed and predicted variances, where:

$$F \equiv \frac{\sigma}{N} \tag{2.15}$$

The Fano factor influences the energy resolution of the detector, i.e. the lower the Fano factor, the better the energy resolution. Although a complete understanding of the factors that give a non-unity Fano factor does not yet exist, it has been postulated that the value may depend on the nature of the incident particle. It is seen that the Fano factor increases sharply at low energy levels, placing a limit on the energy resolution achieveable with the PCD.

2.3 Silicon and Gallium Arsenide

The special properties and growth of the materials studied in this thesis is presented in the following section. Two materials have been investigated:

SI-LEC GaAs; and silicon. Table 2.1 shows the relevant properties of each material for comparison [19].

2.3.1 Silicon

Silicon has atomic number 14 and crystallises in the diamond lattice. It is well suited for imaging low energy X-rays, with a low contribution from escape peaks (fluorescence). The transparency of silicon to high energy X-rays is useful if there is a high gamma background. The material quality in silicon is of a very high standard, and devices made from silicon typically give charge collection efficiencies of 100% for soft X-rays despite the low Z, as photoelectric absorption still dominates below 20keV. The uniformity of the material and resilience to standard processing make it attractive for characterisation of devices.

Crystal growth

The Czochralski technique for silicon crystal growth uses a device called a puller. Polycrystalline silicon is placed in a crucible and heated to above melting point. A seed crystal is suspended over the crucible in a holder and inserted into the melt. The puller then draws the partially melted seed from the melt and progressive freezing at the solid-liquid interface yields a large single crystal. Approximately 90% of silicon grown for the semiconductor industry uses the Czochralski technique.

2.3.2 Gallium arsenide

GaAs has average atomic number 32, and crystallises in the zincblende lattice. It is a direct bandgap semiconductor with a bandgap of 1.42eV at 300K, and because of this, the intrinsic carrier concentration is very small. GaAs may be grown in a number of ways [25]:

- **LEC**(Liquid-Encapsulated Czochralski): High resistivity, but high level of C and dislocations.

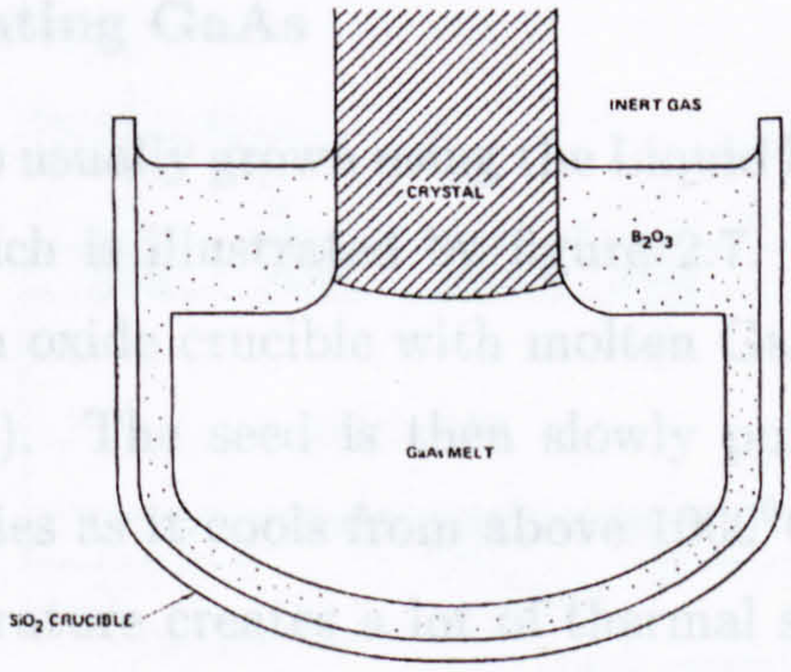

Figure 2.7: Cross section of the crucible for the growth of LEC GaAs.

- **VGF**(Vertical Gradient Freeze): Ga and As are liquified, enclosed with a GaAs seed and slowly cooled. Similar problems to LEC material.

- **LPE**(Liquid-Phase Epitaxy): single crystal layers grown from supersaturated solution. Difficult to attain low doping levels.

- **VPE**(Vapour-Phase Epitaxy): uses chemical reaction with HCl gas to form GaAs. Lower impurity levels.

The GaAs detectors studied in this thesis were all fabricated from semi-insulating (SI) LEC GaAs substrates.

The EL2 defect

The EL2 defect is widely believed to originate from a substitutional arsenic antisite, where an arsenic atom moves into a gallium vacancy in the lattice. It is a midgap donor in gallium arsenide, with an energy of about -0.75 eV with respect to the conduction band edge (it also exists in an ionised state ($EL2^+$). Due to compensation of shallow traps by this deep donor, gallium arsenide is often made *semi-insulating* (SI).

Semi-insulating GaAs

Bulk GaAs is usually grown using the Liquid Encapsulated Czochralski (LEC) method, which is illustrated by figure 2.7. A single crystal seed is dipped into a silicon oxide crucible with molten GaAs encapsulated by liquid boric oxide (B_2O_3). The seed is then slowly pulled from the crucible, and the GaAs solidifies as it cools from above 1000^0C. Unfortunately, the cooling to room temperature creates a lot of thermal stress, resulting in many defects which affect the conductivity of the material. LEC grown GaAs is also high in impurities, which are usually carbon or silicon.

Semi-insulating GaAs is compensated due to the effect of the deep defects, particularly the EL2. This material has a higher resistivity than uncompensated material, which means less bias voltage required to deplete fully any diode devices made from SI-GaAs. LEC GaAs is made semi-insulating through meeting the following criteria:

$$N_a > N_d$$
$$N_{DD} > N_a - N_d \tag{2.16}$$

where N_{DD} is the concentration of deep donors.

At room temperature the shallow levels are fully ionised, so the shallow acceptors will gain electrons from the shallow donors. Any uncompensated shallow acceptors will be compensated by the EL2 donor to satisfy equation 2.16. To produce enough EL2 for this compensation mechanism, the GaAs is grown arsenic rich.

2.3.3 Epitaxial GaAs

The shortcomings of LEC grown GaAs are being overcome by using epitaxially grown layers [26], specifically using Low Pressure Vapour-Phase Epitaxy (LP-VPE). Vapour phase epitaxy involves passing HCl gas over elemental gallium and letting the resulting GaCl react with arsine (AsH_3) to form

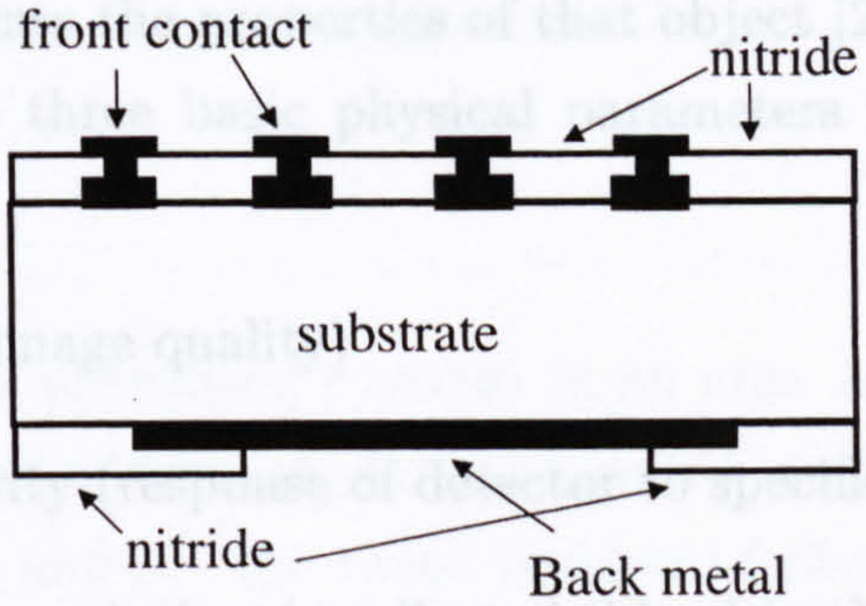

Figure 2.8: Side view of an SI-LEC GaAs substrate Schottky diode detector fabricated at the University of Glasgow.

epitaxial films. The use of low pressure epitaxy increases the growth rate to about 100μm/h compared with the 0.5μm/h rate achieved with Atmospheric Pressure Vapour Phase Epitaxy.

2.4 Schottky diode detector

Figure 2.8 shows a cross section of a Schottky diode detector with an SI-LEC GaAs substrate. These detectors (as fabricated at the University of Glasgow [27]) have a silicon nitride (Si_3N_4) passivation layer to stop surface currents. The back metal is 40nm Pd and 100nm Ge for the ohmic contact. The metal for the front Schottky contact is 33nm Ti, 30nm Pd and 150nm Au.

2.5 Sensor analysis

The performance of any imaging system may be analysed using a "black box" treatment, where nothing is known of the internal workings of the system. This basic system has two terminals; the input terminal which corresponds to the spatially varying intensity of X-rays characterising the transmission

properties of the object, and the output terminal which presents the image which represents the properties of that object [28].

There are three basic physical parameters fundamental to an imaging sensor [29]:

- Noise (image quality)
- Sensitivity (response of detector to specific X-ray energy spectrum)
- Spatial resolution (smallest visible object)

All these parameters contribute to the overall large-scale transfer function [30], which describes the relationship between the system input and the output. Historically, the investigation of signal detection has been tackled in two stages: the radiation detection and the processing and display of the data. This dichotomy is not so obvious when applied to photographic emulsions, but is clearer in the case of charge integrating devices such as CCDs, where the output from the sensor is a voltage dependent on the deposited charge in each pixel. This in turn is fed into a computer for digitisation into a useful image. The digital output of photon counting sensors removes the digitisation process from the system, thus the three parameters listed above will provide a complete description of the detector performance.

2.5.1 Sensitivity

The ability of a system to respond to a known stimulus may be measured using a number of related parameters.

Dose response

A good X-ray imaging system should have a linear response with increasing dose. Photon counting systems with active pixel logic have a linear and extendable response, which offers advantages over charge integrating devices in terms of lack of saturation at high dose, and "fog" (dark current) at low dose. A dose response curve therefore provides information on the dynamic

range of the sensor, however a more quantitative approach is required to compare the sensitivities of imaging systems.

Contrast

Considering an object presenting contrast in an area A of the detector, we define n to be the mean number of photons counted in the background region (i.e. outside area A) and n' the mean number of photons counted in the target region. The *contrast* (or modulation ratio), C, an object presents to an imaging system may be calculated from:

$$C = \frac{n - n'}{n} \tag{2.17}$$

The contrast of an object should remain the same for increasing dose, and depends on the absorption properties of the object and scattering effects. A bar/space pattern may be used to define the contrast at increasing spatial frequency. By analogy with equation 2.17 given the maximum and minimum intensities (I_{max} and I_{min}) in the bar/space region respectively, the contrast may be calculated from:

$$C = \frac{I_{max} - I_{min}}{I_{max} + I_{min}} \tag{2.18}$$

Signal-to-Noise ratio

Image quality and the ability to discriminate signals from the background is related to the signal strength and noise level in the image. The *Signal-to-Noise Ratio* (SNR) is defined as the ratio of the signal amplitude to the standard deviation in the mean signal (noise). This quantity can be calculated in many ways, but considering the sensitivity of the detector it is convenient to define the SNR in terms of the number of photons counted. In the case of Poisson limited statistics, the Signal-to-Noise ratio may be defined as:

$$SNR = \frac{n - n'}{\sqrt{n + n'}} \tag{2.19}$$

where $\sqrt{n}$ is the quantum noise (see noise section). In the general case where other noise sources such as noise from the electronics or fixed pattern noise may be a factor:

$$SNR = \frac{n - n'}{\sqrt{\sigma_n^2 + \sigma_{n'}^2}} \tag{2.20}$$

The SNR of a flood image is simply the mean counts per pixel across the sensor divided by the standard deviation σ, where this value is dependent on incident flux. The minimum value of SNR that gives a detectable signal is generally taken to be about 5 [5].

The signal-to-noise ratio is related to the contrast C by combining equations 2.17 & 2.20 to give:

$$SNR = \frac{nC}{\sqrt{\sigma_n^2 + \sigma_{n'}^2}} \tag{2.21}$$

2.5.2 Spatial resolution

The degradation of images due to the sensor's intrinsic spatial resolution properties may be characterised by measuring the response of the detector to simple, known objects. In principle, this knowledge may be extended to predict the response to more complex objects. Techniques for measuring these properties involve the imaging of some highly localized feature and the analysis of the corresponding blurred image from the sensor. These techniques require the imaging system to be *linear* and *shift-invariant* [31], enabling several unique characteristics of the imaging system to be defined.

Point Spread Function

The Point Spread Function (PSF) is the response of the imaging system to an ideal point stimulus (i.e. a point Dirac delta function), and describes

the transfer of a two-dimensional object through the system. It may be measured by imaging an infinitely small aperture (point source) radiating with unit radiant energy. This is made difficult experimentally due to the low radiant energy through such a small aperture. It is clear that a different form of sensor stimulus is required.

Line Spread Function

The Line Spread Function (LSF) gives the response of the detector to an infinitely narrow slit (i.e. a linear Dirac function), and is an accurate experimental tool for the determination of the PSF. Unlike the PSF, however, the LSF does not describe the transfer of 2-D inputs, but rather simplifies the transfer problem in the case of 1-D inputs. Nevertheless, it is a vital measurable property for the determination of the system Modulation Transfer Function.

For a pixel detector, the slit size used for the determination of the LSF should be less than 15 μm, or one fifth of the pixel pitch, whichever is the smaller. The slit is placed at an angle to the detector direction along which we wish to measure the spatial resolution. This is done to ensure that the slit is not sitting between two adjacent pixel rows. The pixels with maximum response are selected, corresponding to the pixels directly under the slit, and linear regression is used to find the equation of the line which best describes the slit in the image. The distance to this line (x) for all the pixels responding is calculated and the intensity (normalised to 1) against the distance to the slit is plotted.

The LSF is described by [32]:

$$LSF(x) = a_2 \exp^{-\left[\frac{x-a_1}{a_3\sqrt{2}}\right]^2} + a_4 \exp^{-\frac{|x-a_1|}{a_5}} \tag{2.22}$$

A non-linear fit to the LSF data may be used to deduce the values of a_1-a_5. Alternatively a digital transformation (Fast Fourier Transform) of the LSF data yields the MTF without some of the systematic uncertainties inherent in the fitting coefficients.

Contrast Transfer Function

The response of a detector to a square wave input of increasing spatial density allows the Contrast Transfer Function (CTF) to be obtained. The contrast measurement of the signal at each spatial frequency of a bar/space test object yields a function which describes the frequency components of an object that are visible to the sensor. This forms the basis of the Modulation Transfer Function, which may be derived from all the above functions. An optically transparent test mask with lead bars at increasing spatial density is imaged, and the contrast between the lead and background is calculated using equation 2.18. Performing this calculation across a large number of spatial frequencies yields the CTF(f), which may be used to calculate the MTF (see section 2.5).

2.5.3 Noise

All imaging system processes are susceptible to noise. This enforces a statistically based analysis of the system performance. In an X-ray imaging system, there are three sources of noise:

- Fixed pattern noise
- Electronic noise (ENC)
- Photonic noise

Fixed pattern noise

Fixed pattern noise is caused by the inhomogeneity of the sensitivity of the detecting medium across the sensor surface and is directly proportional to the signal. This noise source may be compensated for by calibrating each individual pixel [33]. In this case, multiple flood images are taken with the system, and a pixel-by-pixel average is performed to obtain a mean image. A flood image is simply a uniform, equal exposure across the sensor area. The pixels in the mean image are divided by the overall mean of all the pixels in

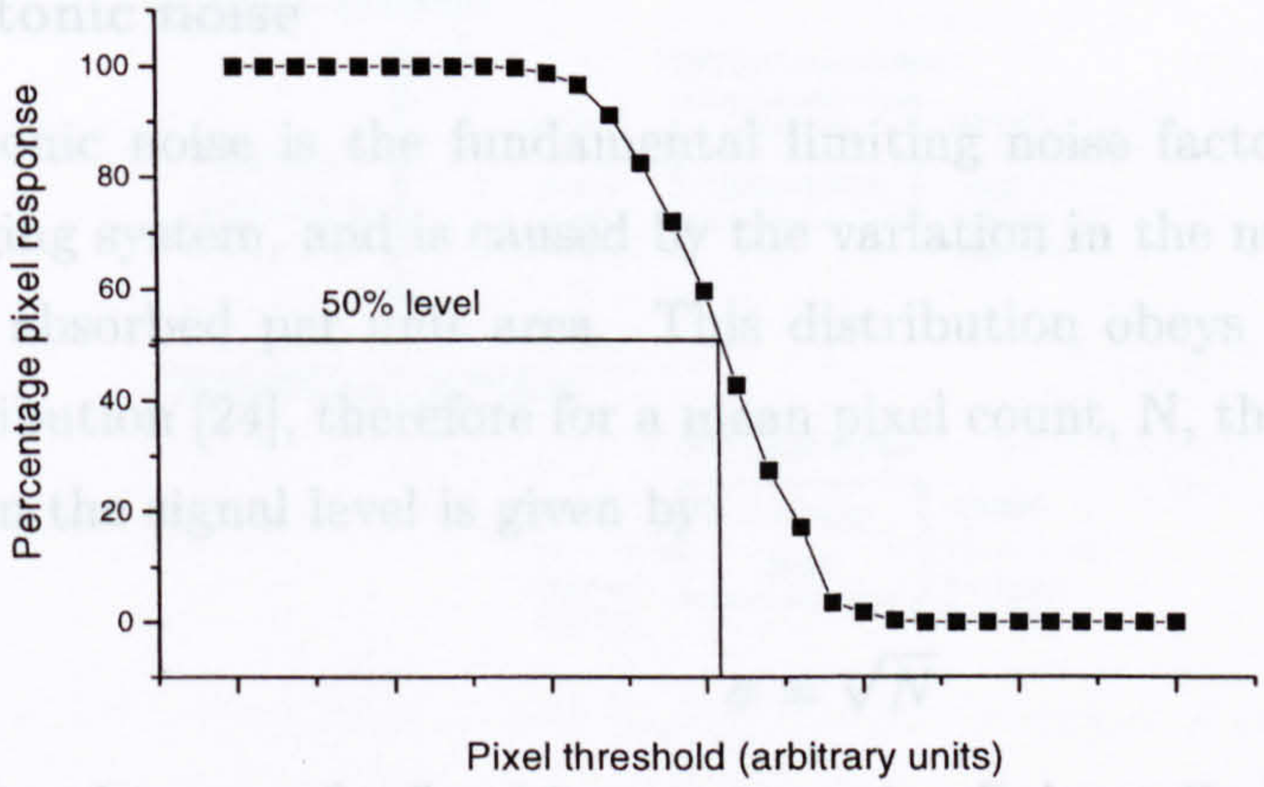

Figure 2.9: A typical "S-curve" response for a single detector pixel.

the flood image. The result is a matrix which has a multiplication factor for each pixel which may be applied to any image taken with the system in order to smooth the response. This technique only works if the inhomogeneities display no time dependence.

Electronic noise (ENC)

Electronic noise arises from sources such as Johnson noise (from series resistances and poor electrical contact with the detector), shot noise (leakage current fluctuations) and the capacitance at the input of the preamplifier. In a counting system, the electronic noise may be calculated from analysis of the S-curve response for a single pixel at increasing test pulse height.

The "S-curve" results from the loss of counts in a pixel as the threshold goes up. At low threshold, the counts are at a maximum, then as the threshold increases, the number of counts rapidly drops to zero at high threshold. The 50% response level is taken as the threshold of that pixel. The S-curve response is demonstrated in figure 2.9.

Photonic noise

Photonic noise is the fundamental limiting noise factor in an ideal X-ray imaging system, and is caused by the variation in the number of X-ray photons absorbed per unit area. This distribution obeys a Poisson statistical distribution [24], therefore for a mean pixel count, N, the standard deviation (σ) in the signal level is given by:

$$\sigma = \sqrt{N} \tag{2.23}$$

For the case of a flood image, assuming Poisson-limited noise behaviour, the signal-to-noise ratio is:

$$SNR = \frac{N}{\sqrt{N}} = \sqrt{N} \tag{2.24}$$

A SNR which varies as $\sqrt{N}$ with increasing dose indicates that the noise in the sensor is dominated by the photonic noise. The SNR is clearly related to the number of photons detected per unit area, and the image quality improves as the number of X-ray quanta used increases. However, it is necessary to use second order statistics to describe the noise fully not only in terms of intensity, but also in terms of spatial noise correlations. This is the basis of the Noise Power or Wiener spectrum which is presented in the next section.

2.6 Fundamental imaging parameters

The above imaging concepts allow the determination of a set of figures of merit which allow different systems to be compared directly, irrespective of detector type and mode of operation.

2.6.1 Modulation Transfer Function

The Modulation Transfer Function (MTF) shows the response of an imaging system to a sinusoidal input of varying spatial frequency, and is an accurate representation of the fidelity of reproduction of object details at various

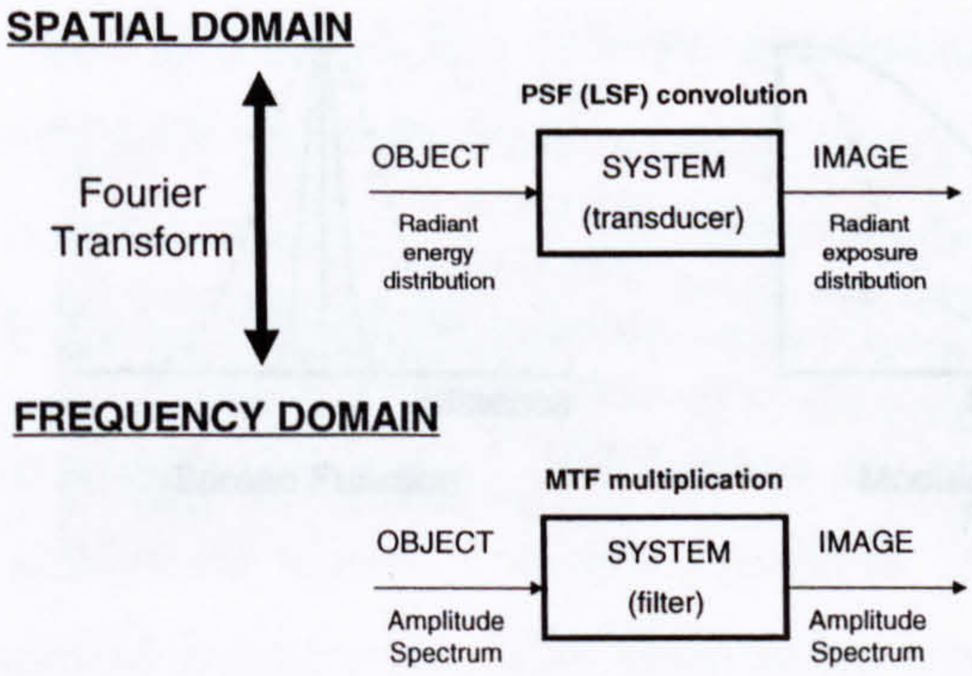

Figure 2.10: The concept of the Modulation Transfer Function.

spatial frequencies. Almost all imaging systems reproduce the lower spatial frequencies much better than the higher spatial frequencies, hence the MTF decreases with increasing spatial frequency. Since the MTF describes the transfer of sinusoidal inputs in the frequency domain, it also describes the transfer of amplitude spectra. Therefore the MTF is a general transfer characteristic of imaging systems in the frequency domain, linking arbitrary inputs with their corresponding outputs.

The MTF of a linear shift-invariant system is defined as the magnitude of the Fourier transform of the PSF of the system (Figure 2.10). The LSF may also be used for the calculation, but it must be noted that an MTF calculated with the LSF is only a profile of the *true* 2-D MTF. Therefore a single measurement of the LSF (or Edge Spread Function (ESF)) is not enough to describe the MTF, and a series of different measurements at different object orientations is required [34].

The MTF may be calculated in two ways:

- Direct measurement with a bar/space pattern using the CTF
- Analysis of the LSF (or edge spread function)

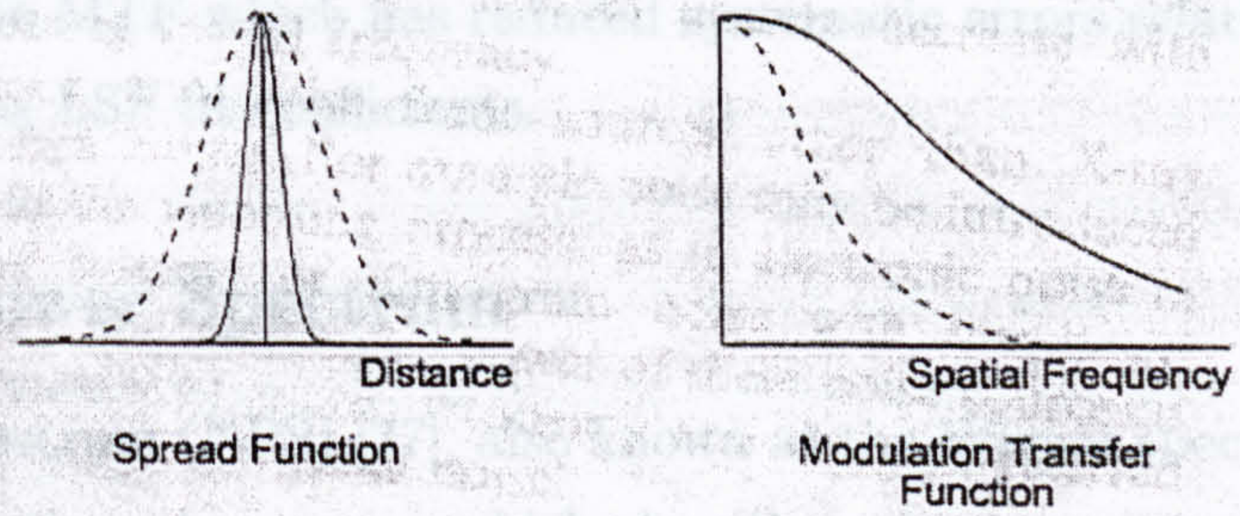

Figure 2.11: Relation of the Spread function to the MTF. A width increase in the LSF (dashes) corresponds to a decrease in the MTF at higher spatial frequencies.

CTF method

Since the CTF describes the contrast response to a set of rectangular pattern inputs, the MTF may be calculated from the CTF using a Fourier Series to obtain the sinsusoidal response. Provided the bar/space pattern represents a high number of spatial frequencies, the MTF may be defined by:

$$MTF(f) = \frac{\pi}{4}\left[CTF(f) - \frac{1}{3}CTF(3f) + \frac{1}{5}CTF(5f) - \frac{1}{7}CTF(7f)...\right] \tag{2.25}$$

where f is the spatial frequency in lp/mm along one direction.

LSF method

The MTF is found from the modulus of the Fourier Transform of the LSF, using the same coefficients as deduced in equation 2.22. Figure 2.11 shows the effect of the widening of the LSF on the calculated MTF. Given the LSF, the MTF may be calculated from [35]:

$$MTF(f) = \frac{\sqrt{2\pi}a_2a_3\exp^{\left[-2\pi^2a_3^2f^2\right]} + \left(\frac{2a_4a_5}{(1+4\pi^2a_5^2f^2)}\right)}{\sqrt{2\pi}a_2a_3 + 2a_4a_5} \tag{2.26}$$

Alternatively, a fast Fourier transform (FFT) may be applied to the data

to give a result for the MTF which has reduced systematic errors relative to those using the a_1 - a_5 LSF fit coefficients.

2.6.2 Noise Power Spectrum

The Noise Power Spectrum (NPS) [37], also known as the Wiener spectrum, is a second-order statistical measure which describes the intensity of the noise at different spatial frequencies. The total noise power is composed of the quantum noise associated with the X-ray source, and system noise such as electronic noise or loss of resolution.

Imaging systems blur fluctuations in the signal arising from noise in the same way that object signals are blurred. Quantum noise fluctuations are also blurred, however the power of the noise usually decreases with increasing spatial frequency. System noise however, is often independent of spatial frequency, and such sources are referred to as sources of "white noise".

The NPS may be calculated by taking the squared modulus of the 2-D Fourier transform of the noise in an evenly exposed flood image. To reduce the noise in the NPS, a large number of spectra need to be averaged. Taking an area of the sensor from (-X,-Y) to (X,Y) (with u,v being the corresponding coordinates in frequency space), and averaging the counts (or grey level) within the area to give an intensity, $\bar{E}$ [36]:

$$NPS(u,v) = \frac{1}{4XY}\left|\int_{-Y}^{Y}\int_{-X}^{X}(\Delta E/\bar{E})exp^{-2\pi i(xu+yv)}dxdy\right|^2 \qquad (2.27)$$

An average may be performed, assuming radial symmetry, to determine a one-dimensional representation of the NPS, the Wiener spectrum, $W_{\frac{\Delta E}{E}}(f)$.

2.6.3 Noise Equivalent Quanta (NEQ)

The signal and noise characteristics of an imaging system may be expressed in a single figure, the Noise Equivalent Quanta (NEQ). The NEQ describes the photon fluence that would give rise to the same SNR if the source of

all noise is attributed to quantum fluctuations in the photon beam. This assumption is made irrespective of the actual source of noise, so the noise level is assumed to be due to the apparent number of X-ray quanta per unit area, which is directly related to the SNR (equation 2.24).

The NEQ has dimensions of quanta (or photons) per unit area and may be calculated from:

$$NEQ(f) = \frac{MTF^2(f)}{W_{\frac{\Delta E}{E}}(f)} \tag{2.28}$$

Low noise levels, hence higher SNR are associated with larger number of NEQ. The NEQ is decribed as the *apparent* number of X-ray quanta used in image formation, and will always be less than the actual number to which the system is exposed since:

- Not all photons are absorbed by system.
- High energy X-ray conversion to lower energies gives a spread in the energy deposited (increased noise).
- The image system adds sources of noise other than photonic.

2.6.4 Detective Quantum Efficiency (DQE)

The Detective Quantum Efficiency (DQE) is defined with the purpose of including spatial resolution, signal-to-noise ratio and sensitivity in the same figure [37]. The DQE is a measure of the efficiency with which the imaging system utilises the X-ray quanta to which it is exposed. It is calculated by comparing the NEQ to the incident photon fluence, Φ, hence we define:

$$DQE(f) = \frac{NEQ(f)}{\Phi} \tag{2.29}$$

The DQE is independent of the dose, but dependent on the X-ray spectrum. The NEQ is always smaller than the exposing photon fluence, hence the DQE is less than unity for all systems. Further reduction of the DQE

arises from loss of resolution by the system and noise introduced by the sensor, both of which are manifest as reduced NEQ.

The DQE can also represent the SNR transfer efficiency of the imaging system, since NEQ is the SNR^2 at the output of the system and the exposing photon density defines the SNR^2 at the input. Therefore,

$$DQE = \frac{SNR_{out}^2}{SNR_{in}^2} \tag{2.30}$$

Since DQE is essentially a measure of the dose efficiency of the imaging system, a system with 20% efficiency requires half the X-ray quanta required for a 10% efficient system to achieve the same image quality (same SNR). Therefore, higher DQE allows reduced patient exposure.

Chapter 3

Photon counting detector (PCD)

The architecture and characterisation of the photon counting detector are described in the following chapter. A description of the read-out chip, detector and experimental set-up is followed by results of the readout chip characterisation. A section on the properties of the complete detector assembly follows, and finally some other measurements related to device degradation and the selection of known good dice during wafer probing are presented.

3.1 Description

The photon counting detector (PCD) is a hybrid semiconductor pixel detector (see chapter 1), comprised of the photon counting readout chip (PCC1) bump-bonded to an equally segmented semiconductor detector. This whole assembly is mounted on a PCB board, and is read out using either a VME based controller, or a dedicated I/O interface board. A description of each of the elements of the whole system follows.

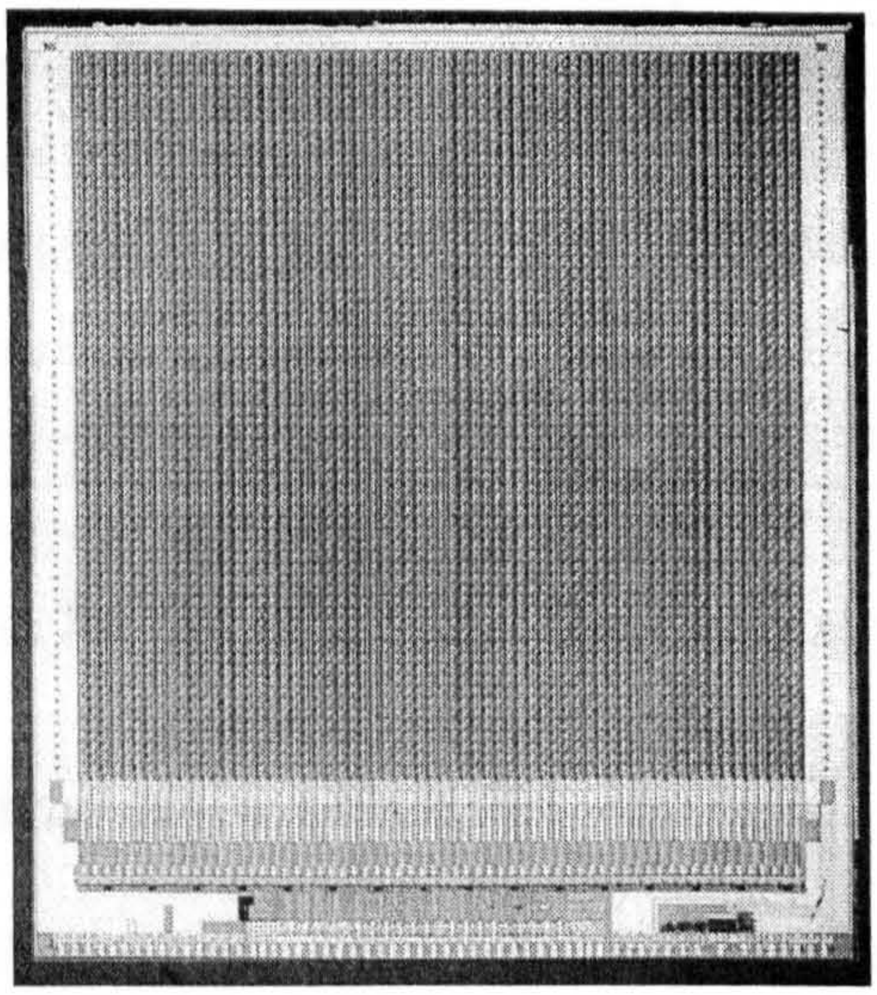

Figure 3.1: Photograph of the photon counting readout chip (PCC). The 4096 pixels each have a size of 170μm x 170μm.

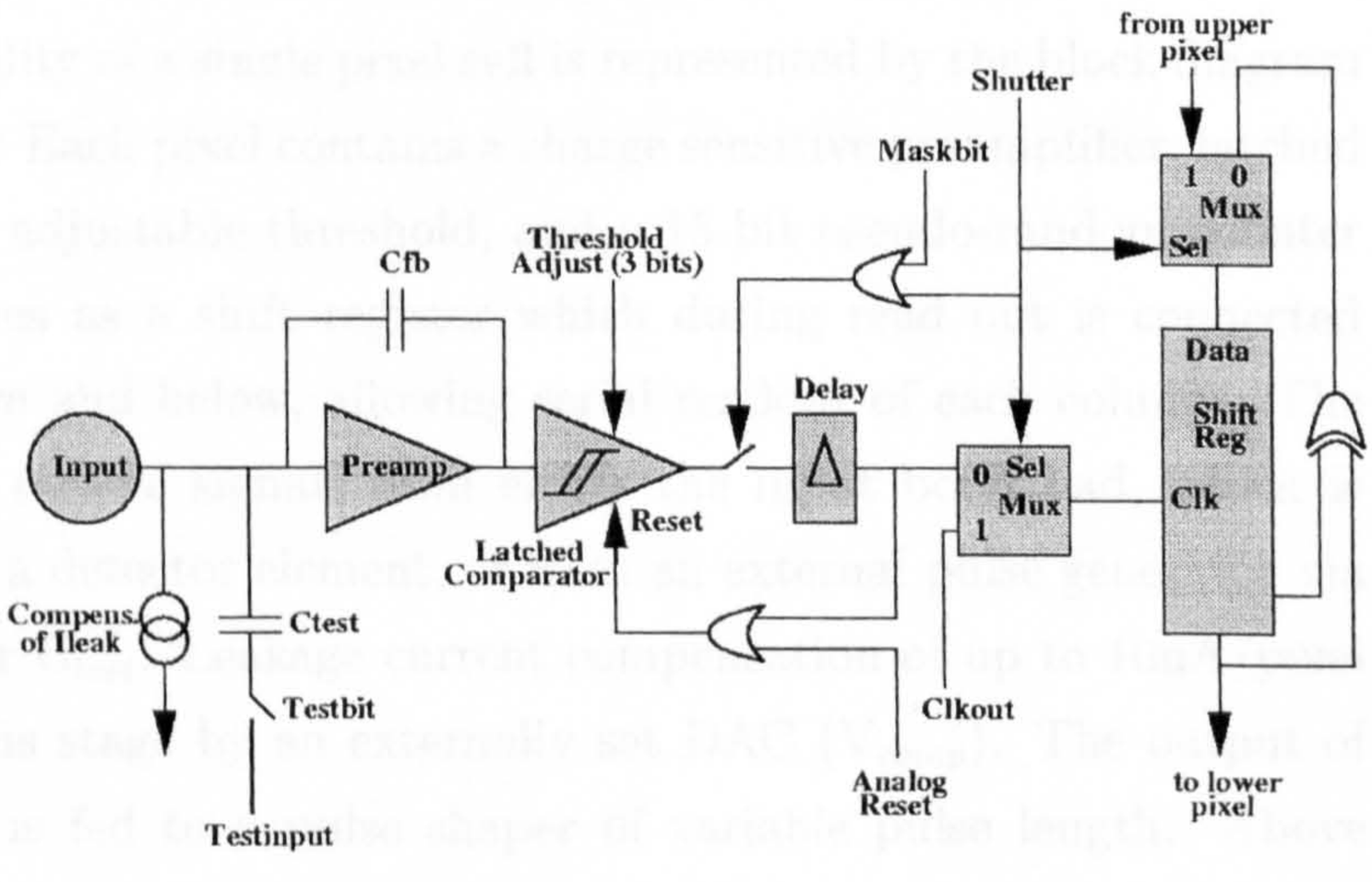

Figure 3.2: Block diagram of a single PCC pixel cell. [39]

DAC voltage	Function	Typical values (V)
V_{bias}	Preamp bias voltage	1.6-1.8
V_{comp}	Leakage current compensation	1.0-3.2
V_{dl}	Width of pulse	0.7-0.8
V_{th}	Minimum threshold	1.2-1.8
V_{tha}	Threshold adjust	0.7-0.8

Table 3.1: Bias voltages for the PCC1, and their typical values

3.1.1 Photon counting chip (PCC1)

The readout chip is designed in the 1 μm SACMOS1 technology of FASELEC (Zurich) [38] which is equivalent to a 0.6 μm standard CMOS process. The chip has a 64×64 matrix of identical square pixels with 170 μm pitch (centre to centre) operating in single photon counting mode, forming a total sensitive area of 1.18 cm^2, which corresponds to over 70% of the total area of the chip [40][42]. Figure 3.1 shows a photograph of the top of the readout chip prior to bump-bonding.

The functionality of a single pixel cell is represented by the block diagram in Figure 3.2 [39]. Each pixel contains a charge sensitive preamplifier, latched comparator with adjustable threshold, and a 15-bit pseudo-random counter [41] which behaves as a shift register which during read out is connected to the pixel above and below, allowing serial readout of each column. The preamplifier can receive signals from either the input bond pad, which is bump-bonded to a detector element, or from an external pulse generator via the test capacitor C_{test}. Leakage current compensation of up to 10nA/pixel is provided at this stage by an externally set DAC (V_{comp}). The output of the preamplifier is fed to a pulse shaper of variable pulse length. Above the global threshold V_{th}, the comparator contains three fully static flip-flops to provide a 3-bit threshold fine-tune, the range of which is determined by another bias voltage (V_{tha}), again externally set by a DAC. Two other flip-flops provide test enabling and masking for each individual pixel. A table of

the bias voltages and their typical values is shown in table 3.1. Note that the value of V_{comp} depends on the type of material used for the detector, where less compensation is needed for silicon because of the lower leakage current.

Complete readout at 10MHz is achieved in 384μs, and the power consumption for the chip is less than 200 mW. The chip is designed to collect holes at the electrode, and so is not well-suited to "single carrier" materials such as CdZnTe. One pixel cell contains about 400 transistors giving a total across the chip of 1.6 million transistors [43].

3.1.2 Experimental setup

The PCD is run from a PC with dedicated software [44] developed by INFN, Napoli as a C executable and a newer LabWindows appication, and the device is controlled either through a VME crate or built-in PCI boards with a special interface. The PCD is powered by 4 externally supplied voltages:

- V_{dd} +3.0V power for digital part of electronics
- V_{dda} +3.0V power for analog part of electronics
- V_{cc} +5V power line for motherboard/MUROS board.
- V_{gnd} +1.5V Reference analog
- V_{ss} System ground (0V)

Except where indicated, measurements have been made with the LABEN VME readout system.

VME setup

Figure 3.3 shows a schematic of the University of Glasgow setup. A PC communicates with the PCD through an MXI-PCI-2 card, connected to an MXIbus controller in slot 0 of a VME crate. Also in the VME crate is the LABEN MRS-1 board, which has all the read/write FPGAs and also

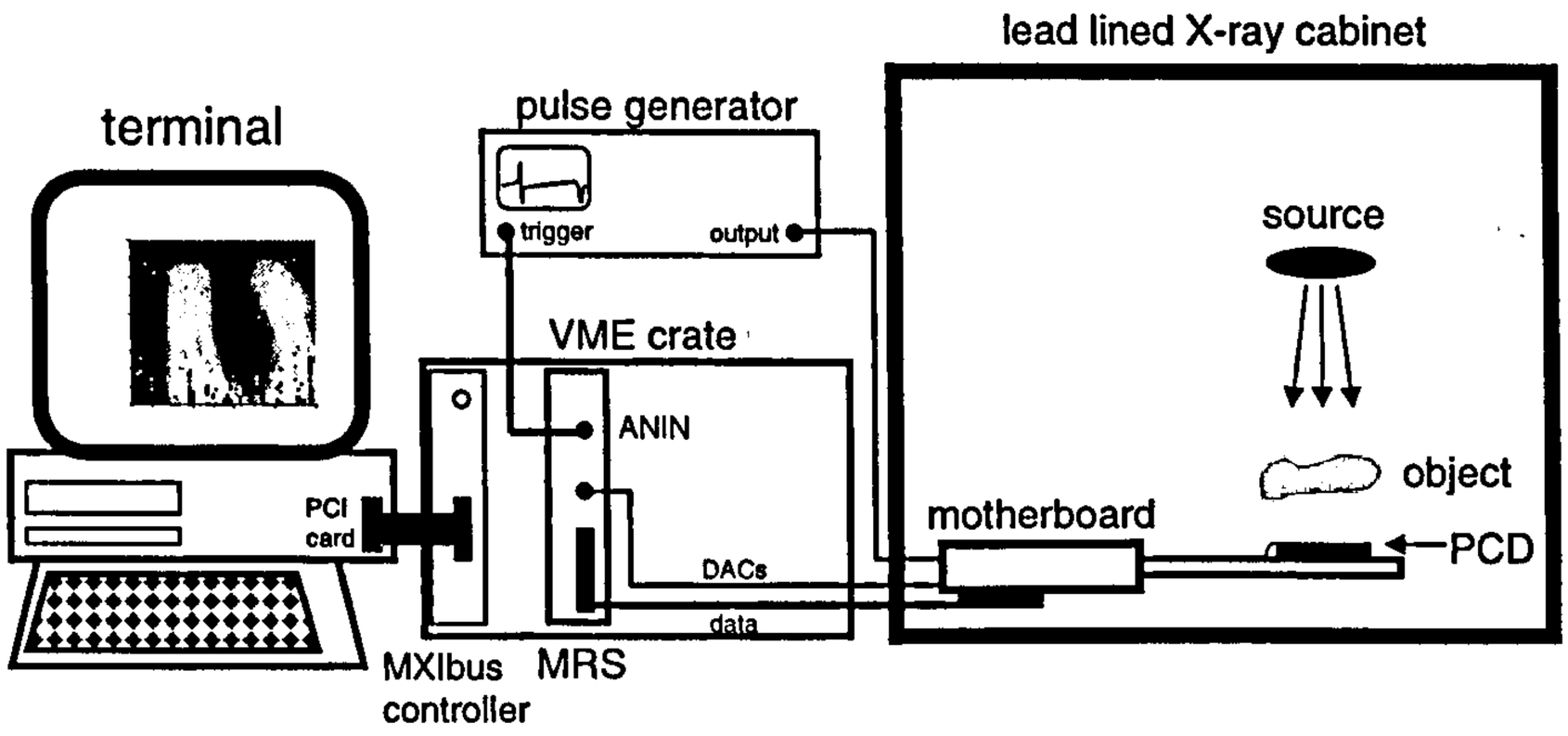

Figure 3.3: Schematic of the VME based LABEN MRS system.

sets the bias voltages [45]. The PCD is connected to this board through a motherboard which acts as a voltage regulator, and also as a measuring point for all the input/output lines. A pulse generator receives the timing signal ANIN, and changes the pulse amplitude while keeping the same timings. This is discussed further in section 3.2.1.

MUROS-1 setup

MUROS1 is a special interface designed to allow the PCD to be run from analog and digital PCI cards installed in the PC which generate the bias voltages, and perform the read/write functions [46]. Figure 3.4 shows the setup with the MUROS board, eliminating the need for the cumbersome (and expensive) VME crate. An internal pulse generator is provided on the MUROS board, allowing quick threshold calibrations to be measured without the need for an external pulse generator.

X-ray tube

Most of the detector measurements were made with a standard dental X-ray tube. The system used was the Planmeca Prostyle Intra X-ray set operating

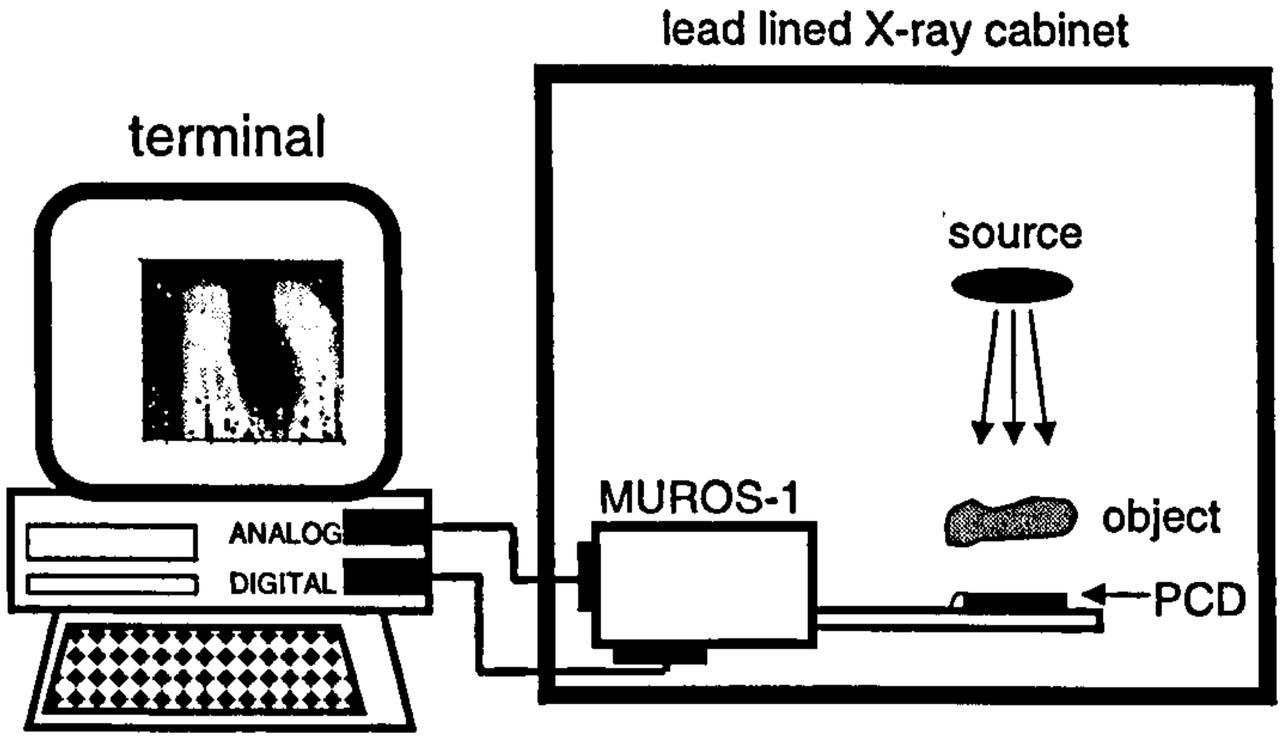

Figure 3.4: Schematic of the MUROS-1 readout system

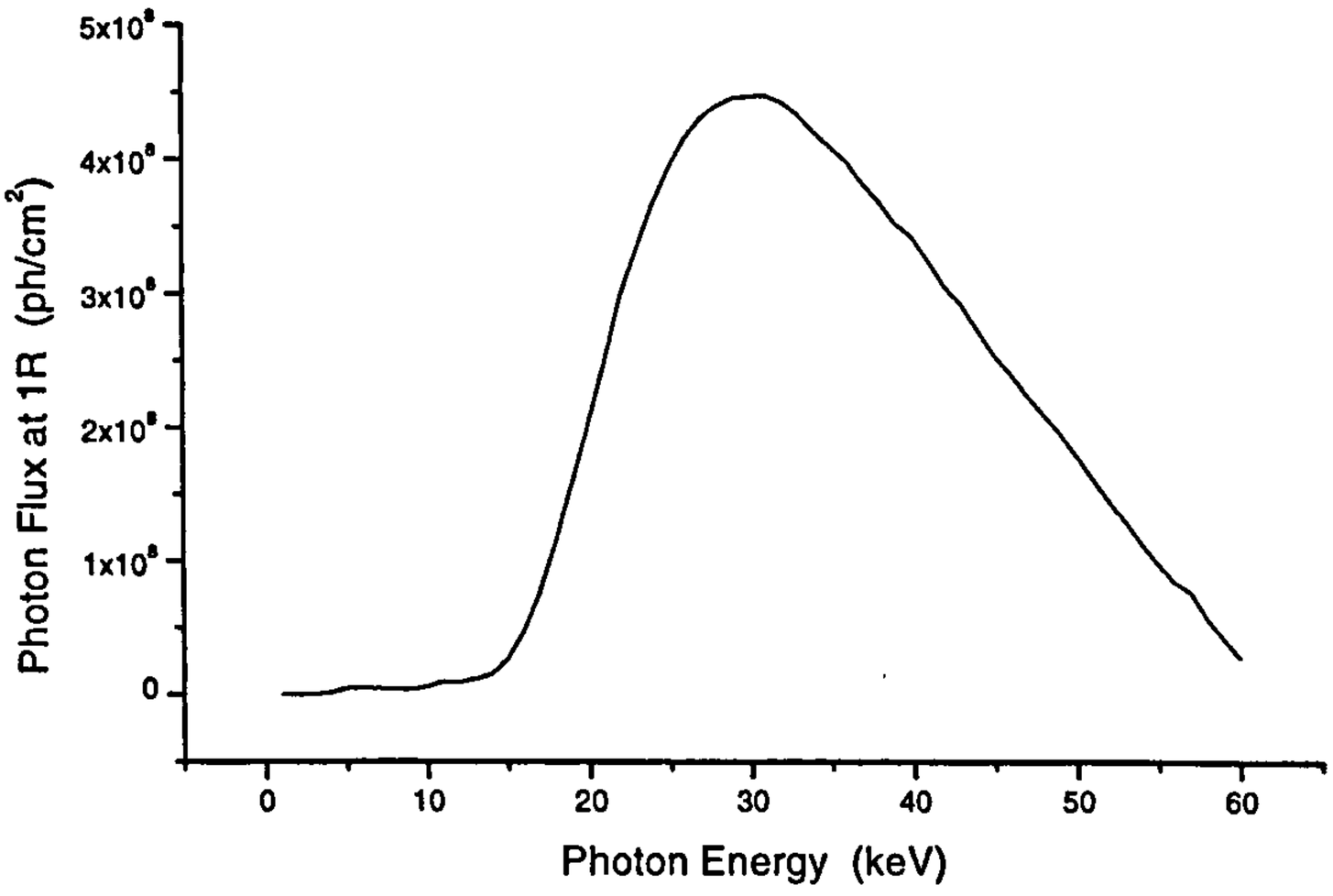

Figure 3.5: Photon flux calibration for the Planmeca Prostyle Intra X-ray gun at 1R exposure with 60kVp anode voltage.

at 60kVp [47]. Figure 3.5 shows the manufacturer's measurement of the photon flux as a function of energy at 1R (8.7mGy) exposure [48]. The peak energy lies around 30keV, with no flux recorded below 15keV. The tube is susceptible to "on-time" errors which make low fluence measurements erratic, and the PCC1 motherboard may be affected by increasing amounts of electromagnetic noise, degrading the detector performance at high flux [49].

3.2 Readout chip performance

The performance of the PCC1 is determined by the chip's response to a known external stimulus. For optimising electrical performance, the readout chip is supplied with a known number of pulses of varying amplitude and frequency from a pulse generator. The bias voltages are adjusted to give the best results from this test. In this way, the V_{bias}, V_{comp} and V_{dl} may be set.

3.2.1 Threshold scan

The pulse generator is programmed to provide 1000 pulses to the test input of each pixel cell. The width and period of these pulses are set in the software. The pulses have a period of 37μs, with 1000 pulses occurring in about 36ms. The timing between the 1000 bunches is about 50ms. The amount of charge deposited is determined by the pulse width, which for the VME system is set to 200ns. If the test input capacitance is known, an equivalent amount of deposited electrons may be easily calculated. A plot of the number of responding pixels against test pulse height yields a Gaussian distribution of pixel thresholds, the mean of which may be used to measure how well the detector is performing.

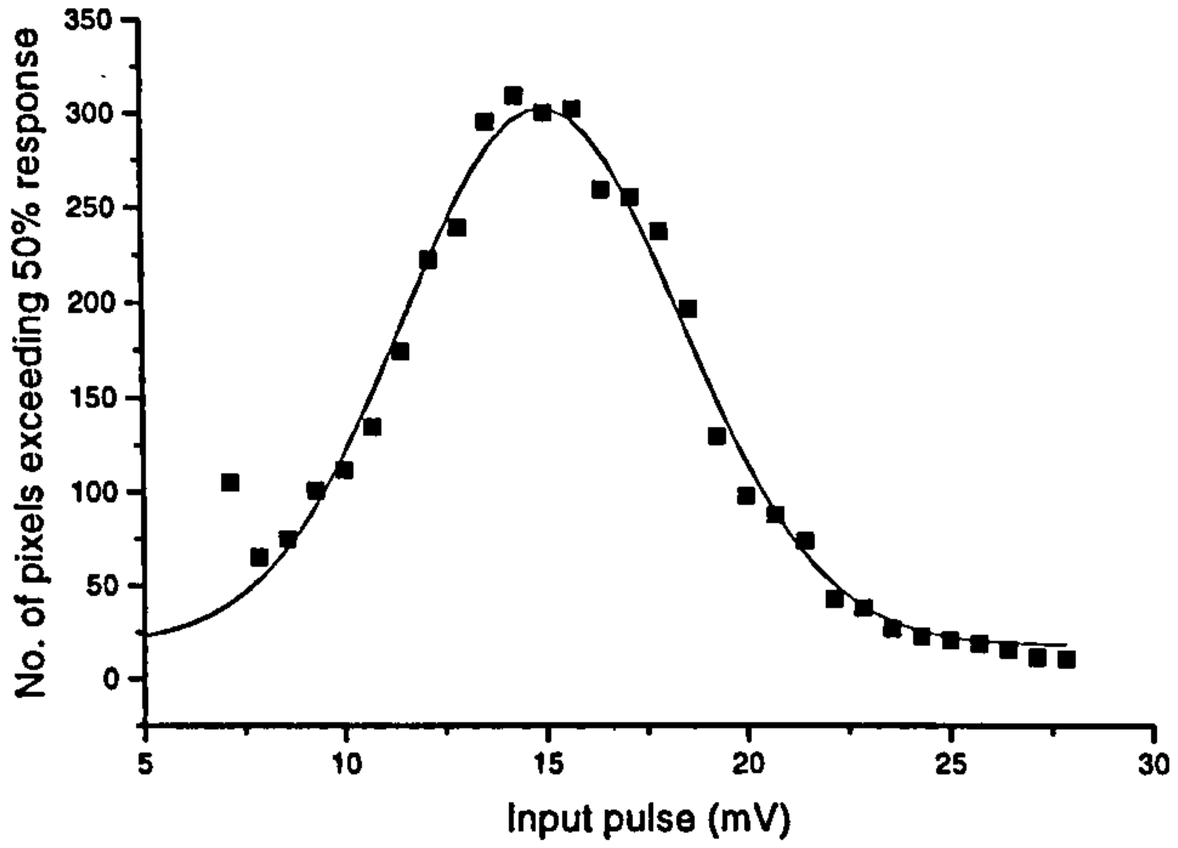

Figure 3.6: Plot of the threshold distribution of chip 4K. A Gaussian curve is fitted with a mean of approx. 15mV

Minimum threshold

A value for V_{th} (the comparator threshold) is determined by varying this value with no external stimulus, and looking for the point where the matrix becomes noisy. In this case, the V_{th} cut-off point was when 10% of the matrix was counting above 2 counts with no input pulse.

At this V_{th} value, the response of the chip to increasing test pulse height was measured. The test pulse range was typically from 8 to 40mV for an unadjusted chip. A pixel was defined to have responded when the count returned exceeded 50% of the total pulses given to the pixel (i.e. 1000). A pixel was defined as noisy if it exceeded 1002 counts (i.e. 2% over the maximum). The best operating point is the value that gives the lowest mean value of the distribution, with the lowest variance, achieved by varying V_{comp} and V_{bias}, although V_{bias} will give the greatest difference while there is no detector attached. V_{dl} is also determined in this way, and often manifest double counting is an indication that V_{dl} is too high.

Figure 3.6 shows the minimum threshold achieved with readout chip 4K (from the 1st fabrication run). The mean corresponds to approximately

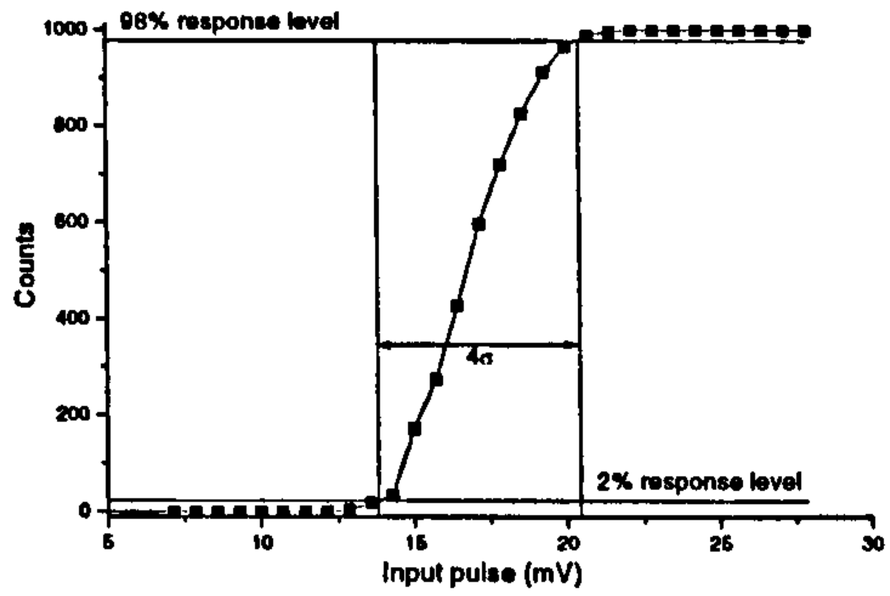

(a) S-curve response of a single PCC1 pixel. The 2% and 98% levels are marked for ENC calculation

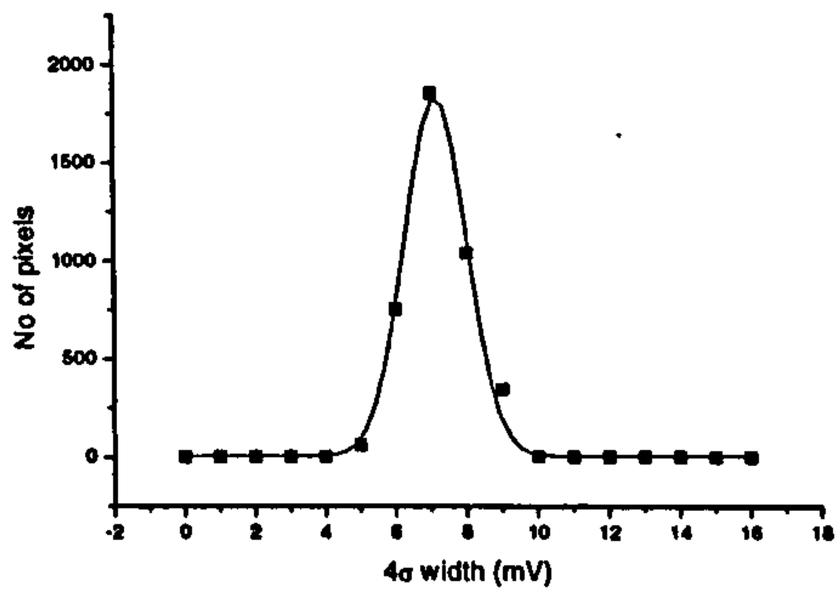

(b) Plot of the distribution of the width of the 2% to 98% response levels for all pixels in the matrix. The mean width gives a σ of approximately 1.8mV corresponding to an ENC of about 170e-.

Figure 3.7: ENC calculation.

1400e$^-$ with a variation of about 350e$^-$. This corresponds to about 5.1keV in silicon and 5.8keV in GaAs. An input charge of 80000e$^-$ (290keV in Si, 336keV in GaAs) was later applied with no performance degradation. The values of number of electrons are calculated assuming an input capacitance of 14.9fF and silicon as a detecting medium.

ENC

The total electronic noise may be calculated by examining the response of the matrix to increasing calibration pulse heights on a pixel-by-pixel basis. The response of one pixel is shown in figure 3.7(a), with the difference in input signal between 2% and 98% response corresponding to 4σ of the noise distribution. Taking all the pixels into account (figure 3.7(b)), the mean width of the 4σ is about 7.2mV giving an ENC of approximately 170e$^-$ using the 14.9fF test capacitor estimate. The ENC noise is dominated by the comparator noise.

Maximum pulsing frequency

The time delay between pulses from the pulse generator was decreased to observe the maximum counting frequency of the PCC1 chip. The chip was successfully pulsed up to a frequency of 2MHz with no loss of electrical performance. Above this frequency the PCC1 had difficulty resolving each individual pulse because the comparator had not reset before the next pulse arrived ("pile-up").

3.2.2 Threshold adjust

The ever decreasing component size in hybrid semiconductor detectors means an increase in the amount of on-board logic that may be implemented on the readout chip. Of the five configuration bits on board each pixel, three of them are reserved for a 3-bit threshold fine-tune. The concept behind this adjustment and the practical determination of the improvement achievable are outlined below.

Concept

The voltage V_{th} is set globally so that every pixel should have the same comparator threshold. This is not true in reality (see figure 3.6) due to small variations in V_{comp} and V_{bias} transistor dimensions [50]. Another fraction of global voltage (V_{tha}) is applied to each pixel in addition to the global threshold in steps of 0 to 7 (3 bits in binary). This value is written to the flip-flops prior to acquisition. The total threshold may then be given by the expression:

$$V_{total} = V_{th} + (0 - 7) \times (\frac{V_{tha}}{8}) \tag{3.1}$$

This should at best give a factor of 8 improvement in the width of the threshold distribution. During normal, non-adjusted operation the flip-flops contain a zero, giving no extra threshold above the global V_{th} level.

Determination of adjustment

The minimum threshold is determined in the manner described above to find a value for V_{th}. To quantify the amount of adjust a certain value of V_{tha} gives, the adjust bits are loaded with a 7 (maximum adjust), and then a pulse height scan is performed. The resulting distribution is still Gaussian, but moves up in mean threshold (some widening of the distribution is observed also). The idea is to choose a value of V_{tha} which allows the upper 1/8th of the zero-adjusted distribution to overlap with the lower 1/8th of the "seven-adjusted" distribution. At this point it can be reasonably assumed that all the pixels in the distribution will have a value of adjust that will fall in that region. The distributions for adjusts between 1 and 6 are measured once the correct value of V_{tha} has been determined.

A range is chosen over which the thresholds are to be adjusted. This value must be greater than or equal to 1/8th of the width of the original distribution, as a factor of 8 improvement is the limit of the adjust. A pixel-by-pixel analysis of the response across all adjust values yields an adjust value which causes the pixel threshold to fall in the predetermined region. A complete threshold adjust map is then created, which may be loaded onto the PCC1.

Results

Figure 3.8 shows the effect of the threshold adjust on the threshold scan. The 0 and 7 adjust responses are shown for a V_{tha} value of 0.72V. The tuned threshold distribution is shown in the middle of the 0 and 7 distributions, and gives a variation of about 80e^-s at a mean of approximately 23mV (2150e^-s). The value of V_{th} may be lowered to give a lower mean threshold, at the expense of widening the variation slightly [42].

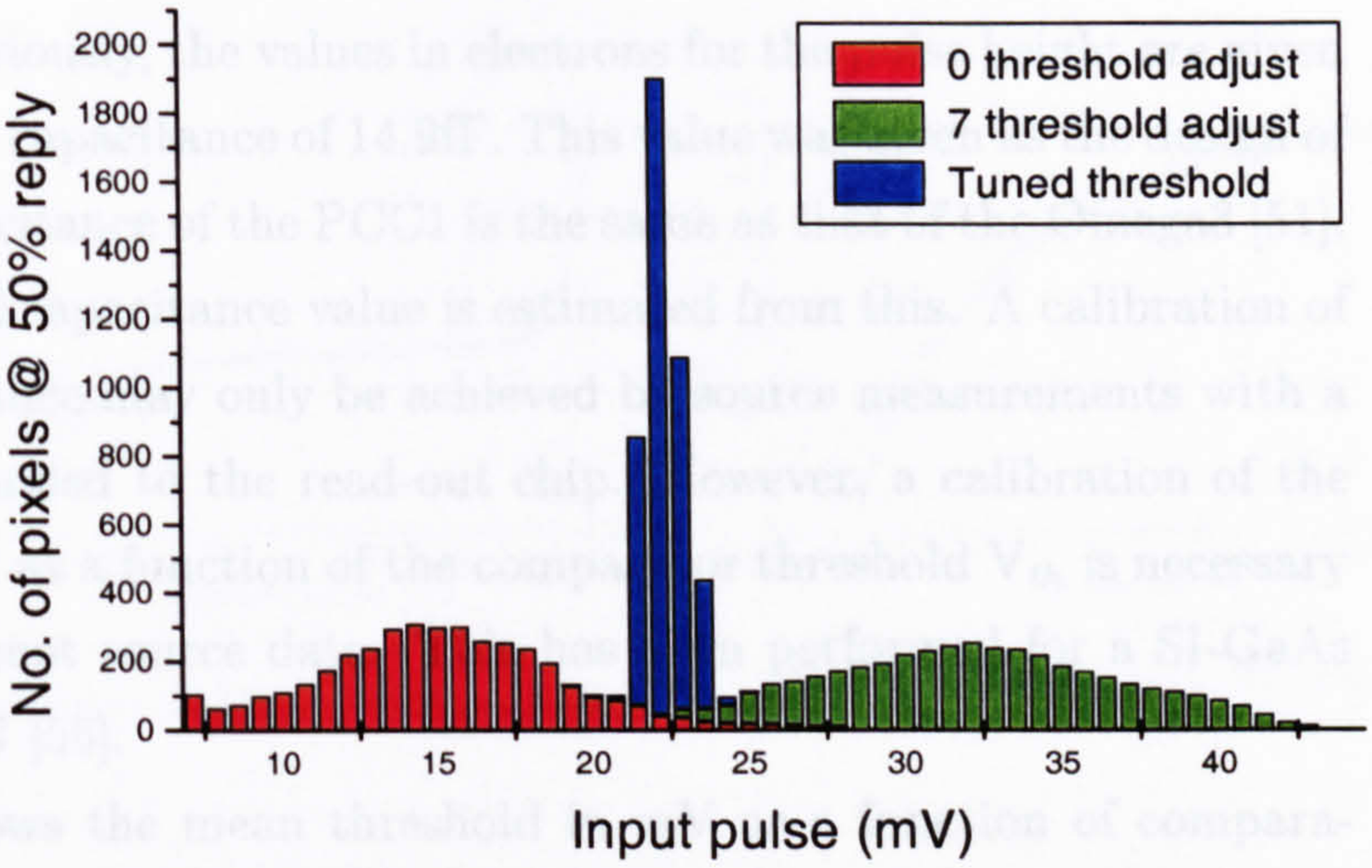

Figure 3.8: Threshold scan with 0 adjust, 7 adjust, and 3-bit tuned threshold map applied. Note the approx. 1/8th overlap between the 0 and 7 scans.

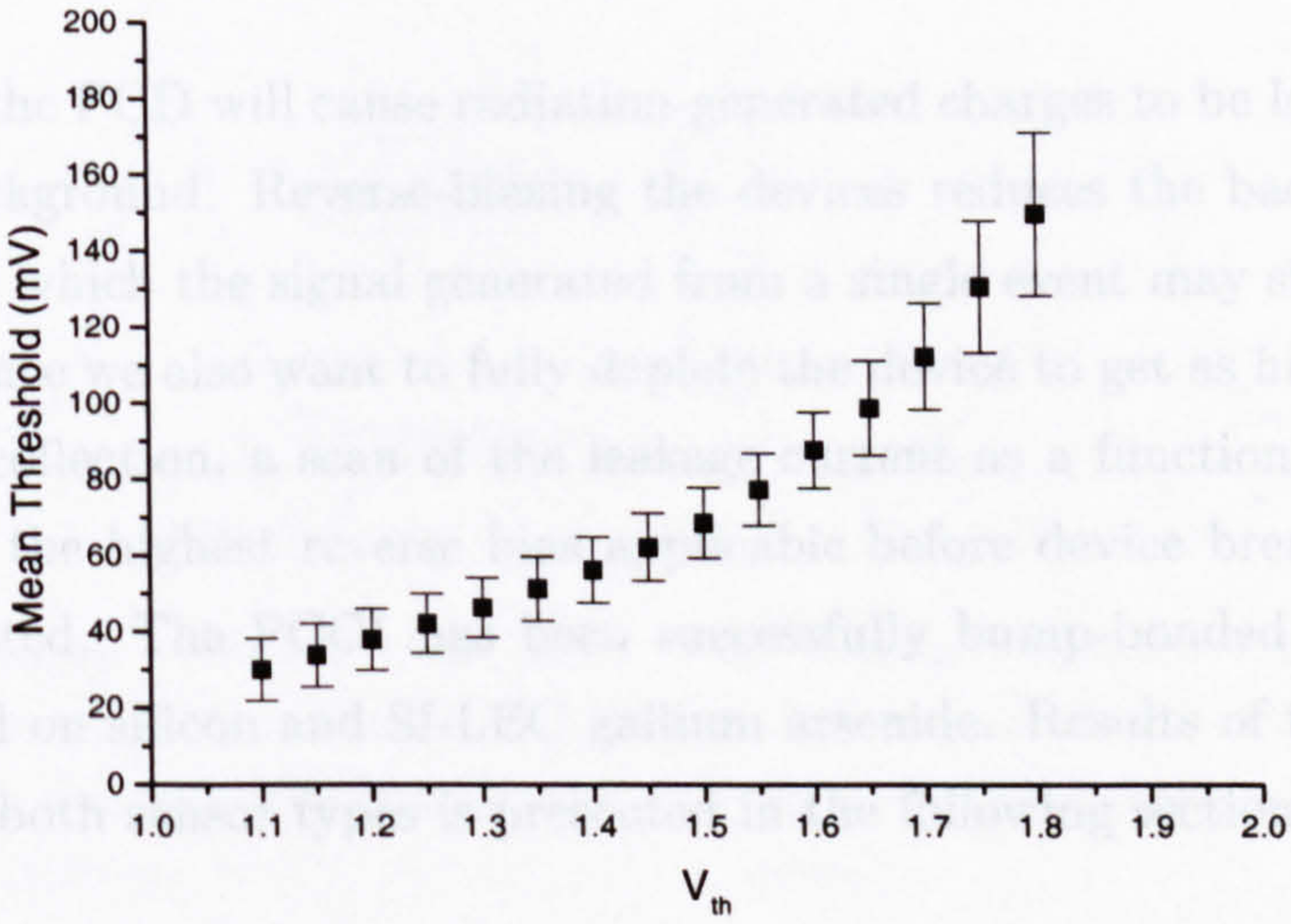

Figure 3.9: Calibration curve of mean pixel input pulse threshold in mV as a function of comparator threshold V_{th}.

3.2.3 Test capacitor calibration

As mentioned previously, the values in electrons for the pulse height are given assuming an input capacitance of 14.9fF. This value was given as the design of the front end capacitance of the PCC1 is the same as that of the Omega3 [51], and the calculated capacitance value is estimated from this. A calibration of the input capacitance may only be achieved by source measurements with a detector bump-bonded to the read-out chip. However, a calibration of the input pulse height as a function of the comparator threshold V_{th} is necessary to fit any subsequent source data. This has been performed for a SI-GaAs detector at CERN [55].

Figure 3.9 shows the mean threshold in mV as a function of comparator threshold V_{th} for an unadjusted chip (P24). The ordinate scale will be calibrated in terms of electrons deposited in silicon subsequent to a source calibration as described in section 3.3.2.

3.3 Detector performance

Leakage current in the PCD will cause radiation-generated charges to be lost in a high signal background. Reverse-biasing the devices reduces the background to a level at which the signal generated from a single event may still be resolved well. Since we also want to fully deplete the device to get as high as possible charge collection, a scan of the leakage current as a function of bias voltage allows the highest reverse bias applicable before device breakdown to be calculated. The PCC1 has been successfully bump-bonded to detectors fabricated on silicon and SI-LEC gallium arsenide. Results of the characterisation of both sensor types is presented in the following section.

3.3.1 Detector measurements

Figure 3.10 shows the I-V characteristics of a GaAs and a Si detector. The leakage current from the detector is a good indication of the reverse bias

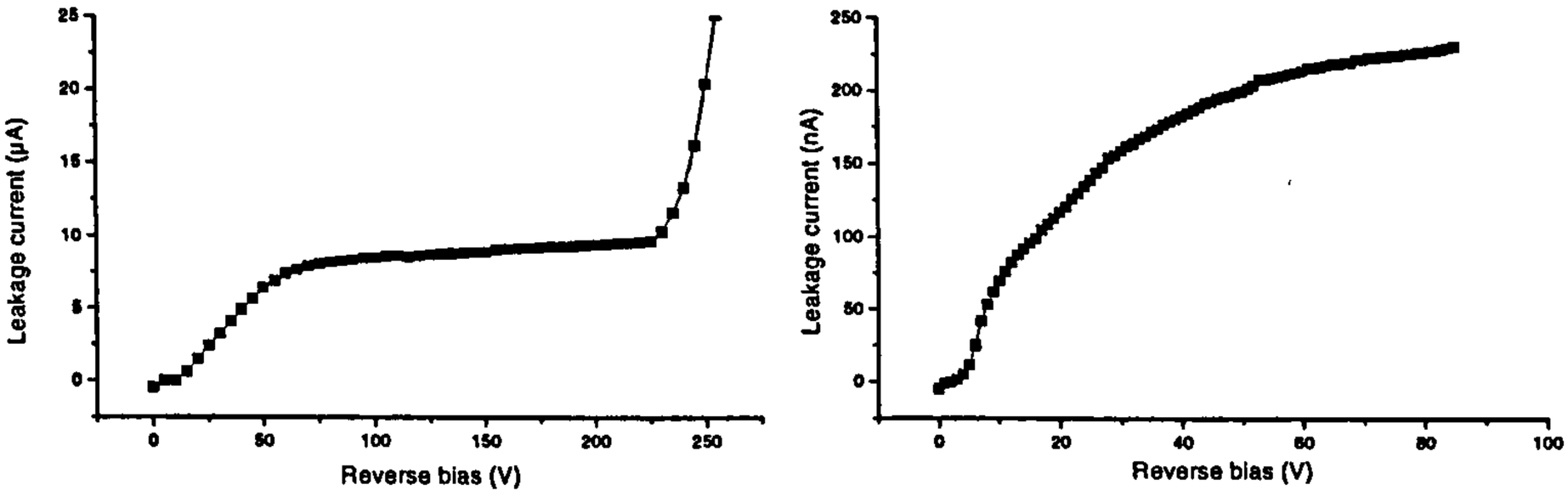

(a) Detector 06G0-7I (200μm SI-GaAs).

(b) Detector P24(5D) (300μm Si)

Figure 3.10: IV characteristic curves for GaAs and Si detectors.

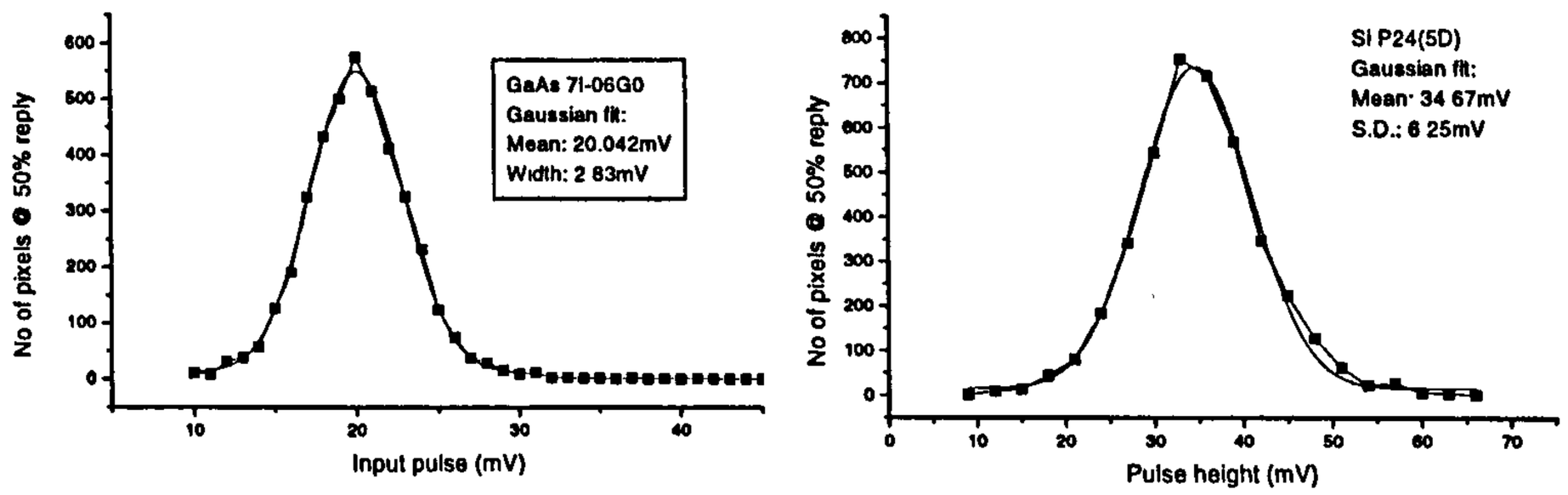

(a) Detector 06G0-7I (SI-GaAs 200μm) at 230V reverse bias. The minimum threshold has increased to 20mV (2300 e-).

(b) Detector P24(5D) (300μm Si) at 80V reverse bias. The minimum threshold has increased to 34mV (4000e-)

Figure 3.11: Threshold scan (unadjusted) for GaAs and Si detectors.

required to deplete the device fully, as it indicates the highest depletion possible before the leakage current increases to the point where imaging is impossible. Just before breakdown, one can be sure the device has reached it's maximum possible sensitive volume. An I-V scan of the leakage current as a function of reverse bias for a 200μm SI-LEC GaAs detector is shown in figure 3.10(a). The leakage current rises fairly rapidly from 0 to 7μA before levelling off to around 9μA at 230V reverse bias. Higher bias voltage leads to device breakdown and the leakage current rises steeply to a level which is unsuitable for particle detection. This is due to the electrons being accelerated by the electric field so much they cause impact ionisation, generating an avalanche of carriers. The 210V point was chosen for imaging because it provides the highest charge collection before breakdown. Good detectors with Non-Alloyed Ohmic Contacts [39][53] will reach voltages of up to 600V before breakdown.

Figure 3.10(b) shows the I-V curve for silicon. The leakage current is over an order of magnitude less than in SI-GaAs due to the better stability and homogeneity of Si detectors. An operating voltage of 80V reverse bias is enough to achieve approximately 100% charge collection efficiency.

After bump-bonding, the effect of the reversed-bias detector on the mean threshold was investigated by performing a threshold scan in the manner described in section 3.2.2. Figure 3.11(a) shows the mean threshold for the chip moving up to approximately 20mV, and figure 3.11(b) shows the Si assembly responding with a mean threshold of over 30mV. The degradation of the silicon detector is discussed in section 4.3 (Desputtering). With the Si assembly, the application of a reverse bias across the detector does not increase the threshold significantly from the readout chip calibration due to the low noise of the biased silicon detector.

Figure 3.12 shows the mean counts recorded as a function of reverse bias voltage for GaAs and Si. Both detectors were illuminated with the Planmeca dental X-ray tube at 60kVp, with a source-detector distance of 55cm. The SI-GaAs shows a region of low noise near breakdown corresponding to com-

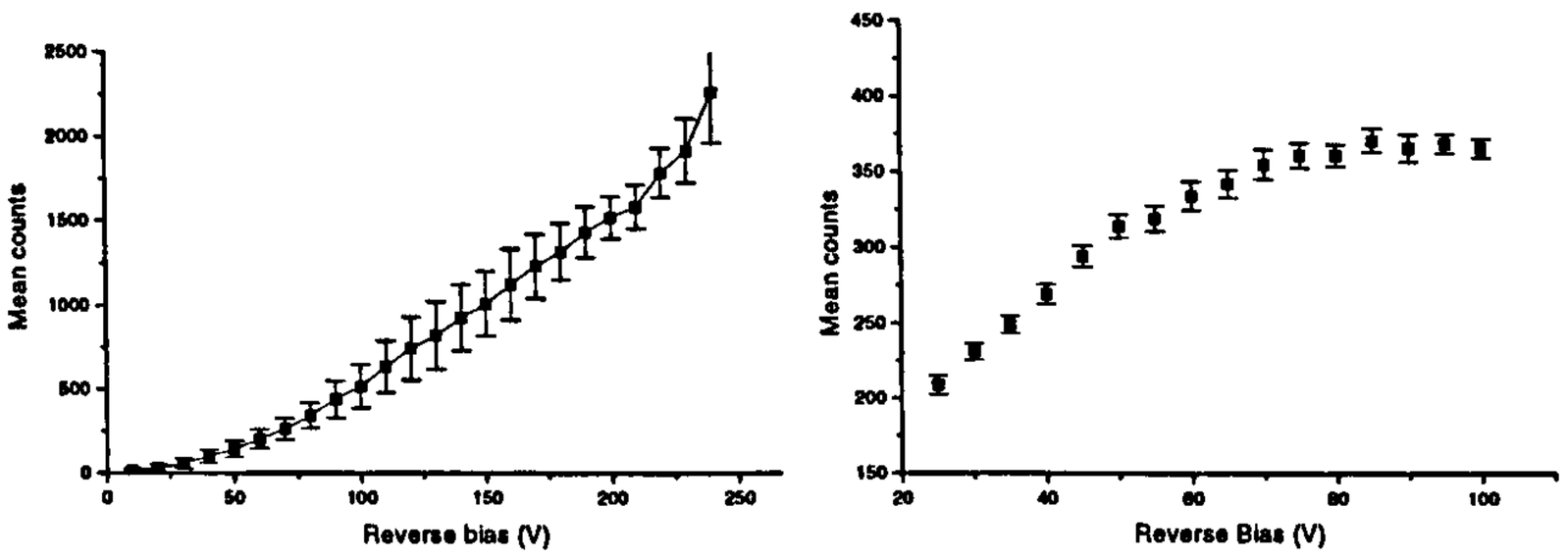

(a) Detector 06G0-7I (SI-GaAs 200μm) mean response at 8mR (64 μGy).

(b) Detector P24(5D) (300μm Si) mean response at 4mR (32 μGy).

Figure 3.12: Mean counts across the pixel matrix as a function of bias voltage for SI-GaAs and Si.

plete depletion which is the best imaging operating point. The silicon slowly plateaus to full depletion after about 60-70V.

3.3.2 Absolute calibration

To characterise the PCC1 a relation between the test signal and the actual charge injected from the detector must be established. The value of the test capacitance was determined using radioactive sources with known gamma energies [54], and scanning through the comparator (V_{th}) values to link the input pulse in mV to the actual charge detected in electrons. The procedure was to start with a low threshold at which all the photons from the source would be counted, and then to move the threshold up in small steps until a drop in counts was seen. This corresponds to a point just above the main energy peak, and after differentiation will show a peaked differential pulse height distribution as a function of comparator threshold. The position of the peak corresponds to the energy of the K X-ray, or the "end-point". The value of V_{th} which corresponds to the gamma end-point may be compared to the mean threshold in mV achieved with the test signal. Comparing the known

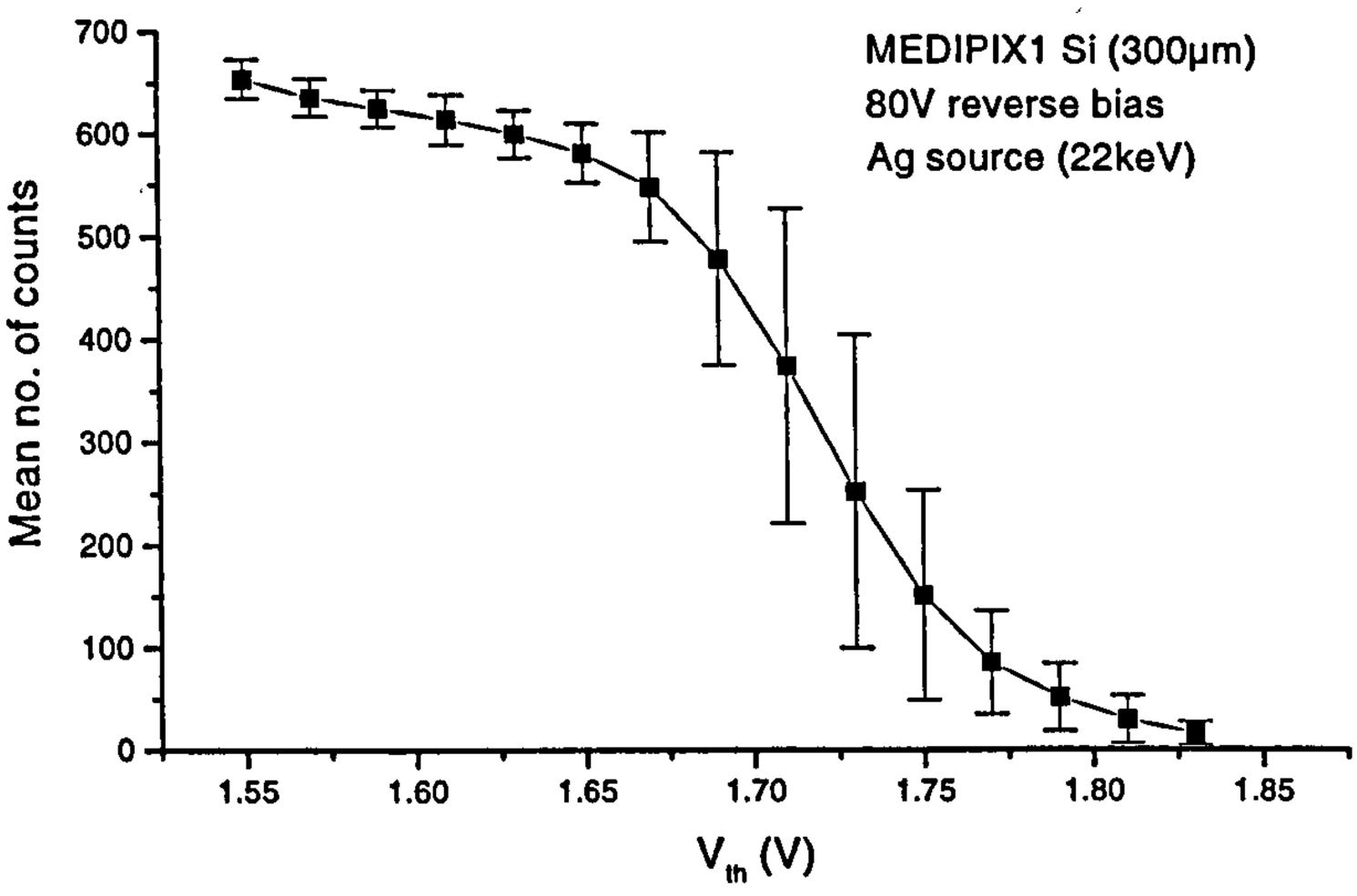

Figure 3.13: S-curve response of the detector to a flood Ag K X-ray source as a function of comparator threshold.

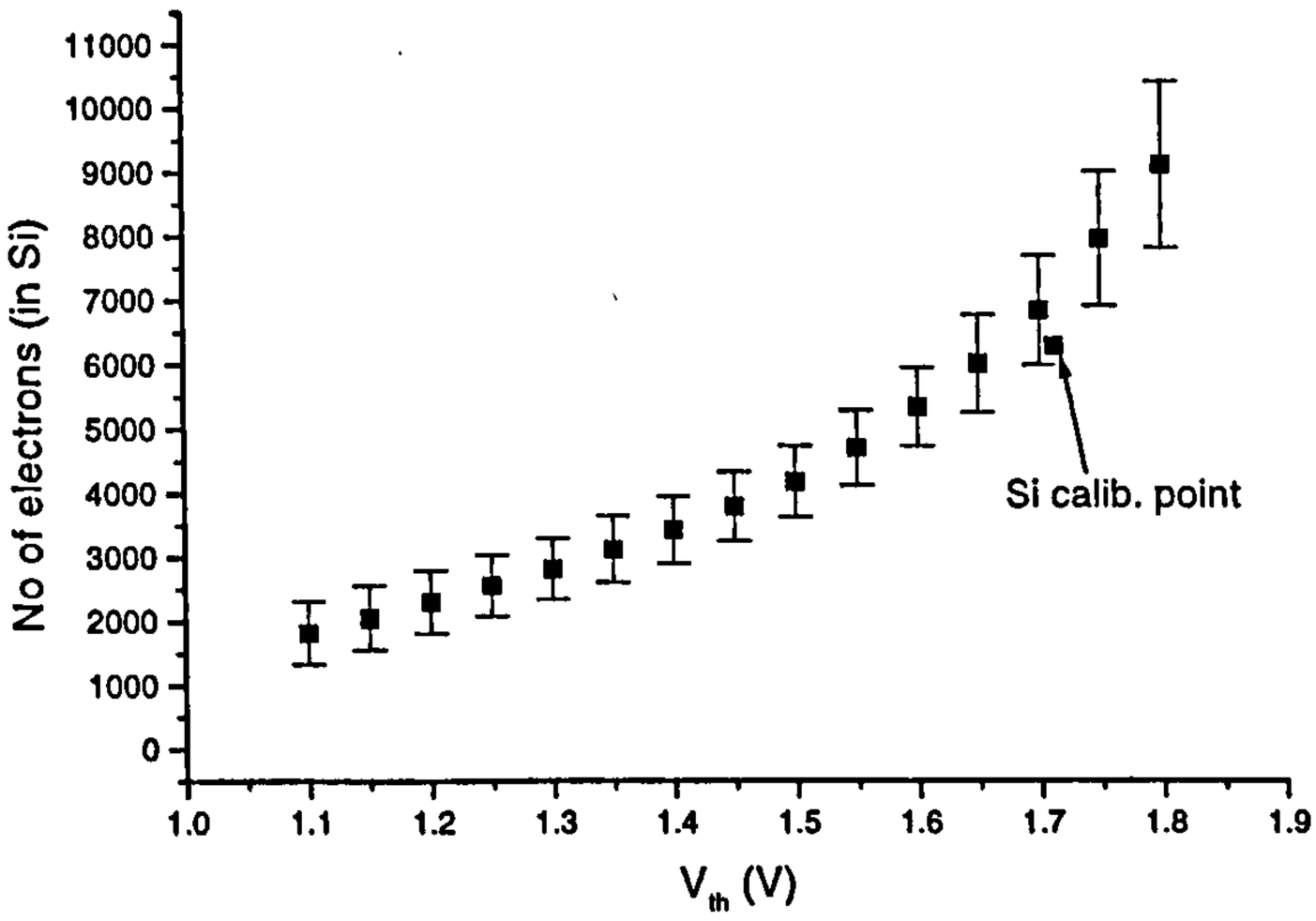

Figure 3.14: Threshold calibration from figure 3.9 with source end-point.

charge detected and the test pulse height will yield the input test capacitor value (using $Q = VC$). The end-points are determined on a pixel-by-pixel basis (similar to the ENC calculation) and the average value of the input test capacitor may be calculated assuming a charge collection efficiency relevant for the material. The design value of the test capacitance is given as 20fF.

The system noise increases the width of the energy peak, so the value determined by the above method will be a best case estimate. Subtracting the system noise will raise the test capacitor value. A value for the input test capacitor has been determined for a SI-GaAs detector [55] (assuming a CCE of 89%) yielding a test capacitor value of approximately 24.7fF (after a system noise of 250 e^- was subtracted). This may be assumed as an overestimation due to the shaping time assumed for the GaAs (1μs) being more than the shaping time of the PCC1 (150ns), and consequently some signal may be lost.

A calibration for a silicon detector will prove more accurate due to the high uniformity, operational stability and charge collection efficiency of 100%. Figure 3.13 is a plot of the mean counts achieved with the Ag source as a function of comparator threshold. The large error bars are due to the relatively low statistics with the variable X-ray source and a 50% level of 1.72V for V_{th} was estimated. This curve may be differentiated to determine the source end-point. Figure 3.14 shows the threshold calibration from figure 3.9 with the end-point estimated above for a silver source (K_α=22.1keV) fitted to the curve, which has been rescaled in terms of the amount of charge liberated in silicon. A charge of approximately 6000 electrons at the end point of around 100mV yields a test capacitance value of 10fF, which is low compared to the result achieved with GaAs. The electrical performance of the P_24 chip was borderline rejection (according to the chip selection criteria stated in section 3.4.1), requiring a high threshold to exclude the extra signal provided by the low input capacitance.

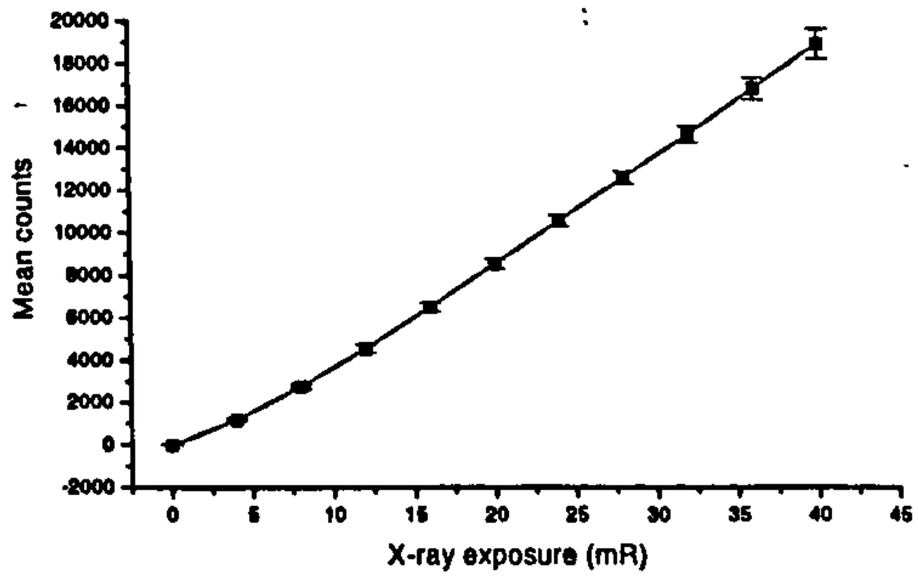

(a) Detector 06G0-7I (SI-GaAs 200μm) at 210V reverse bias (no threshold adjust).

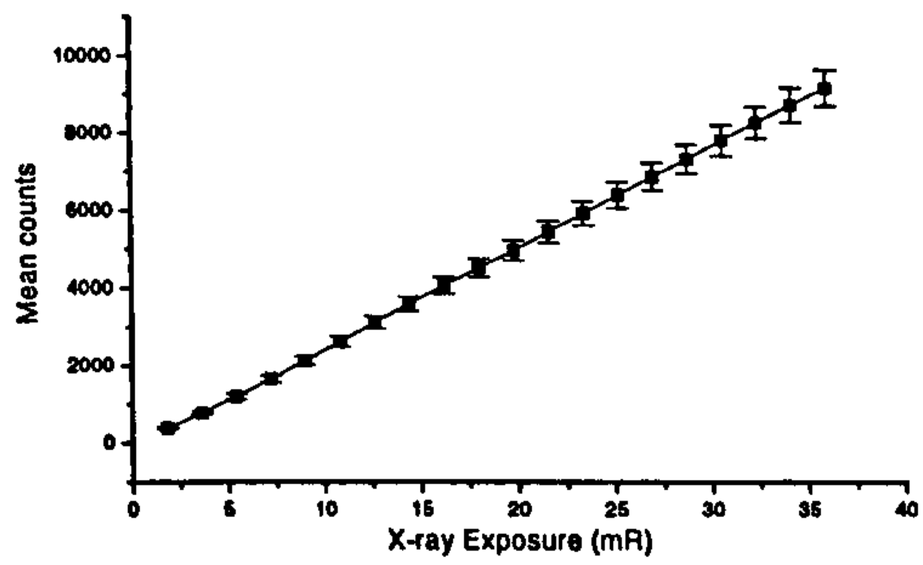

(b) Detector P24(5D) (Si 300μm) at 80V reverse bias (no threshold adjust).

Figure 3.15: Sensitometric curves for SI-GaAs and Si.

3.3.3 Sensitivity

The dose response of a photon counting system should be linear across the whole dynamic range. Figure 3.15 shows the mean number of counts across the whole matrix as a function of X-ray exposure. The standard deviation in the mean (noise) is shown on the error bars. At 60 kVp, the Planmeca X-ray gun delivers approximately 1.2×10^{10} photons/cm^2/R [48], which for the PCD corresponds to 347 photons/pixel/R. The images were median filtered with a 3x3 kernel to improve the noise.

The gallium arsenide detector shows a linear response above 3mR (24 μGy), with a photon detection efficiency of 49% (measured at 20mR (160μGy)). The silicon response is also linear, with a detection efficiency of 28%. The silicon detector suffers from poor photon absorption above 20keV resulting in a lower number of counts per pixel than in the GaAs. However, the noise level in silicon is still better than in GaAs due to the high number of defects in bulk SI-GaAs.

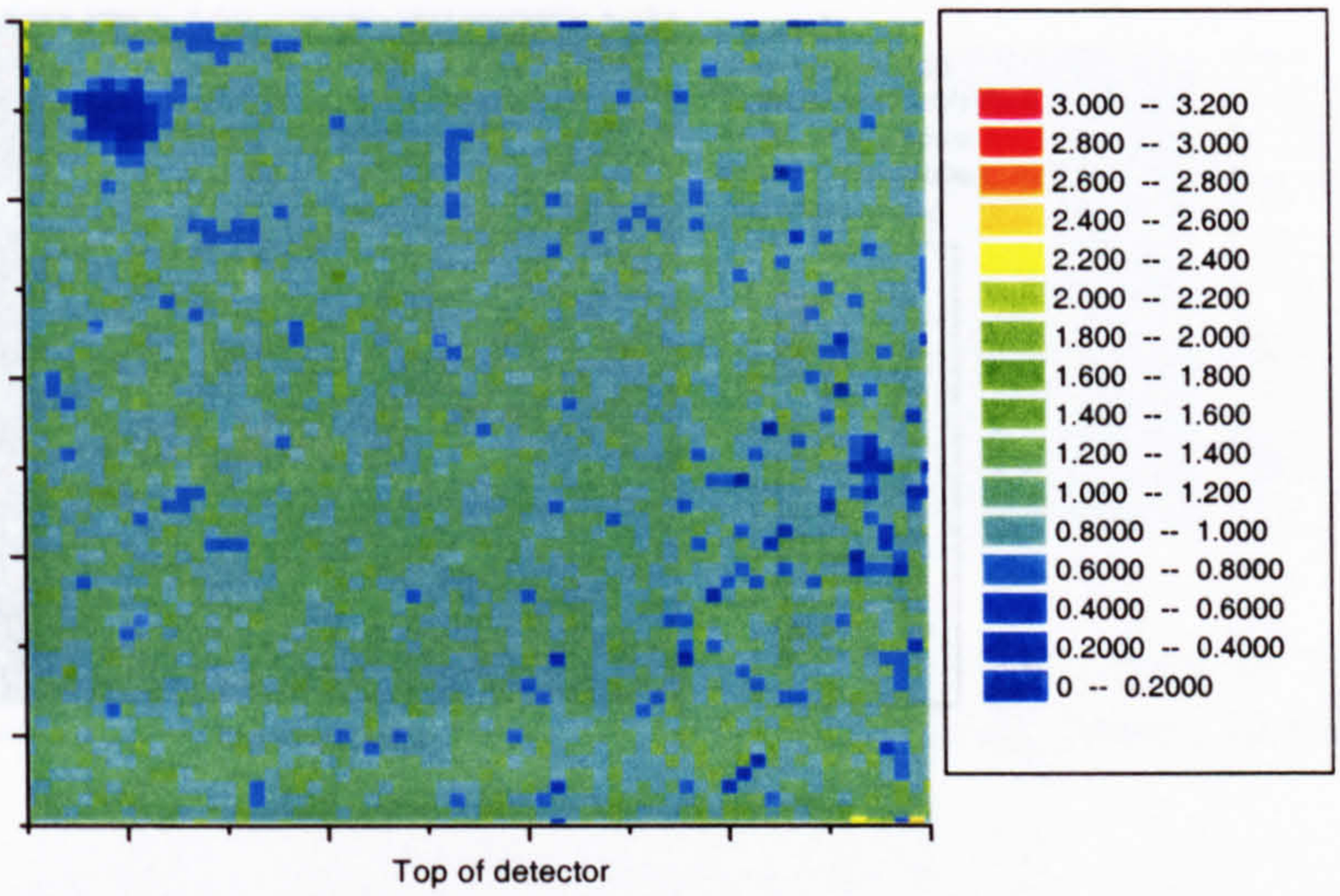

Figure 3.16: Gain map calculated for 30 consecutive exposures of detector 7I-06G0 (250μm SI-GaAs) at 20mR (160μGy).

3.3.4 Optimisation

The principle of threshold adjust has been discussed above as a means of smoothing pixel-to-pixel variations across the sensor matrix. This adjustment is fine for the readout chip, however it has little effect on more macroscopic inhomogeneities within the detection medium. This is especially true in GaAs, where the large number of trapping centres means that there may be areas of the sensor where the material itself is distorting the signal seen by the electronics, resulting in a poor image quality. The gain map is calculated by taking a large number (more than twenty) of *flood* images under identical dose conditions and calculating a pixel-by-pixel mean, and a mean across the whole matrix. The deviation of each pixel from the global mean may be calculated which yields a multiplication factor map which may be applied to bring each pixel to the global mean value. In this way, areas of the matrix with too low or too high a response may be identified and a geography of the matrix response may be plotted.

The gain-map correction was performed on chip no. 7I (SI-GaAs), taking

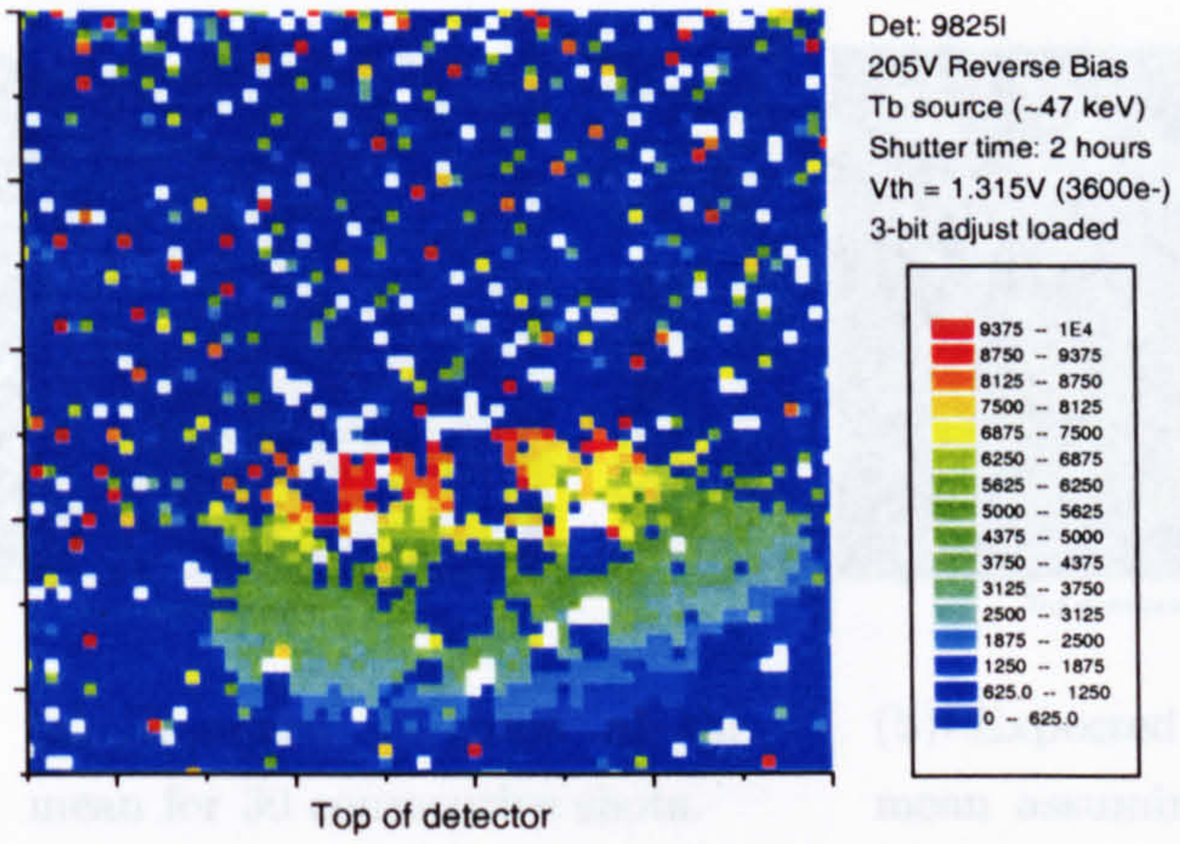

Figure 3.17: Plot of mean count per pixel for 30 identical acquisitions.

30 consecutive exposures at 20mR (160 μGy). The signal-to-noise ratio for the fixed pattern noise before gain map correction was 6.67. Figure 3.16 shows the gain map calculated from these 30 flood images. The blue area near the top left is the small blob of solder bonding the HV supply to the rear side of the detector. Applying the gain map calculated from all 30 exposures, the signal-to-noise ratio improved to 13.5.

The gain map correction was observed to become redundant at higher doses, suggesting a dose dependent factor when applying the gain map. The converse was observed to be true, where a high dose gain map was applied to a low dose image. This effect may be better investigated using silicon detectors, and has been investigated for SI-GaAs before [57], with similar results.

3.3.5 Noise

A study of the uniformity of the response of a pixel across a number of consecutive acquisitions was made to investigate if there were any regions of the PCD exhibiting Poisson-limited noise behaviour. The detector used for this study was 9825I, which by the time of the experiment had degraded to

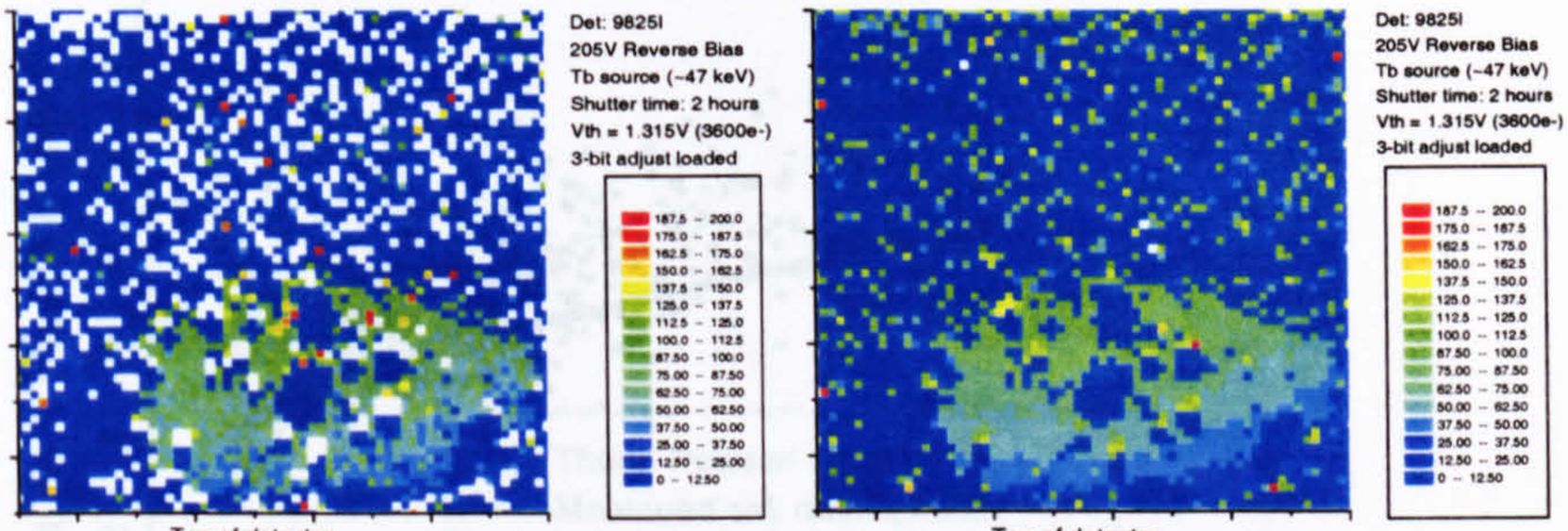

(a) Standard deviation of the mean for 30 consecutive shots.

(b) Expected deviation in the mean assuming Poisson limited noise.

Figure 3.18: Plots of the variation across the pixel matrix for real and ideal noise.

a device with a sensitive area of about a third of the entire matrix. Reasons for this degradation are given in section 3.4.2, however the good area was still large enough to image with a large number of pixels. The detector was operated at 205V reverse bias, with a Tb source (47 keV) illuminating the back side for 1 hour per image. Figure 3.17 shows the mean response of each pixel over the 30 acquisitions, with the active area containing regions of no response that are about 3 pixels by 3 pixels in size.

The response of each pixel over the 30 acquisitions was measured by plotting the standard deviation in the mean of each pixel in the same way as figure 3.18(a). There appear to be areas just outside the dead zones where the pixels fluctuate a large amount through the images (appearing as white areas). By plotting the square root of the means in figure 3.17, the actual noise per pixel may be compared with the ideal situation of Poisson limited noise (figure 3.18(b)).The plots in figure 3.18 show similar bad areas and an overall similar noise level, with the actual noise just higher than the quantum noise. Figure 3.19 shows the theoretical and measured noise in the good region of the detector on the same plot for comparison.

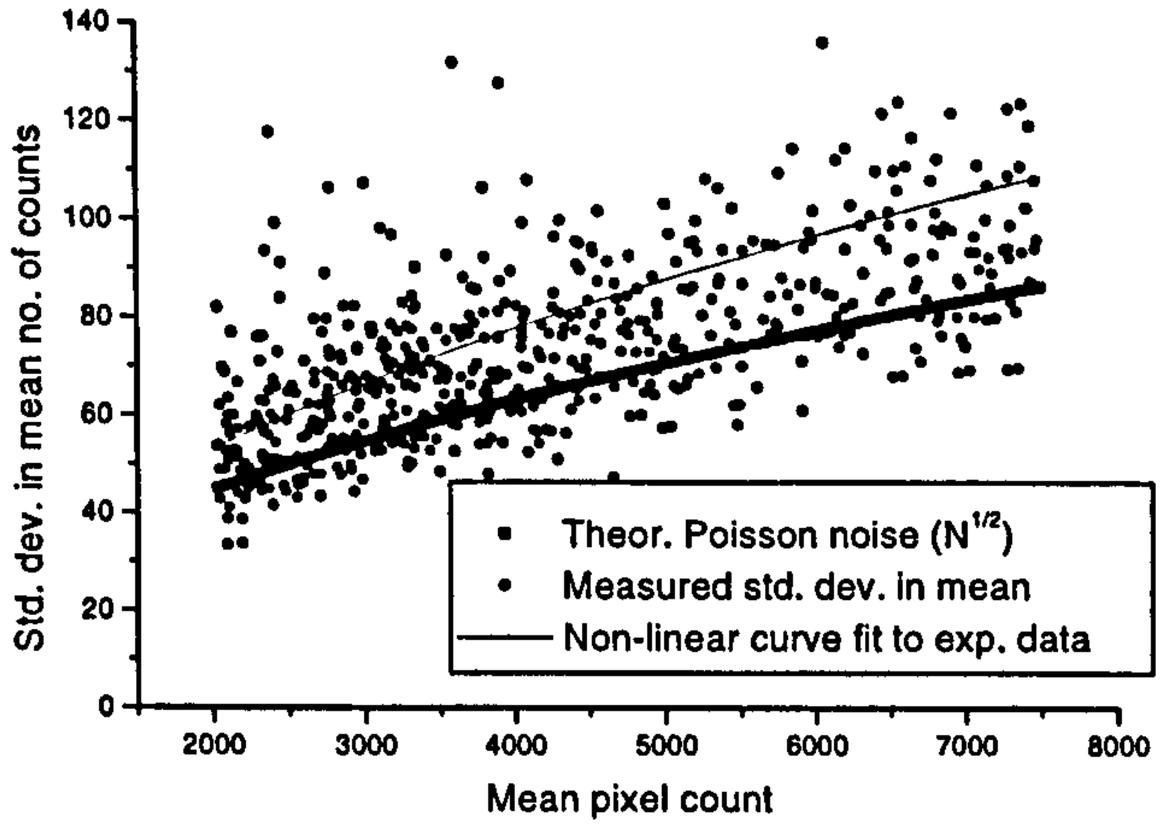

Figure 3.19: Plot of the expected and measured standard deviation for a mean pixel count N.

3.3.6 Spatial resolution

The Modulation Transfer Function for GaAs and silicon was measured by the Freiburg group [58]. Using a 20μm slit, a line spread function was determined, and an MTF calculated using the LSF. An MTF of approximately 4.4 lp/mm at the 30% level is found for both silicon and GaAs (c.f. figure 3.21). The MTF is poorer than most commercial digital imaging systems due to the large pixel size. A comparison with other systems has been made by Irsigler et al. [59] and is shown in figure 3.21.

3.4 Image processing

A number of image processing algorithms may be applied to the PCD1 images to improve the noise performance or enhance certain features. In dealing with radiographic images, one requires a smoothing algorithm that smoothes Gaussian noise and eliminates noisy pixels, while still retaining the image boundaries (i.e. not smoothing out the edges). The best method for this type of image procesing is the median filter.

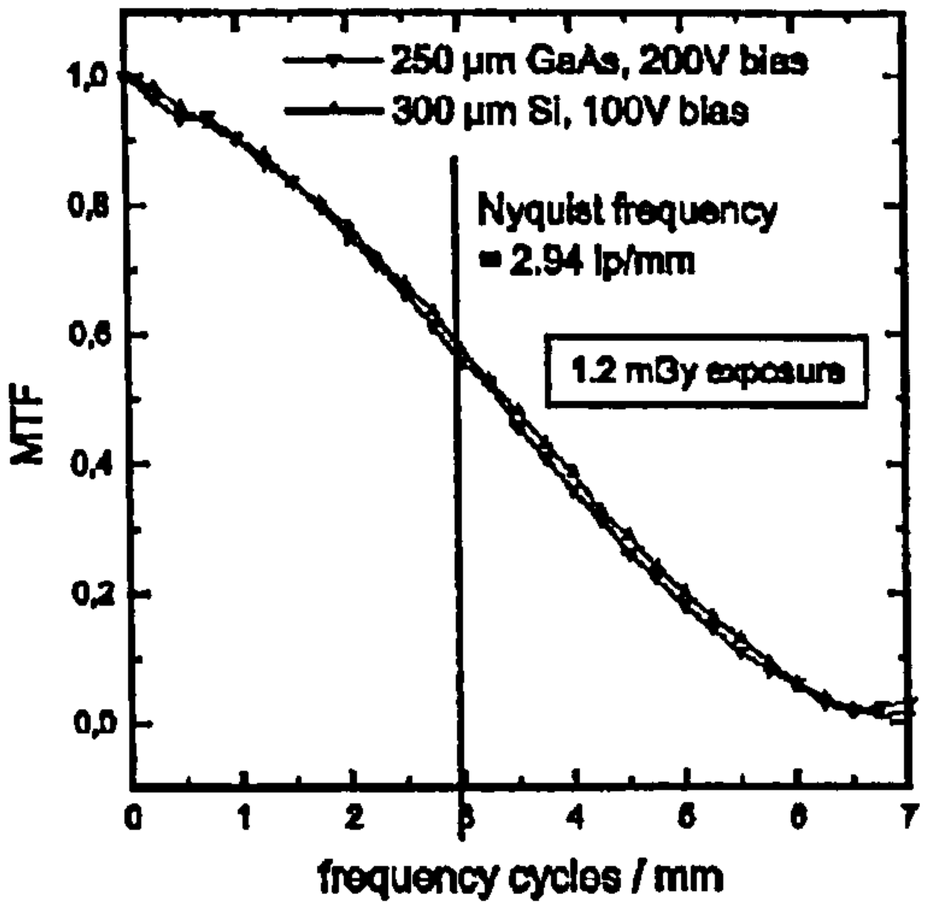

Figure 3.20: Modulation transfer function for a silicon and a GaAs PCD.

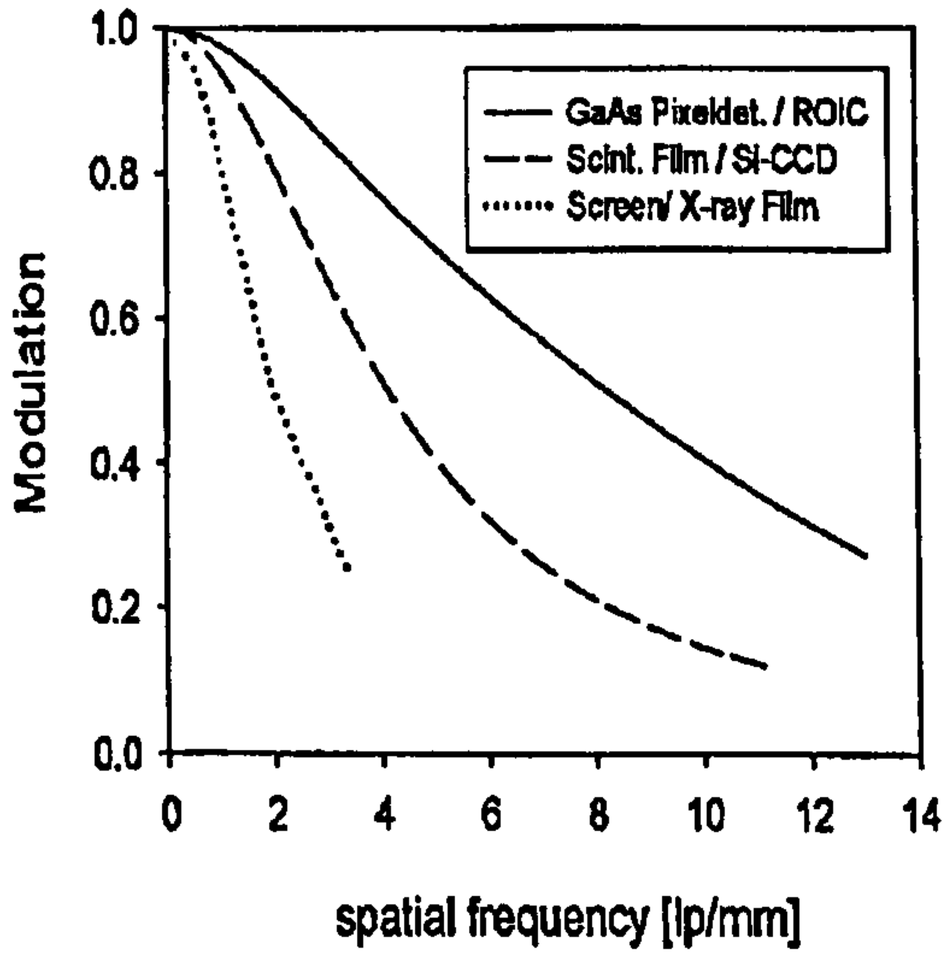

Figure 3.21: Modulation transfer function for other imaging systems. The SI-GaAs detector was a 240x320 array of 35μm square pixels bump-bonded to a charge integrating read-out chip developed for IR imaging.

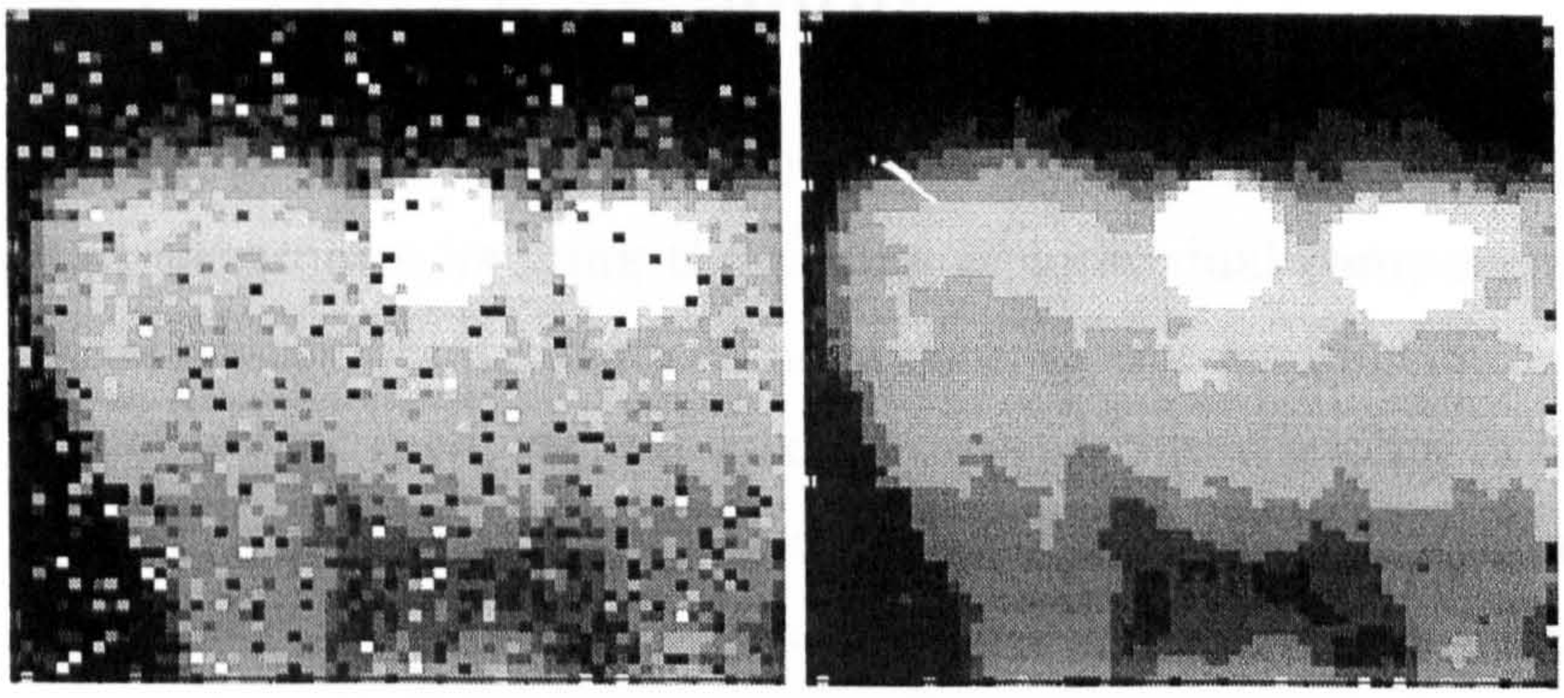

(a) Raw data image of a molar phantom.

(b) Image of molar phantom after application of a 3x3 kernel median filter.

Figure 3.22: Image of a tooth phantom with and without a 3x3 kernel median filter.

3.4.1 Median filter

The median filter works by taking the median value of the counts in a pixel and its neighbours. In a 3x3 kernel median filter, the counts in a pixel and it's surrounding 8 neighbours are listed in ascending order. The middle value in the list replaces the original central pixel count. This method pushes noisy or dead pixels to the extremes of the median list, and are unlikely to be the median value. Figure 3.22 shows a PCD image of a molar phantom illuminated with a 60kVp X-ray beam for 0.05 seconds. This corresponds to 30% of the normal dose required for imaging an adult molar [47]. The detector was 200μm SI-GaAs (9815B) operating at 210V. Figure 3.22(a) shows the unprocessed raw image from the PCD1, and figure 3.22(b) shows the image after the application of a 3x3 kernel median filter. It can be seen that the shape of the image remains intact, whereas the noisy pixels have been effectively masked. Bigger kernel sizes, however, lead to a reduction in edge resolution.

3.5 Device assembly

Hybrid pixel detectors by their nature allow separate optimisation of detector and electronics, making the testing of individual components of the system before assembly a reality. The testing of the readout chips before they are diced is described, including some tests on the reliability of the chip selection process and the performance of chips from a range of sites across the wafer. The bump-bonding process is described extensively in Humpston et al [14] and will not be expanded upon here, however some device degradation which may be due to this process has been seen and is discussed at the end of this section.

3.5.1 Wafer probing

The readout chips are fabricated on 6 inch wafers and are individually tested prior to flip-chip bonding. Digital and analog tests are performed to select Known Good Die, the contact with the readout chip being made with a specially designed probe card, which allows a temporary contact with the bonding pads to be established. Wafer probing was performed at CERN, Geneva and NIKHEF, Amsterdam.

Probe station setup

Figure 3.23 shows the probe station set-up at NIKHEF. The wafer is mounted on a vacuum plate under the microscope, and the plate is grounded to minimise noise. The microscope is required to line up the contact needles on the probe card with the readout chip bond pads, and may be programmed to step across the wafer automatically by a repeatable distance to speed up the probing process. Once aligned, the probe needles are lowered to make contact with the pads, usually with a small amount of overdrive to make effective contact with the chip. Figure 3.24 shows the mean threshold achieved with one chip (1G - wafer 10C3) at different probe needle heights. It can be seen that an overdrive of approximately 0.2mm is required to get reason-

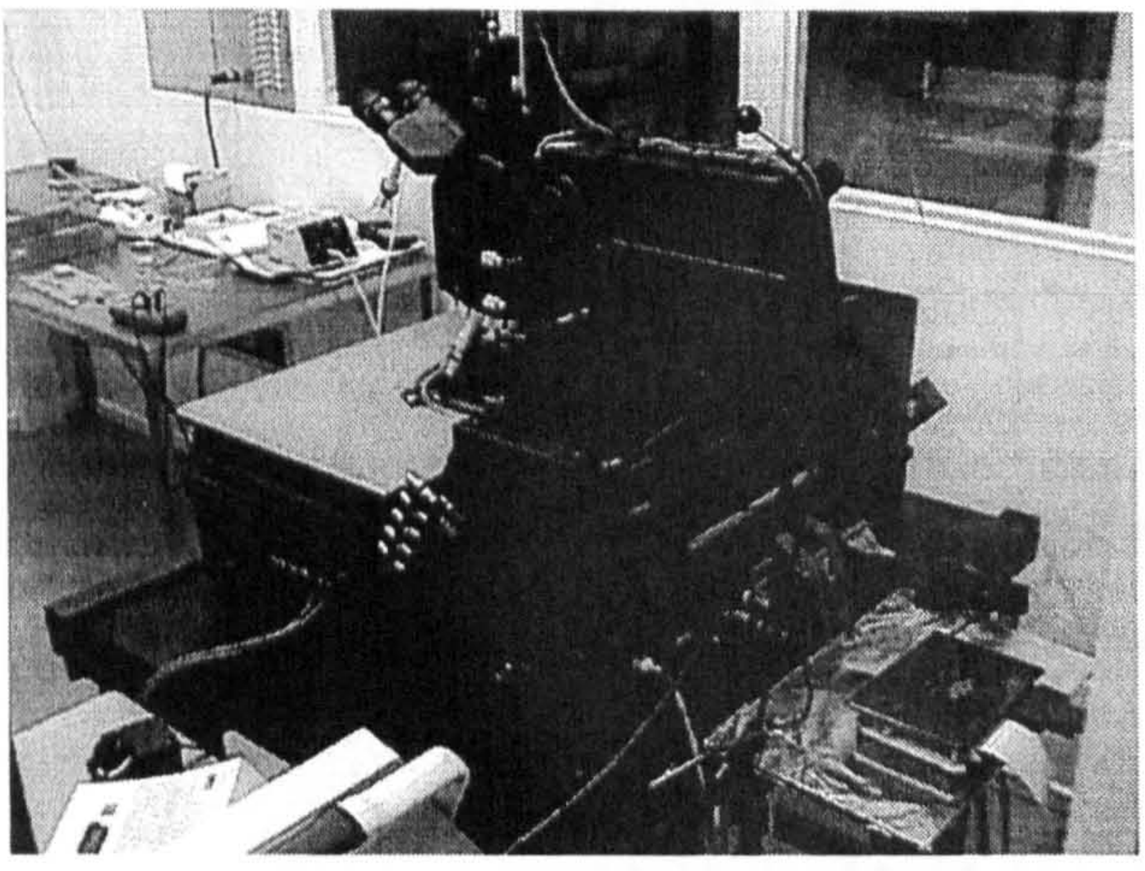

Figure 3.23: Photograph of probe station setup at NIKHEF. The MUROS1 interface can be seen at the bottom right, with the probe card connector attached. All measurements were made under clean room conditions.

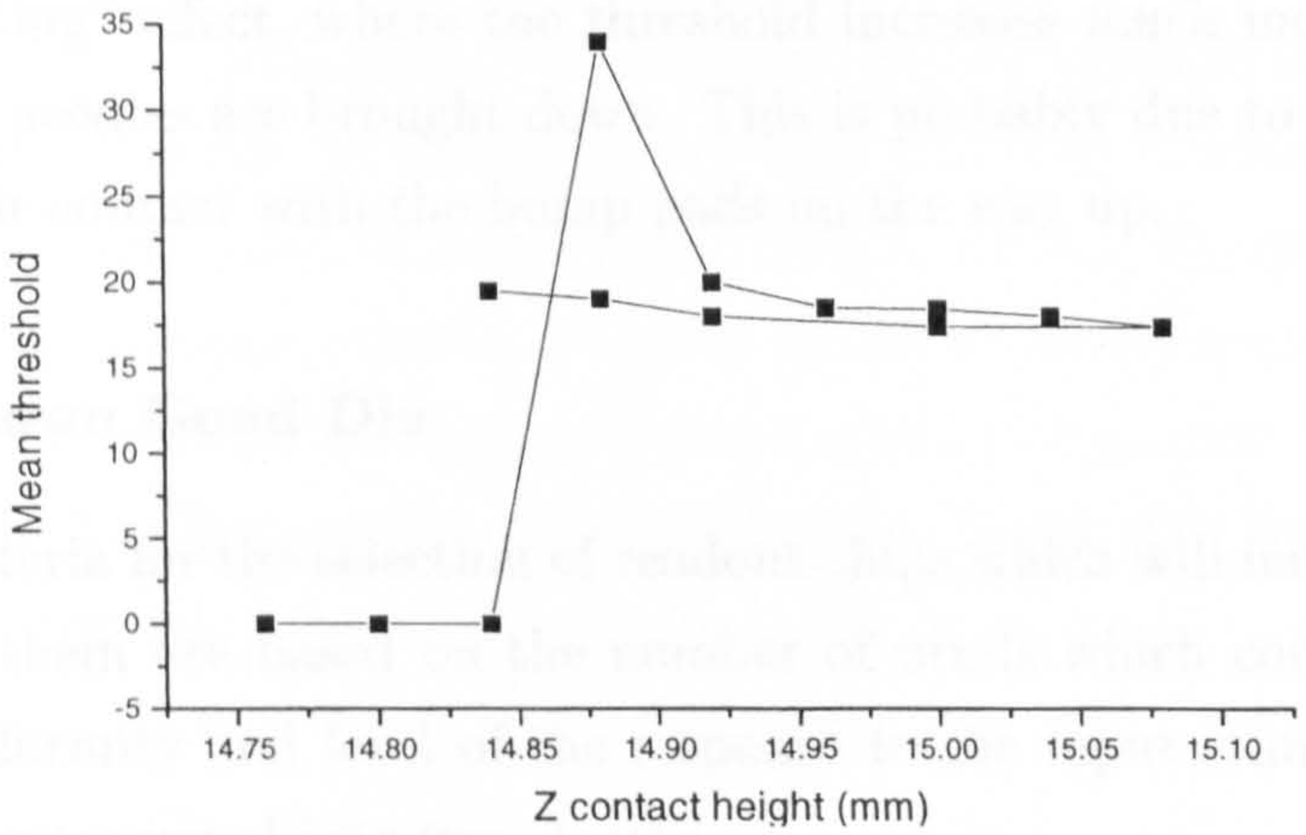

Figure 3.24: Plot of average threshold against probe card contact height. The return line has the measurements made when gradually lifting the pins off the wafer.

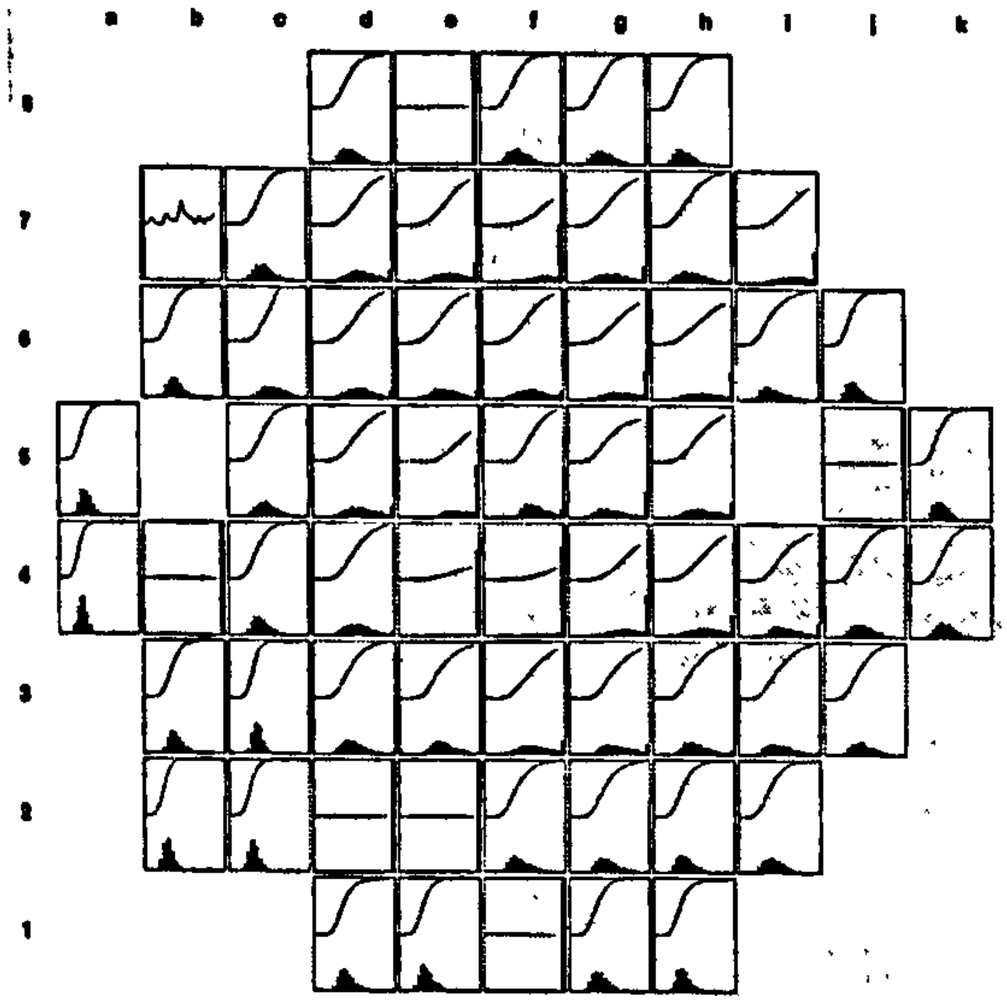

Figure 3.25: Wafer map for wafer 10C3. The lower histogram in each box shows the shape of the threshold distribution. The upper curve is the mean S-curve response of all the pixels

able contact with the bond pads. The return line (the flatter one) shows a "lifting" effect, where the threshold increases much more slowly than when the needles are brought down. This is probably due to the needles retaining their contact with the bump pads on the way up.

Known Good Die

Criteria for the selection of readout chips which will have detectors mounted on them are based on the number of pixels which count properly, and the uniformity and level of the response to the input stimulus. The chips may be categorised into two classes:

- **Class 1:** Chips which have more than 4000 pixels responding at a mean threshold of less than 20mV

- **Class 2:** Chips which do not meet the first class are normally rejected.

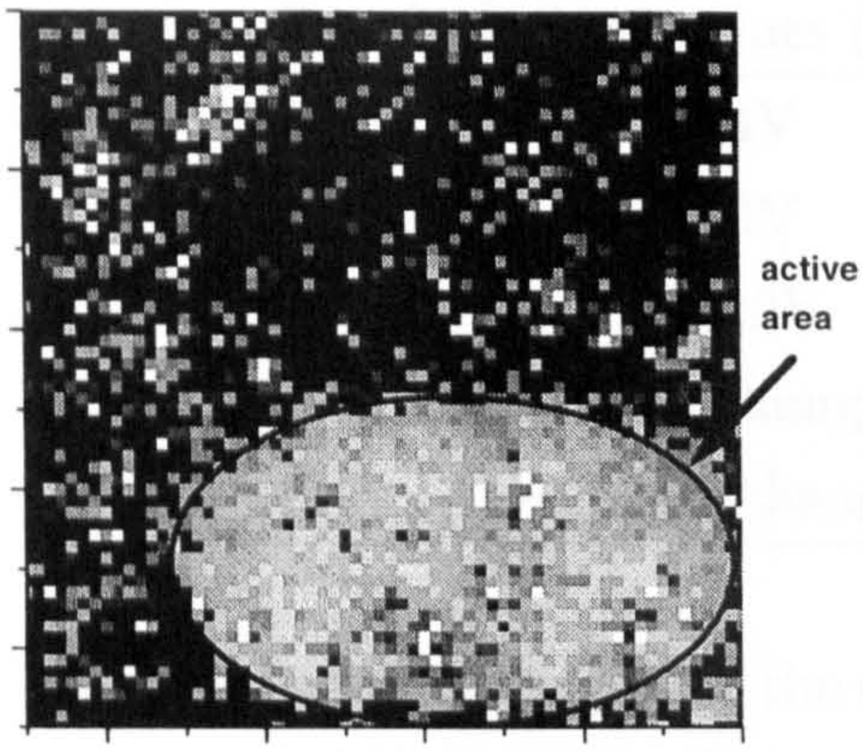

Figure 3.26: Assembly 9825I illuminated by a Tb source. The active area has decreased to approximately 30% of the original sensor area over a period of 7 months.

Figure 3.25 summarises the measurements made on wafer 10C3. Each box contains a histogram and curve. The histogram (at the bottom) shows the shape of the threshold distribution, and the upper curve shows the mean "S-curve" response of all pixels in the matrix. The fact that the best chips are found on the periphery of the wafer has been observed in almost all wafers tested. This wafer has 7 Class 1 chips, with a further 15 chips which are just below the selection criteria. Possible causes of the poor quality of chips near the centre include a variation in bias voltage (V_{bias} and V_{comp}) across the wafer due to differing transistor dimensions, which may be affecting the operating conditions.

3.5.2 Bump-bonding

Some assemblies have been seen to degrade quite badly in image quality with the passage of time. One of the principal effects seen is the gradual loss of sensitivity around the perimeter, leaving only a small part of the sensor operational. Figure 3.26 shows an SI-GaAs assembly flood image,

Supply	New values (V)
V_{dd}	+4V
V_{dda}	+4V
V_{gnd}	+2.2V
V_{ss}	0V (unchanged)
V_{cc}	+5V (unchanged)

Table 3.2: New supply voltages for the damaged GEC chips.

with about 70% of the detector giving no useful information. This effect may be due to differential thermal expansion between the readout chip and detector, causing higher stress at the periphery of the detector and leading to loss of signal from the outer pixels. Since assemblies were in extremely short supply, a destructive test to view the degradation of the detector by cycling the temperature was not performed!

3.5.3 Sputtering damage

Silicon assemblies bump-bonded at GEC during Spring 2000 were found to have been radiation damaged by the sputtering under-bump metallisation process [14]. The effect of this was to reduce the V_{dd} and V_{dda} supplies to the chip, causing a drop in performance. The external supplies for the PCC1 were adjusted upwards to compensate for the damage, and the analog reference voltage V_{gnd} was similarly increased to provide an effective current drain. Table 3.2 shows the new voltages required to operate the PCD. These values apply to all silicon detectors studied in this thesis, results from which are described in Chapters 4 and 5.

A summary of all the devices received in Glasgow and used in this thesis is presented in table 3.3.

Device	Date	Material
R/O chip 8D,8F	10/97	No detector
1804B	5/98	200μm SI-GaAs (Alenia)
9815A-L	7/98	200μm SI-GaAs (Glasgow)
9825H-I	12/98	300μm SI-GaAs
7I-06G0	4/00	250μm SI-GaAs (Freiburg)
P24[5D], P22[6H]	5/00	300μm Si (Freiburg)
GA1,GA2,GA3	5/00	500μm EPI-GaAs (Glasgow)

Table 3.3: Summary of devices at University of Glasgow.

Chapter 4

Synchrotron Source Applications

The monochromatic, high flux photons produced by a synchrotron radiation source are an ideal testing ground for the PCD. The Synchrotron Radiation Source (SRS) at the CLRC Daresbury Laboratory, Cheshire, England provides such a source, with Station 9.1 providing a full experimental setup for powder diffraction studies. The existing technology is based on scintillators, which although efficient are quite slow and provide no 2-D information. The PCD used for the experiments described here was assembly 9825I from CERN, a 200μm thick SI-LEC GaAs detector operated at 340V reverse bias. The MEDIPIX readout chip was loaded with a 3-bit threshold adjust mask, calibrated at the SRS using a pulse generator before any images were taken. The useful working area of the detector had, by this time, reduced to a 40x34 pixel array in the top half of the sensor. Possible sources and consequences of this behaviour are discussed in Chapter 3. The SRS was working in single-bunch mode for the duration of the visit, thus ruling out a study of the rate capabilities of the PCD. The opportunity was therefore taken to extend the work of Manolopoulos et al. [60] which used a GaAs and Si pixel detector with the Ω3/LHC1 in an X-ray powder diffraction (XRD) experiment. The SRS was, in this case, operating in multi-bunch mode, giving higher rate and

statistics.

4.1 X-ray powder diffraction

Over a hundred years ago it was known that crystals consisted of repeating unit cells, establishing highly symmetrical planes and faces within crystalline materials. Later, with the discovery of X-rays, diffraction patterns were observed from these symmetrical crystal structures which allowed detailed measurements of the crystalline structure of these materials to be taken. The investigation of crystal structure should ideally be made on single crystals, however the lack of availablility of single crystal samples necessitates other experimental methods. One of the most common is *X-ray powder diffraction*, which coupled with the high-intensity, monochromatic beams available at synchrotron sources allows detailed study of simple structures.

4.1.1 Synchrotron radiation

Synchrotron radiation is defined as the electromagnetic radiation emitted by a charged particle moving with relativistic velocity through an external electric (or magnetic) field, being observed at a large distance usually in the forward direction of the particle motion.

Synchrotron radiation has a number of unique properties [61]:

- High brilliance: radiation is extremely intense and highly collimated.
- Wide energy spectrum: radiation is emitted with a wide range of energies allowing a beam of any energy to be produced.
- Polarisation: radiation is highly polarised.
- Short pulse length: typically less than a nanosecond.

These properties have been exploited in a vast range of research fields. Using the intense UV, soft and hard X-ray beams synchrotron radiation

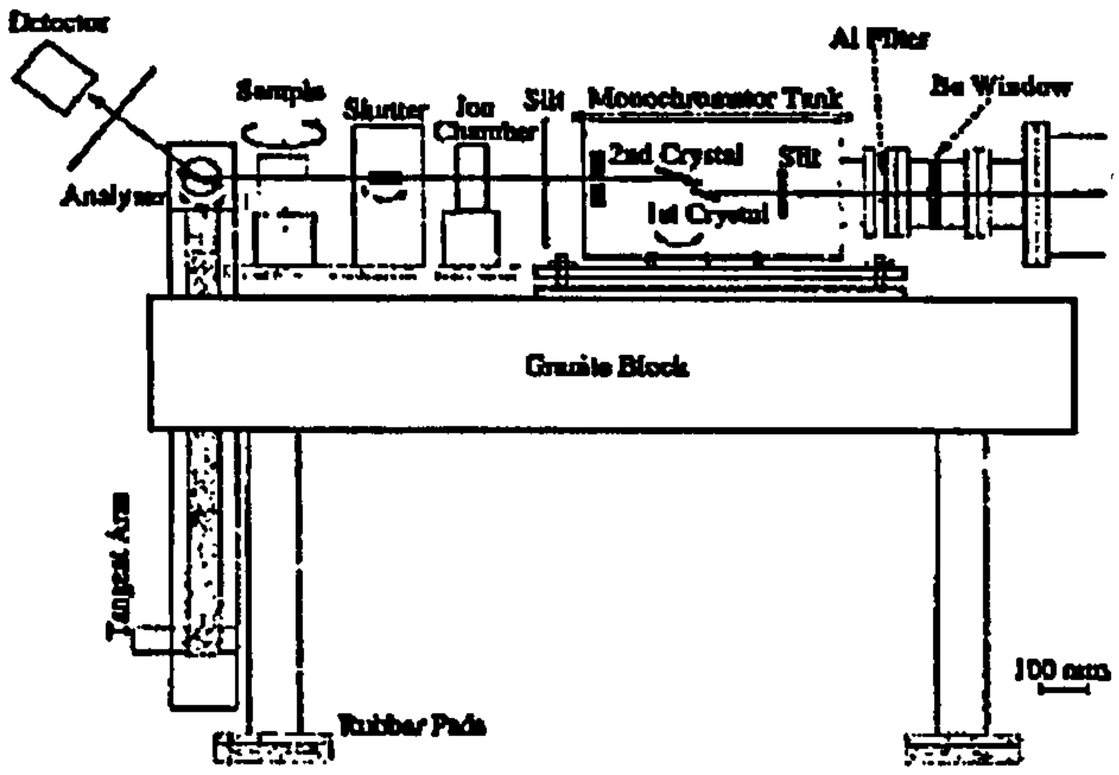

Figure 4.1: Laboratory setup for a diffraction enhanced imaging experiment. [62]

facilities produce, it has been possible to: determine the structure of materials and molecules, the chemical structure of surfaces and interfaces; analyse trace element concentrations in regions of the size of a micron; measure local molecular structures in disordered systems (e.g. solutions and catalysts) and has allowed 3-D CAT scan images to be obtained with micron resolution.

Third generation synchrotron sources (such as the planned UK DIAMOND project) will be capable of delivering a beam which will make time-resolved crystallography and spectroscopy feasible on a nanosecond timescale. The high intensity beams may be used in high pressure diffraction experiments, and X-ray microscopy will benefit from 100 Angstrom resolution in the ability to image wet biological samples, which is finding important applications in biology.

Application

A good example of the application of synchrotron radiation to medical imaging can be found in the relatively new field of *diffraction-enhanced imaging (DEI)* [62].

DEI is a new method of X-ray radiography developed in 1995 at Brookhaven

Laboratory, NY, USA for mammography with improved image contrast. A fan-shaped, synchrotron-generated x-ray beam, monochromatized by a perfect-crystal monochromatoris used to measure the x-ray transmission of a subject in a line-scan detection method. Figure 4.1 shows a typical experimental setup for DEI. The heart of the system is the analyser crystal, similar to the monochromator crystal, which is positioned between the subject and the detector. The detector only receives the part of the subject transmitted beam which has satisfied the crystal's diffraction condition. An image contrast is achieved by measuring the angular yield function (rocking curve) by moving the analyser above and below the diffraction angle. The intensity of the transmitted beam falls off either side of the rocking curve, and hence two measurements made on different points on the curve will provide a high sensitivity image contrast to the two physical processes defining the angular deviation: refraction, which is symmetrical to the left and right of the rocking curve peak; and small-angle scattering, which is symmetrical above and below the plane. None of these processes are resolved in conventional radiography.

A typical detector for this application is a scintillator array ($CdWO_4$) bonded to a photodiode array with around 0.92mm pitch (usually masked by a tantalum grid which improves the spatial resolution by a factor of 2). The angular step required to image across a 360^o rotation of the sample corresponds to approximately 0.23mm across the detector face.

Hybrid pixel detectors would allow a complete 2-D profile of the rocking curve to be acquired in a single acquisition, along with lower noise than the indirectly detecting scintillator/photodiode array. The opportunity to tune the threshold would also allow Compton scattering effects to be excluded. The possibilities for photon counting pixel detectors in a similar experiment is presented in section 4.2.

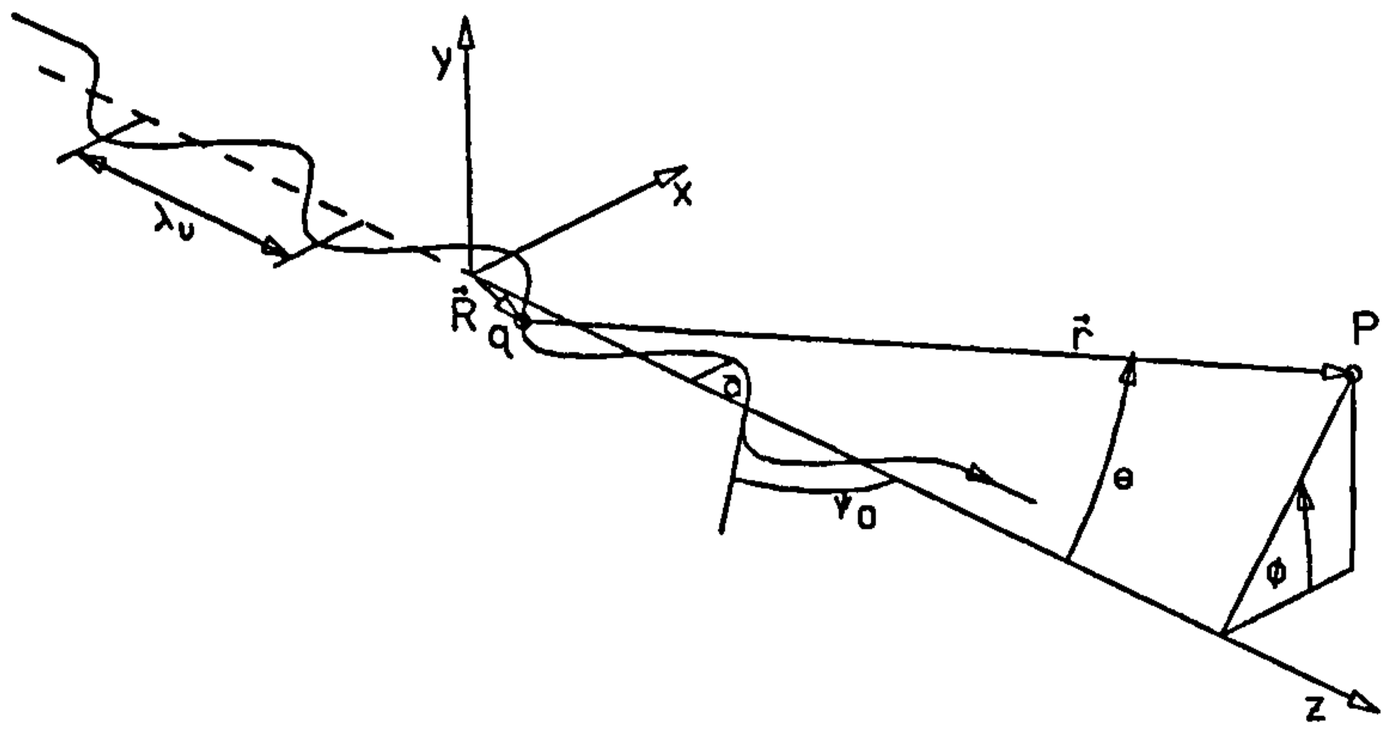

Figure 4.2: Radiation geometry from an undulator

4.1.2 Origin

Consider a charged particle moving with velocity βc on a closed circular orbit of radius ρ. The emitted radiation is expected to have a line spectrum of frequencies:

$$\omega_n = n\omega_0 \ , \omega_0 = \frac{\beta c}{\rho} \tag{4.1}$$

where ω_0 is the *revolution frequency* . In practice, quantum noise broadens these lines to the extent that a continuous spectrum emerges. However, use of an undulator allows quasi-monochromatic synchrotron radiation to be produced from relativistic particles.

4.1.3 Undulator radiation

An undulator or "wiggler" is a spatially periodic magnetic structure which creates a field of the form:

$$B(z) = B_y = B_0 \cos\left(\frac{2\pi}{\lambda_u} z\right) \tag{4.2}$$

where λ_u is the period length. Figure 4.2[63] shows the geometry of the radiation from the undulator. Provided the field is not too strong, the particle trajectory through the wiggler is (to a good approximation):

$$x = a\cos(k_u z)\ ,\ a = \frac{eB_0}{m_0 c\gamma k_u^2}\ ,\ k_u = \frac{2\pi}{\lambda_u} \tag{4.3}$$

$$\text{where, } \frac{dx}{dz} = -\psi_0 \sin(k_u z)\ ,\ \psi_0 = \frac{eB_0}{m_0 c\gamma k_u} = \frac{K}{\gamma} \tag{4.4}$$

$$\text{and } \gamma = \frac{E}{m_o c^2}\ ,\ K = \frac{eB_0}{m_0 c\gamma k_u} = \gamma\psi_0 \tag{4.5}$$

The behaviour of the radiation produced is strongly dependent on the maximum deflection angle ψ_0 compared to the natural opening angle of the synchrotron radiation $\frac{1}{\gamma}$. The quantity K (equation 4.5) quantises this dependence. If $K \geq 1$, the trajectory 'wiggles' by more than the natural opening angle, leading to a complicated radiation pattern. For $K \ll 1$ the angular range is much smaller than $\frac{1}{\gamma}$, producing radiation of a relatively simple nature which may be made monochromatic through collimation.

4.1.4 Daresbury Station 9.1

The Synchrotron Radiation Source consists of a commercially available linac producing an electron beam of between 10 and 15 MeV, which is injected into a 600 MeV booster synchrotron. This accelerated beam is in turn injected into the storage ring operating at 2 GeV. The RF power for the storage ring is provided by a 250 kW klystron supply and the ring has a bending radius at the curves of 5.56m, and a mean orbit radius of 15.28m. The facility produces at its exit ports a beam strongly peaked in the forward direction, highly polarized in the plane of the electron orbit, and with a well-defined continuous spectrum reaching from the infra-red to X-rays. Station 9.1 [65] houses the powder diffraction facility, allowing operation in Debye-Scherrer (or flat-plate sample) geometry at X-ray wavelengths between 0.4 and 1.5 Angstroms (31keV down to 8keV). At 15m from the 5T wiggler magnet, a water-cooled Si (111) monochromator crystal may be set to an angle with a precision of 0.001^0. The station receives approximately 2.87mR/s (25μSv) at the Si collimator, and 0.69mR/s (6μSv) is delivered onto the sample. The maximum flux occurs above 25keV during multi-bunch operation, where a

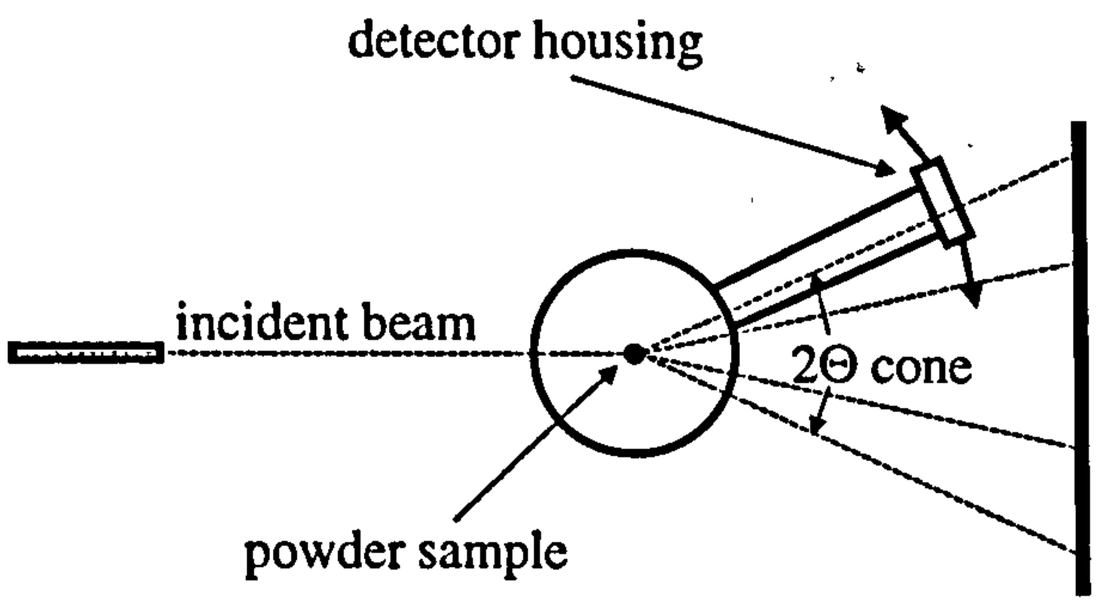

Figure 4.3: Experimental setup for the X-ray powder diffraction experiment

number of closely spaced (of the order of picoseconds) electrons are injected into the booster synchrotron.

4.1.5 Debye-Scherrer method

A spinning capillary tube full of a powdered sample ($KNbO_3$) was illuminated with the monochromatic X-ray beam. The beam is scattered by the crystal planes within the sample according to the Bragg formula [64]:

$$n \times \lambda = 2 \times d \times sin\theta \tag{4.6}$$

Because of the random orientation of the crystals in the sample, the diffraction maxima lie on a cone making an angle of 2θ to the incident beam direction, which is an axis of symmetry. With a detector placed normal to the beam direction, these maxima may be viewed as a series of concentric rings in space. Figure 4.3 shows the basic experimental setup. Standard detection techniques in such experiments involve scintillators, in this case a 20mm diameter disk of scintillating material, collimated with a 300μm slit, connected to a standard photomultiplier, amplifier, comparator and scaler readout chain. The PCD was mounted in the same position at the end of

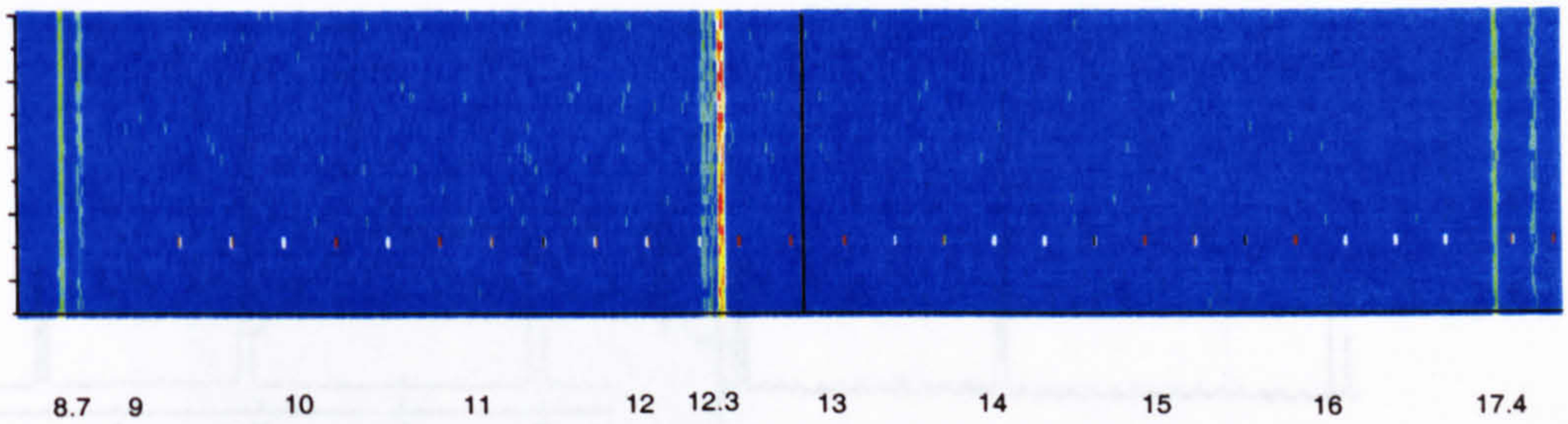

Figure 4.4: PCD scan across 2Θ of a section of the XRD pattern from 8^o to 18^0

the detector mounting arm.

4.2 Large Area Pattern Scanning

The disadvantage with the scintillator set up is the need for movement in at least one direction in order to visualise any variation in the intensity pattern. The 2-D positional information provided by the PCD allows adjacent XRD pattern maxima to be resolved in a single acquisition. However, the extra information acquired by a single image can be used to cut down the number of steps needed to obtain a large area "tiled" image. Figure 4.4 shows a layered image of a PCD scan across the diffraction pattern at 20 keV photon energy. The angles along the x axis represent vertical movement in 2θ, with a source to detector distance of 700mm. Note that the white spots in the bottom third of the image, which are repeated for every image layer, are noisy pixels which have escaped the threshold masking process. The scintillator image profile in Figure 4.5(a) required steps of 0.01^o along 2θ. The PCD scan shown in Figure 4.5(b) (the profile of Figure 4.4) required steps of 0.3^o to achieve the same resolution. The acquisition time per step for the PCD was 30 seconds

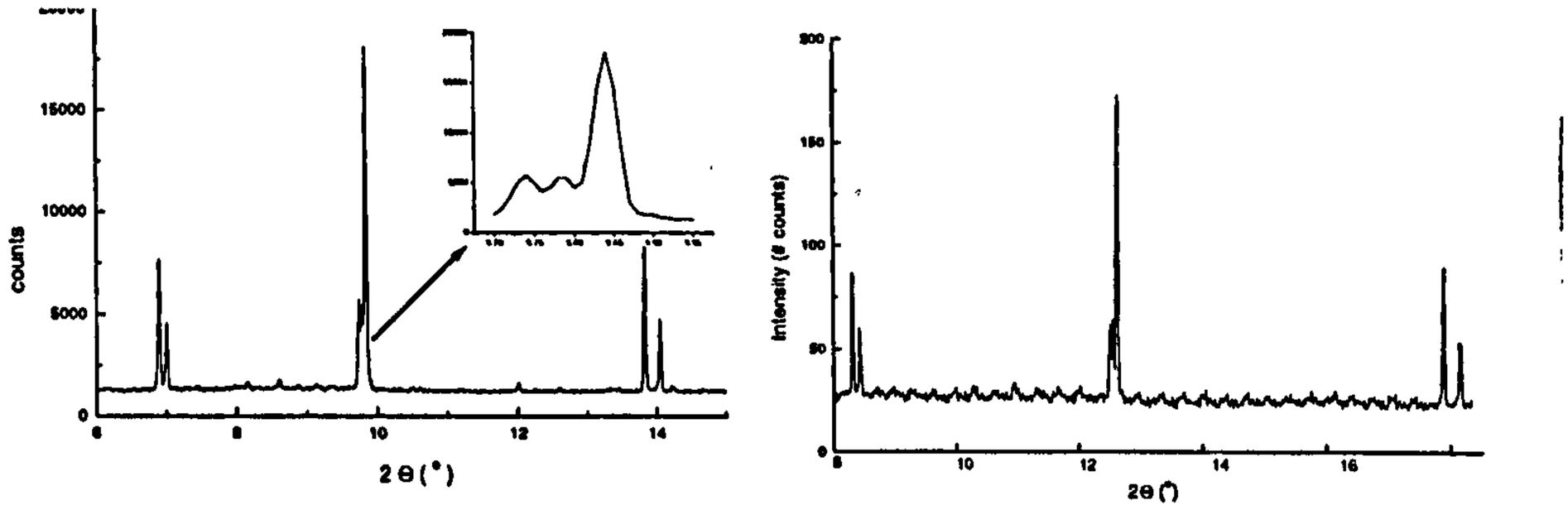

(a) Scintillator at 25keV - multi bunch SRS [60]

(b) PCD at 20keV - single bunch SRS

Figure 4.5: XRD pattern of $KNbO_3$ powder across 9 degrees (12cm in space)

compared to approximately 5 seconds for each step of the scintillator. Taking acquisition time and step size into account, the PCD offers improvement in diffraction pattern profiling speed by a factor of 5. A further 50% reduction would be achievable were the whole sensor operational, allowing an order of magnitude improvement on the existing technology. The large reduction in statistics (visible as a noisier data floor) is due to the single-bunch operation during the PCD experiments compared to the multi-bunch data acquired previously [60]. This may lead to further improvement in the total scanning time. The scintillator acquisition time was fixed for the Station 9.1 setup, so the PCD shutter time of 30 seconds was chosen to give a similar number of counts were the SRS operating in multi-bunch mode.

4.3 Peak Resolution

The triple peak highlighted in Figure 4.5(a) was the best candidate to test the resolution of the detector. The triple peak was tracked through 3 changes of incident beam energy, all at the same comparator threshold for an acquisition time of 10 minutes. Decreasing the incident beam energy causes a spreading

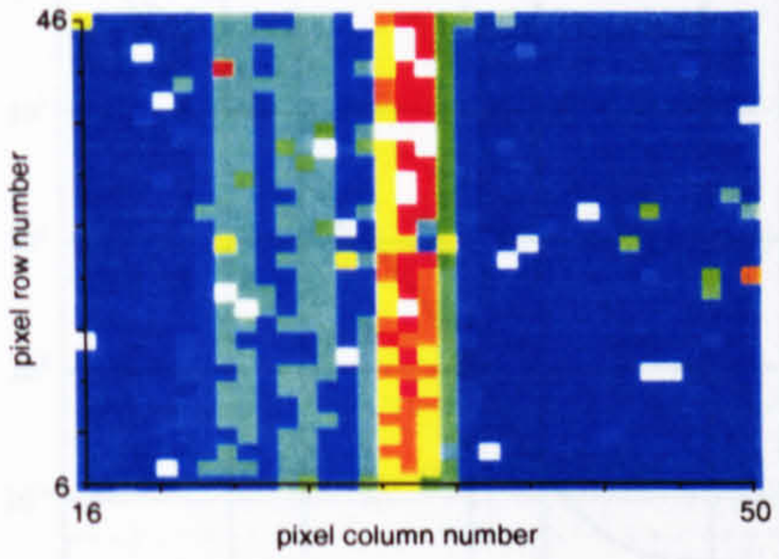

(a) 25keV image

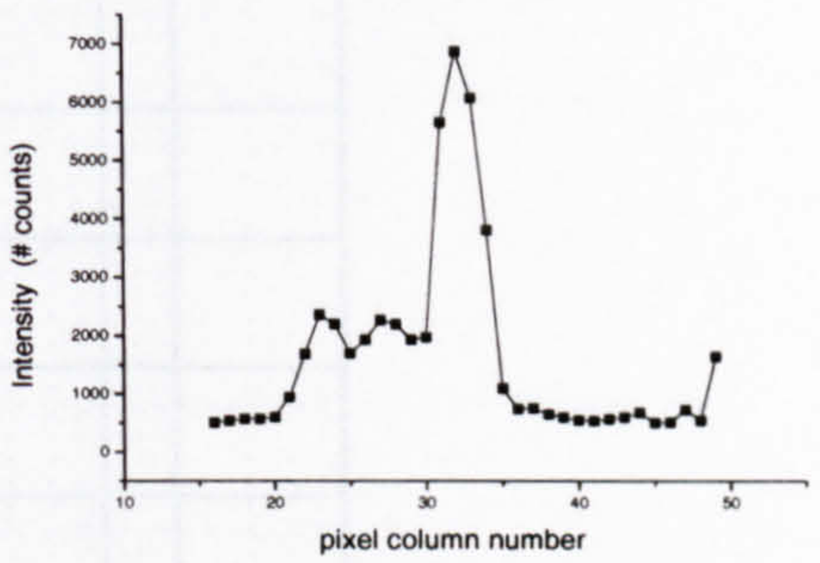

(b) 25keV profile

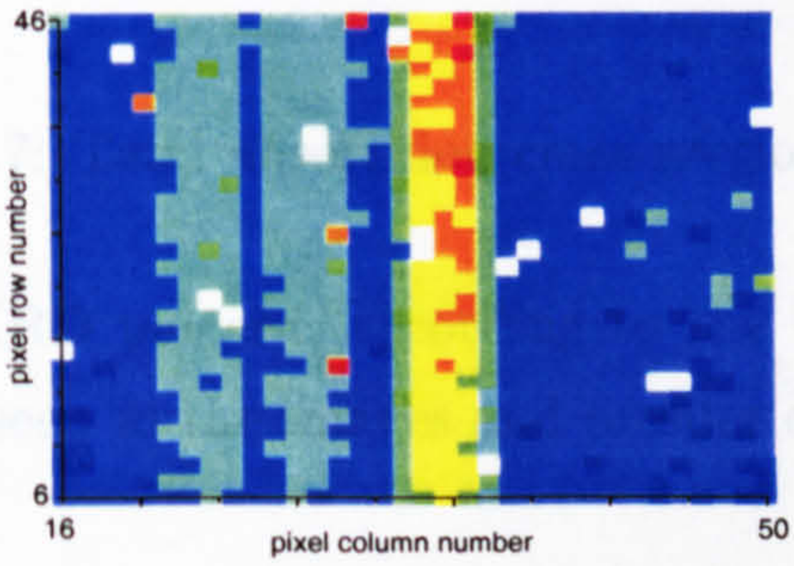

(c) 20keV image

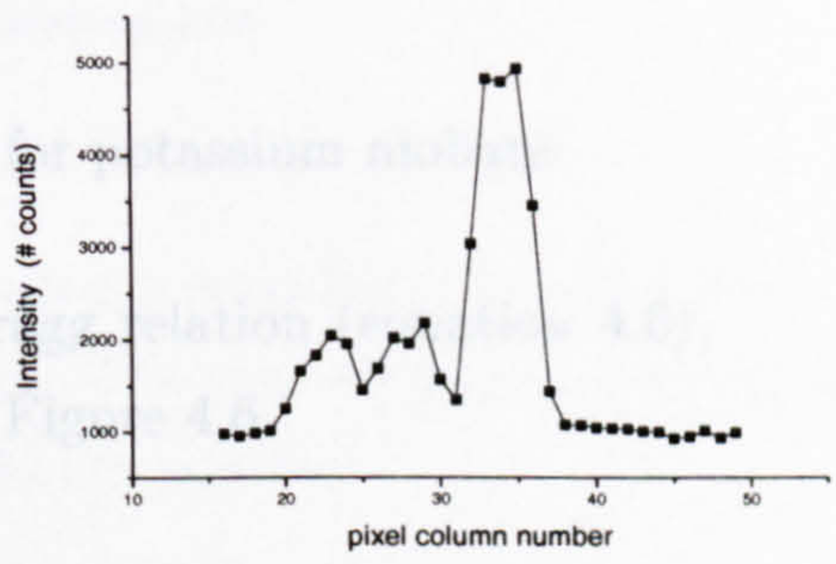

(d) 20keV profile

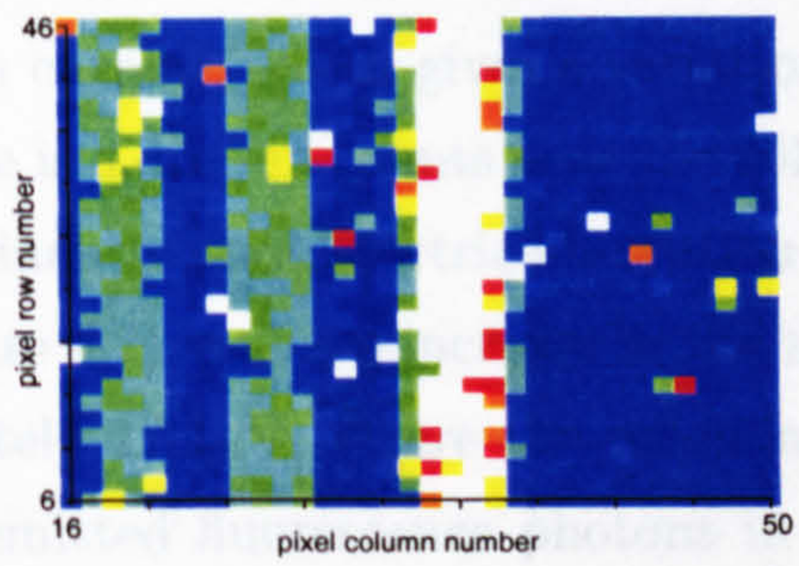

(e) 14keV image

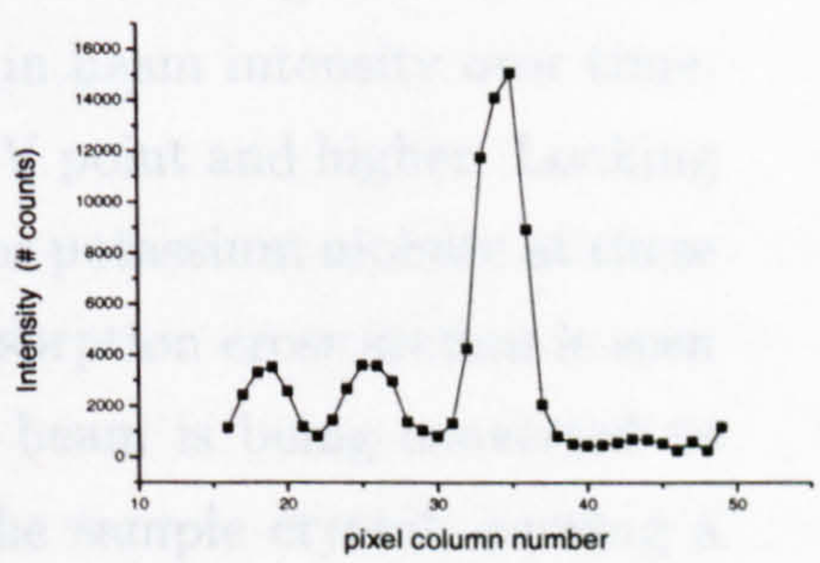

(f) 14keV profile

Figure 4.6: Triple peak in the XRD pattern of $KNbO_3$ powder at 25, 20 and 14 keV.

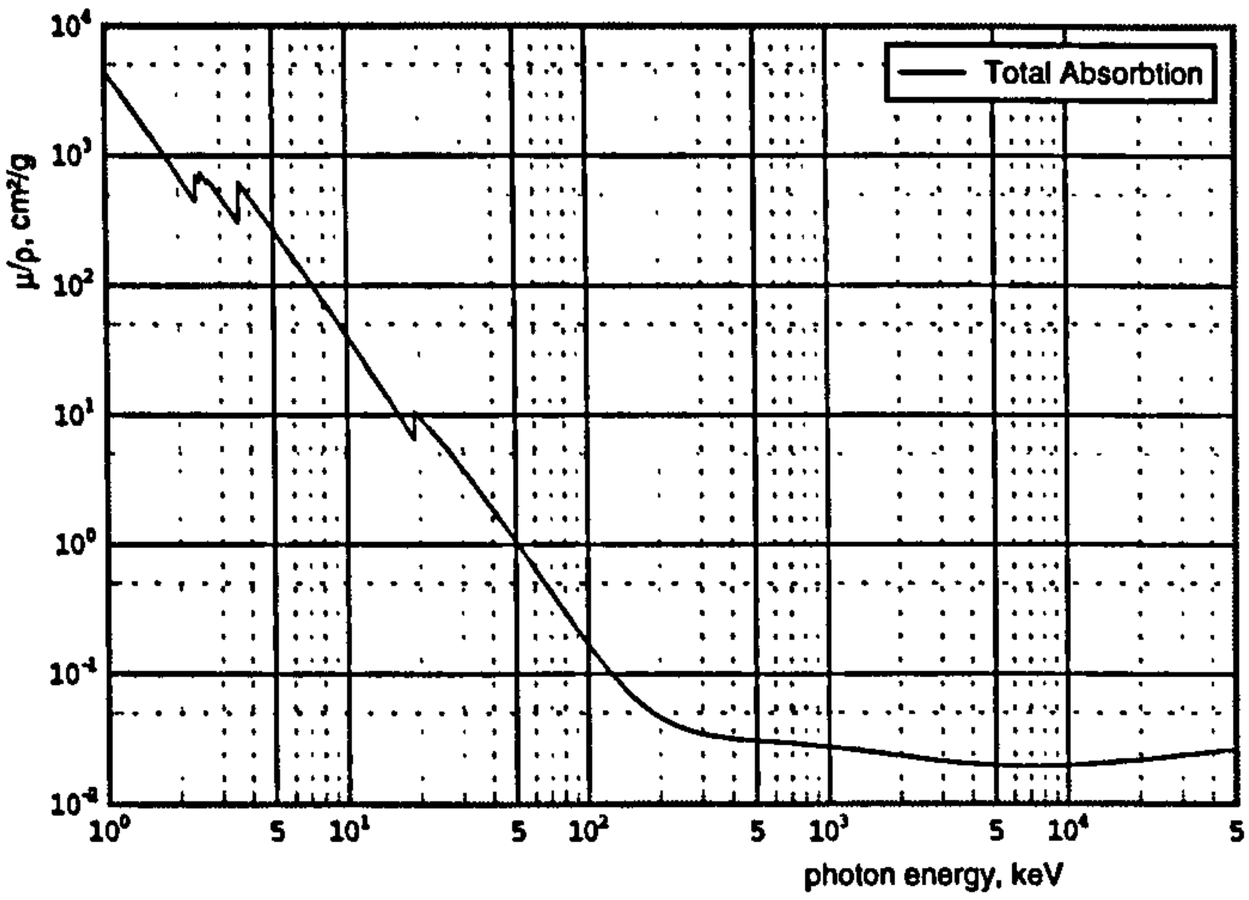

Figure 4.7: Total absorbtion cross section for potassium niobate.

in 2θ of the XRD pattern, according to the Bragg relation (equation 4.6), which can be seen in the images and profiles of Figure 4.6.

4.3.1 Loss of statistics

The fluctuations in statistics visible across the three energies is correlated with the beam current, which gives a variation in beam intensity over time. However, there is a drop in counts near the 20keV point and higher. Looking at the predominantly photoelectric absorption for potassium niobate at these energies (Figure 4.7), a sharp increase in the absorption cross section is seen at approximately 17 keV, where the incoming beam is being converted to isotropically emitted fluorescence photons in the sample crystal, causing a drop in the number of photons incident on the detector. This effect is small compared to the change in beam current over time, but accounts for the 20keV flux reduction as we are very near the K-edge absorption energy for ^{41}Nb (18.99 keV) [67]. The fluorescence photons have energies of 16.52 and 16.62 keV, so adjusting the threshold of the PCD to about 17keV should yield a decrease in background statistics. [Note that the setting of energy

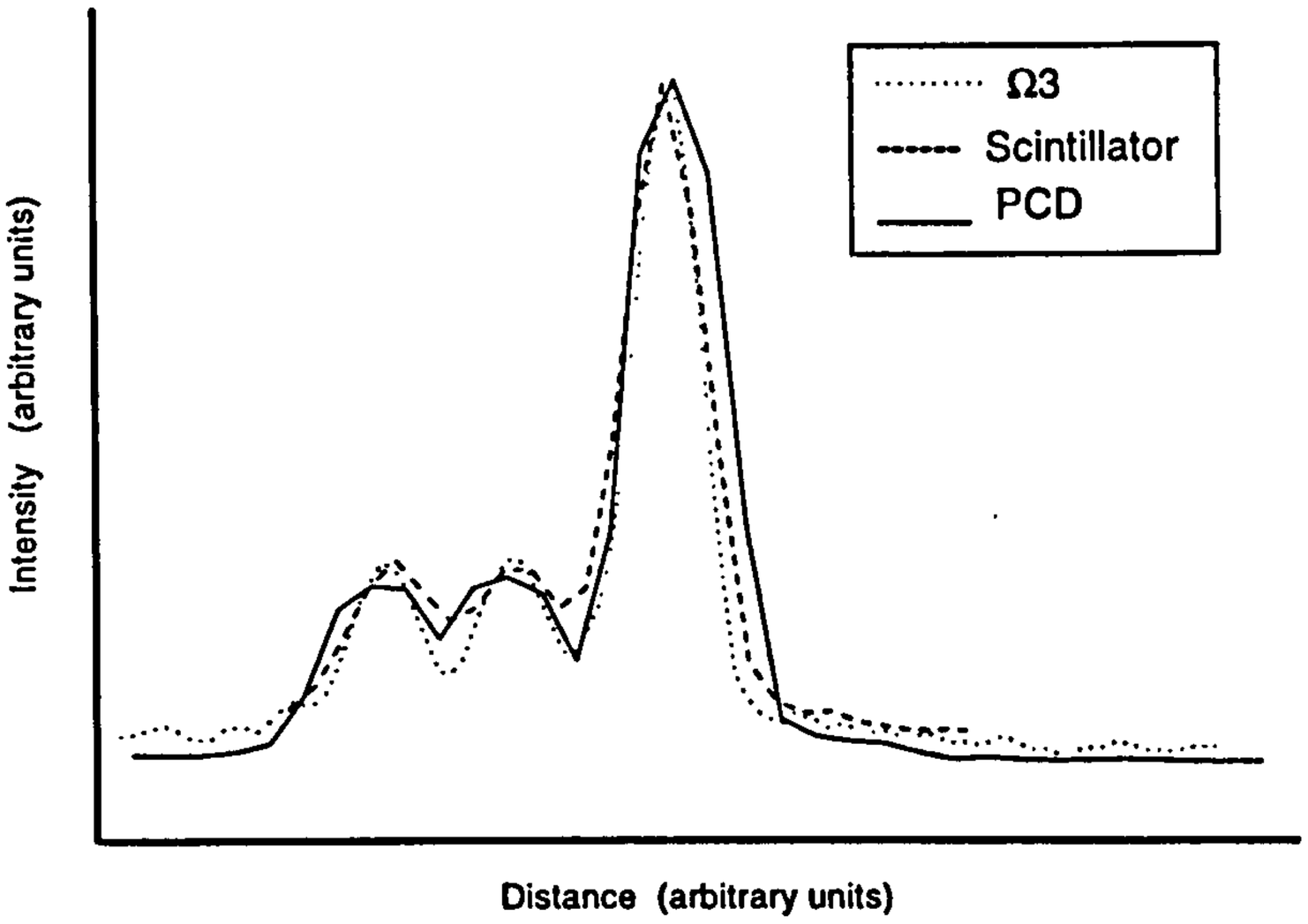

Figure 4.8: 25 keV triple peak profile using a scintillator (dashed line), the Ω3 (dotted line) and the PCD (solid line). The axes are normalised intensity and normalised distance, hence the units are relative.

thresholds is not possible with charge integrating systems].

4.4 Detector comparisons

Results obtained with a beam energy of 25keV may be compared to the previous results made with the Ω3 [60], and the scintillator (Figure 4.8). The peaks may be compared by calculating the peak-to-valley ratio (Table 4.4). It can be seen that the Ω3 is the best performer due to its high spatial resolution along one axis (50μm), but the PCD still offers an improvement over the standard scintillator technology. The Peak-to-valley ratio is the ratio of the full height of the peak in counts measured to the height of the bottom of the adjacent data 'valley'. The primary peak is the large one and the secondary the centre, smaller peak.

Results of a threshold scan to determine the energy/comparator threshold

	Peak-To-Valley Ratio	
	Primary	Secondary
Scint.	3.6:1	1.2:1
PCD	4.1:1	1.4:1
Ω3	6.1:1	2.1:1

Table 4.1: Peak-to-valley ratio comparisons for the 3 systems used at Daresbury SRS.

relation proved difficult due to the decreasing flux from the source with time. This made it difficult to determine the end-point of the integrated pulse height spectrum.

4.5 Remarks

The photon counting detector is attractive for synchrotron radiation applications due to:

- 2-D pattern recognition in a single acquisition.
- Fast readout time - useful for time-resolved studies.
- Direct X-ray detection (no conversion layers needed)
- Photon counting gives large, linear dynamic range - needed for high flux applications.
- High efficiency material may be used.

The PCD has been shown to outperform the scintillator technology used at station 9.1 by up to an order of magnitude in terms of speed of image acquisition [66]. The single scintillator step size and the pixel pitch were comparable, so the resolutions of the two systems are similar. Future developments with the PCD in the MEDIPIX collaboration will bring the pixel

pitch down to approximately 50 microns, hence the spatial resolution will be comparable with the short dimension of the Ω3, making the new generation of chips a very attractive prospect.

Chapter 5

Photon counting vs charge integration

CCD technology has been the preferred basis for imaging in industry for the past decade. However, as mentioned previously, CCDs have certain limitations which mean they cannot function effectively as imaging devices under specific conditions. CMOS technology is expected to supersede current technology [68] by addressing these limitations. The problems associated with CCDs are essentially generic problems of *integrating* devices, namely:

- **Non-linear dynamic range:** the response of integrating devices is only linear provided one is not at the extremes of low and high exposure. At these extremes it becomes more difficult to resolve object features. The non-linearity means reduction of patient dose is impossible without sacrificing image quality.

- **Blooming:** the sharing of charge between pixels when the incident beam saturates the sensor causes large white spots in the image which have no useful information.

- **Fog:** the leakage current from the active region is shared among all pixels giving a background region behind which one cannot resolve object details.

Photon counting systems are not susceptible to these phenomena because the information stored in each pixel is independent of its neighbours (assuming negligible charge sharing in the active region). This gives a completely linear dynamic range, allowing the same contrast to be achieved across the whole exposure range.

A discussion on the theoretical background behind the improved contrast and signal-to-noise ratio with photon counting systems is presented here, followed by an experimental comparison of two imaging systems: the PCD and the Sens-a-Ray dental imaging device. These systems operate in photon counting and charge integrating modes, respectively, and the operation of both systems under identical conditions provides a preliminary comparison of the imaging capabilities of two fundamentally different detection methods.

5.1 Introduction

Any advantage one system has over the other will be manifest as an improvement in contrast and signal-to-noise ratio. Using a model of an ideal integrating and photon counting system one can demonstrate the theoretically improved performance of the photon counting mode for semiconductor detectors. Previously published results of such simulations have favoured the photon counting detection method [70].

5.1.1 Optimisation of signal-to-noise ratio

In an "ideal" imaging system the lowest possible radiation dose is limited only by the photonic or quantum noise of the source. The signal-to-noise ratio may be expressed as follows [6]:

$$(SNR)^2 = E(N) \cdot I_x \cdot A_q \tag{5.1}$$

where E(N) is the expectation value of the Poisson photon distribution with mean N, A_q is the fraction of incident photons detected, and I_x is a

statistical factor which describes the spread in the single event distribution normalised to events with energy greater than zero. I_x refers to the fluctuations in energy imparted to the detector. With monoenergetic incident photons and a totally absorbing detector, $A_q = I_x = 1$.

Assuming the detector is totally absorbing (all incident photons detected) and neglecting scattering effects, A_q will be unity and the signal-to-noise ratio will depend only on the detector mode of operation [71]:

- **Counting Mode:** Each event is treated the same, so I_x will not be dependent on the single event distribution. This gives a value of unity for I_x.

- **Integrating Mode:** An integrating detector will retain the energy information of the incident spectrum. This means I_x will be dependent on the single event distribution function, yielding an I_x less than unity for polyenergetic incident photons (broad spectrum). I_x is unity ONLY for monoenergetic X-rays.

It can be concluded that to optimise the signal-to-noise ratio in an ideal detector, one must operate in single photon counting mode.

5.1.2 Optimisation of contrast

For an absorbed X-ray fluence, $I(E_i)$, and assuming a finite number of X-rays contribute to the image, the *maximum* noise-free signal we get from a charge integrating system is:

$$S_{int} = \sum_{i=1}^{n} I(E_i) \cdot E_i c \tag{5.2}$$

where $E_i c$ (with c a constant) is the signal charge collected from an X-ray of energy E_i, assuming a linear dependence of the signal on incident photon energy. The maximum signal from a noise-free photon counting system may be given more simply as:

$$S_{pct} = \sum_{i=1}^{n} I(E_i) \tag{5.3}$$

by simply adding up the numbers of absorbed photons. By introducing a function f(E), where $0 \leq f(E) \leq 1$, describes the attenuation by an absorber, one may reduce the value of $I(E_i)$ according to the absorption properties of the object in front of the sensor. An expression to compare the shades of grey in the images from the two systems may be constructed from equations 5.2 and 5.3:

$$\frac{\sum_{i=1}^{n} I(E_i) \cdot E_i c \cdot f(E_i)}{\sum_{i=1}^{n} I(E_i) \cdot E_i c} = R_n \frac{\sum_{i=1}^{n} I(E_i) \cdot f(E_i)}{\sum_{i=1}^{n} I(E_i)} \tag{5.4}$$

Here the factor R_n is a figure of merit which allows the two systems to be compared. We may describe the maximum signal (in terms of maximum transmitted X-ray intensity) as giving a white image, and the minimum signal produces a black image, therefore most images will be a shade of grey. If R_n is greater than 1 then the photon counting system gives a lighter shade of grey, whereas if R_n is less than 1 then the integrating system gives the lighter signal. If we simplify the above expression in terms of total signal in the detector with (S') or without (S) an absorber for both detection modes, we may define the figure R_n in terms of the contrast seen in a uniformly absorbing object image, hence:

$$\frac{S'_{int}}{S_{int}} = R_n \frac{S'_{pct}}{S_{pct}} \tag{5.5}$$

We may define the contrast ratio, C, as:

$$C = \frac{S - S'}{S} = \frac{S}{S} - \frac{S'}{S} = 1 - \frac{S'}{S} \tag{5.6}$$

Substituting equation 5.6 into equation 5.5 one obtains:

$$(1 - C_{int}) = R_n(1 - C_{pct}) \tag{5.7}$$

It can be seen therefore, that given R_n is greater than 1, then the *contrast* obtained with a photon counting system will be greater than that of an

integrating system, with the opposite being true for R_n less than unity. Two cases will be considered for the above expressions; a monochromatic source and one containing a spectrum of X-ray energies.

Monochromatic source

With a source emitting only one X-ray energy, the upper summation limit n is equal to one (only one energy) in equation 5.4, which becomes:

$$\frac{I(E_1)\cdot E_1 c\cdot f(E_1)}{I(E_1)\cdot E_1 c} = R_1 \cdot \frac{I(E_1)\cdot f(E_1)}{I(E_1)} \tag{5.8}$$

After cancelling, it is clear that R_1=1 so there is no difference in the shade of grey between the two systems.

General case

Performing the sum over all n energies (E_i) emitted by the source and by rearranging the terms of equation 5.4 we obtain:

$$\sum_{j=1}^{n} I(E_j)\cdot \sum_{i=1}^{n} I(E_i)\cdot E_i \cdot f(E_i) = R_n \cdot \sum_{j=1}^{n} I(E_j)\cdot f(E_j)\cdot \sum_{i=1}^{n} I(E_i)\cdot E_i \tag{5.9}$$

The j term arises from the fact we are summing the responses of two independent systems, so either side of this expression has n^2 terms. Comparing the terms with the same indices ($(..)_{ij}$+$(..)_{ji}$), equation 5.9 yields:

$$\begin{aligned} &I(E_j)I(E_i)E_i f(E_i) + I(E_i)I(E_j)E_j f(E_j) \\ &= R_{n(ij)}\cdot [I(E_j)f(E_j)I(E_i)E_i + I(E_i)f(E_i)I(E_j)E_j] \end{aligned} \tag{5.10}$$

which cancels to:

$$R_{n(ij)} = \frac{E_i f(E_i) + E_j f(E_j)}{E_i f(E_j) + E_j f(E_i)} \tag{5.11}$$

For the trivial term i=j, $R_{n(ii)}$=1 (i.e. same shade of grey). If E_i is greater (less) than E_j, then f(E_i) is greater (less) than f(E_j), in general (for energies

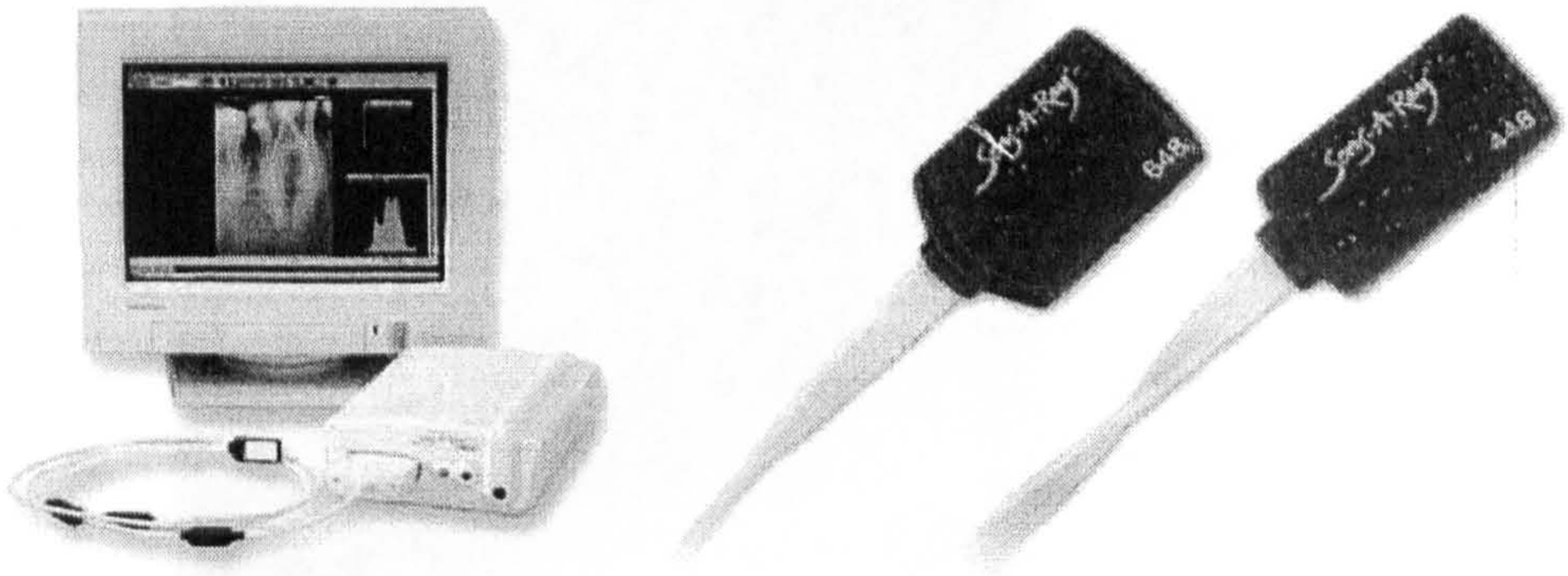

(a) Picture of the Sens-a-Ray imaging system

(b) Image of the two available sensor types (448 used here)

Figure 5.1: The Sens-a-Ray imaging system. The system used here has a coating of scintillating material.

either side of the absorption edge this may not be true). This fact gives the result that for i≠j, R_n is always greater than 1. Hence the photon counting system will always give a whiter shade of grey than the charge integrating system [72]. Using equation 5.7, it can be seen that the photon counting system will give better *contrast* than the charge integrating system.

5.2 The Sens-a-ray dental imaging system

The integrating system under study is the Sens-a-Ray digital intraoral X-ray imaging system [69], the components of which are shown in figure 5.1. The detector is a silicon CCD patterned in a 576×385 matrix of square pixels of side 45μm. The total active region is 17.3×25.9 mm^2. The CCD is coated in a thin scintillating material and the detector is then encapsulated in a package of alumina ceramic. The detector is connected to an A/D converter and digital I/O board which allows readout in approximately 60ms. The sensor is small enough to fit in the mouth for intraoral radiographs (figure 5.1(b)). The device is triggered by the detection of high X-ray flux by special silicon

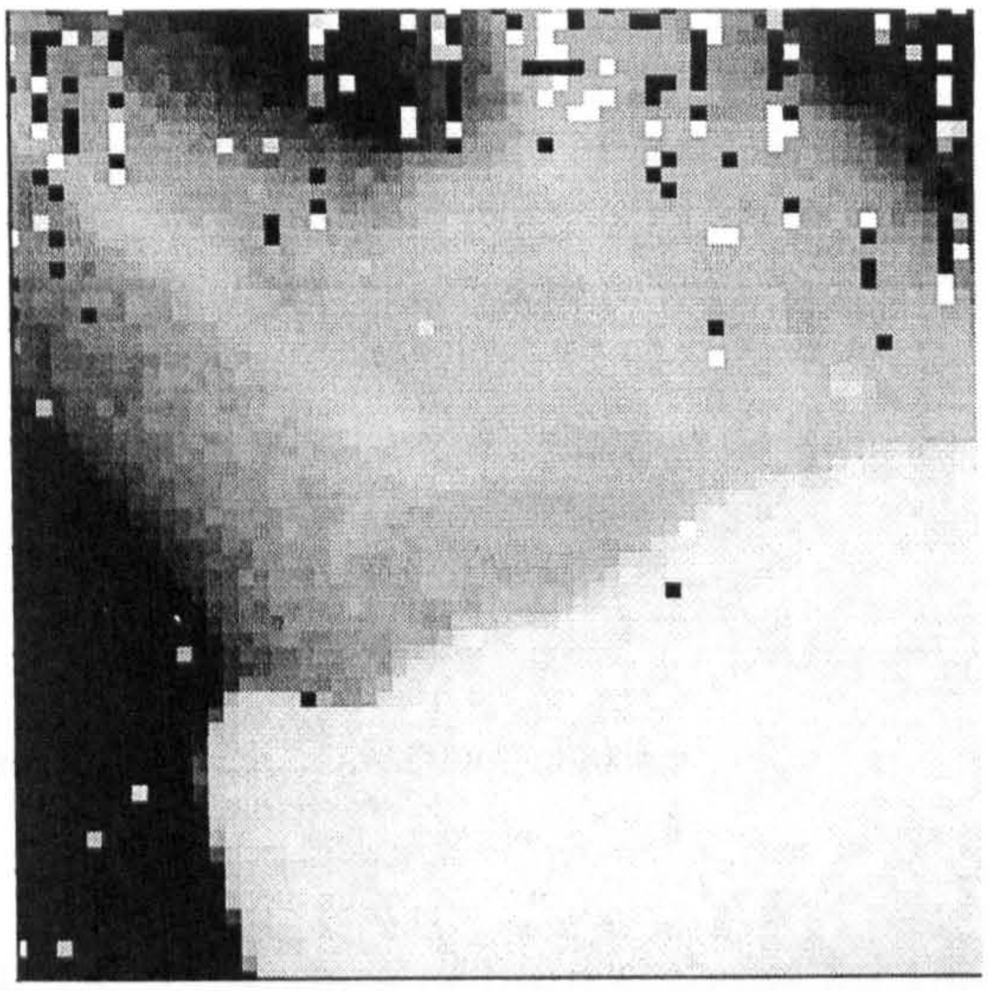

Figure 5.2: Image of the mid section of the tooth phantom. The root is clearly visible and the light area is a gold cap.

diodes on the surface, making a low rate radioactive source measurement impossible. To this end, the Planmeca X-ray gun [47] was used for both systems. Dose information is given in mGy, where a typical dental X-ray requires a dose of around 1 mGy for an adult.

5.3 Contrast across dynamic range

In an ideal noise-free system it has been shown that the contrast achieved in a photon counting system should always exceed that from an integrating device. Using the definition of contrast ratio given in equation 2.17, the contrast for a tooth phantom was measured across the useful dynamic range of the sensor. Figure 5.2 shows a PCD image of the central region of the tooth phantom, with the root visible on the upper left (the all-white section is a gold cap). Figure 5.3 shows the sensitometric responses of the background and target regions for the Sens-a-Ray and the photon counting detector, where the target region is the root of the tooth phantom and the background

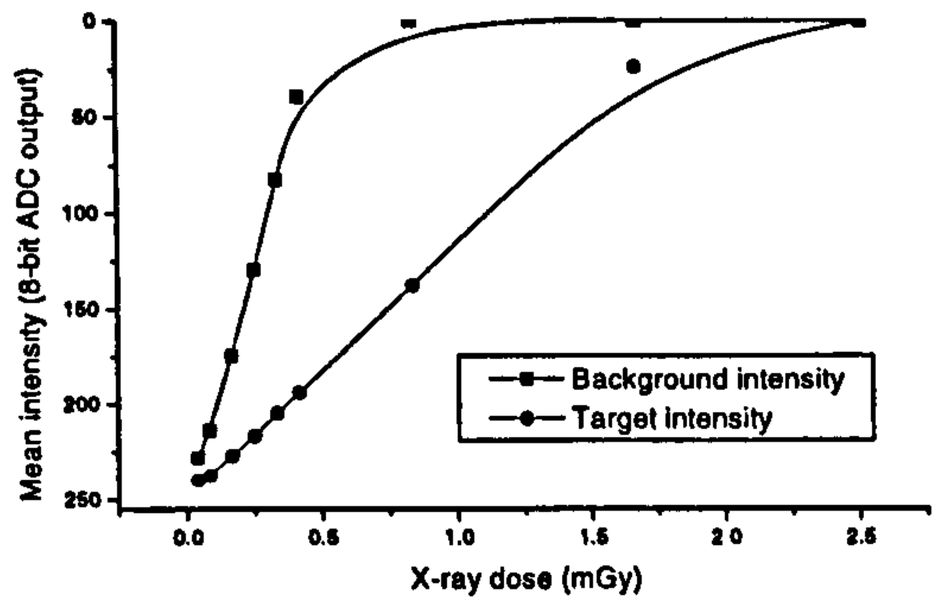

(a) Sens-a-ray with scintillator coating

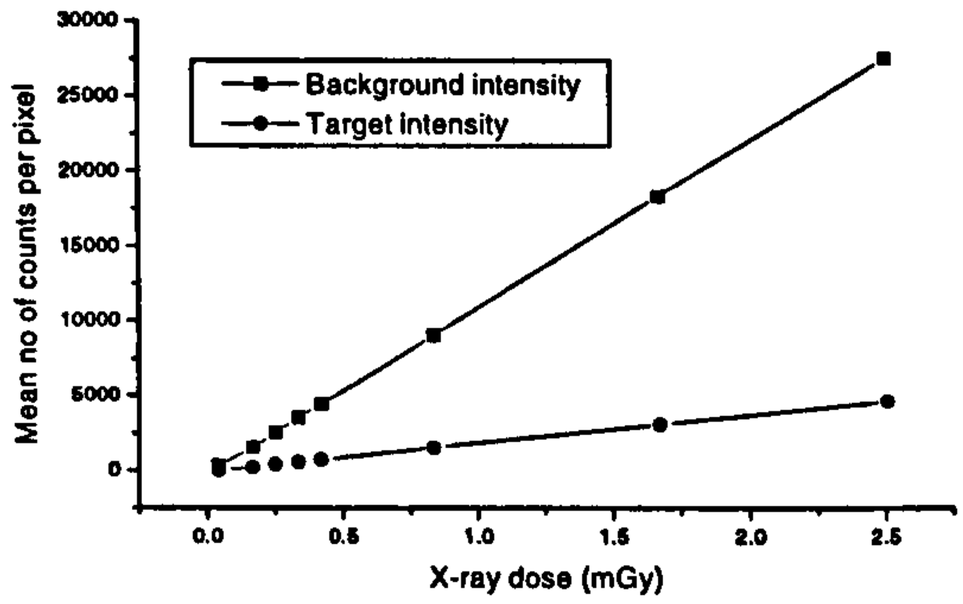

(b) PCD with 300μm silicon

Figure 5.3: Dose response of both systems for the target region (tooth root), and the background.

region is the adjacent area where there is no absorber present. The response is linear for the PCD across the dynamic range, except for a small region near the origin (below about 0.3 mGy) where the timing of the X-ray tube output flux may be more prone to error, giving a slight increase in statistics as we go to the lowest possible exposure length. The Sens-a-Ray response is a characteristic curve similar to a film/screen response, with the background region saturating at about 1 mGy. A "zero dose" response measurement is not possible due to the radiation induced triggering mode of the Sens-a-Ray.

5.3.1 Contrast ratio

The contrast ratio for the tooth phantom was calculated (using equation 2.17) across the useful dynamic range. Figure 5.4 shows that the photon counting detector provides a constant contrast of around 82% across the whole dynamic range, apart from the region below 0.3 mGy where the X-ray tube timing errors appear to provide a bigger flux than expected. The Sens-a-Ray system shows a peak contrast of 71% at 0.4 mGy, with rapid degradation at higher doses due to background pixel saturation. The contrast also falls off at low dose because of the non-linear response of the CCD. The

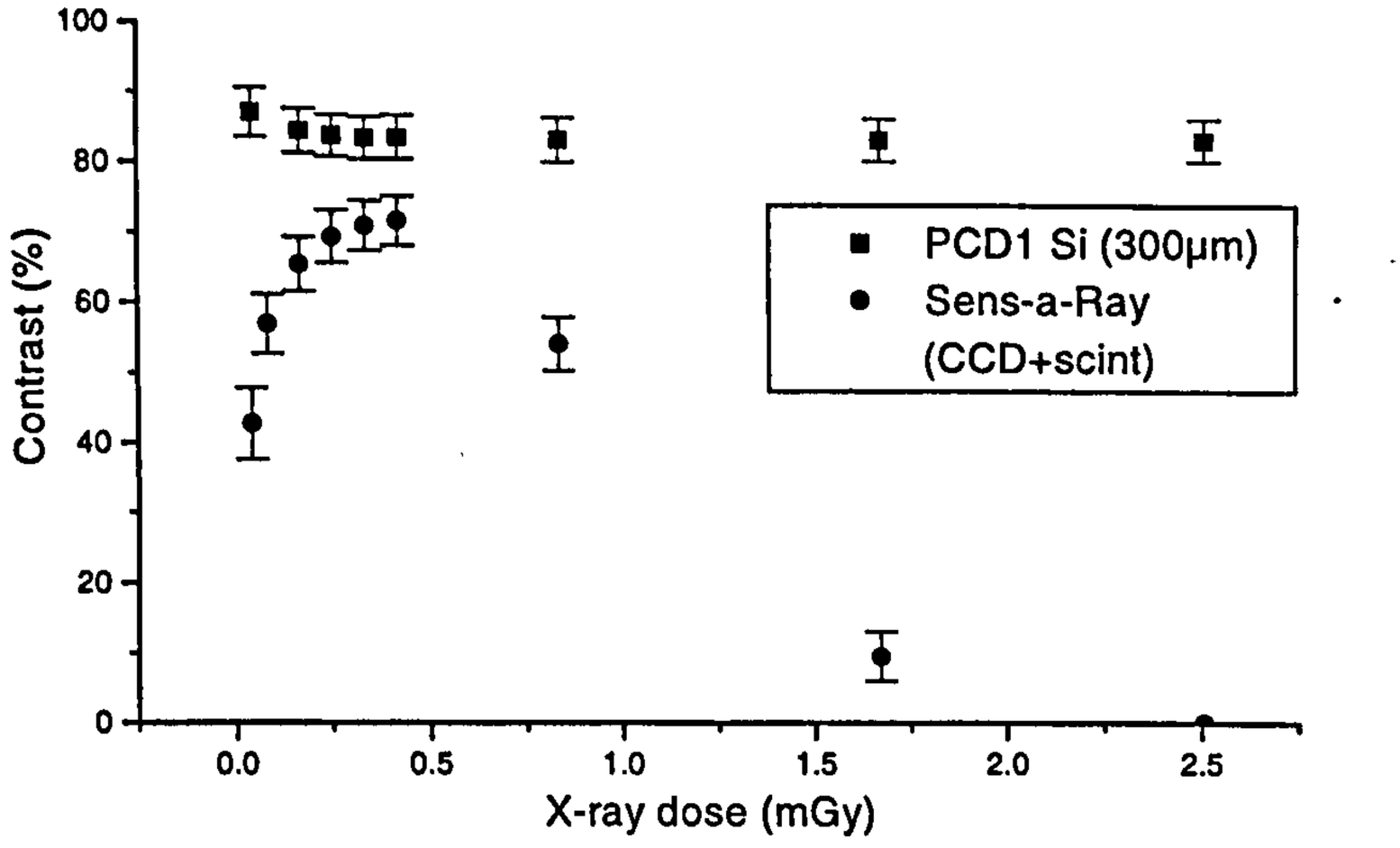

Figure 5.4: Contrast ratio for the PCD (squares) and the Sens-a-ray (dots).

photon counting detector does not reset its counters until after 5 mGy, which is beyond the dose required for dental radiography, however measurements made at this exposure provide the same contrast as those taken at low dose.

5.4 SNR across dynamic range

Flood SNR

The Sens-a-Ray readout provides advanced filtering techniques to smooth the image and improve the noise response. This leads to a noise level in the image that is better than the noise expected from quantum fluctuations. By applying a median filter to the PCD images in a similar fashion, one may improve the noise to beyond this level and compare the signal-to-noise ratio for both systems under the same conditions. Figure 5.5 shows the SNR for both systems from 0 to 2.5 mGy for the background region using the flood image definition of SNR. The target area was not considered as the root section contains material of different densities which make the noise levels worse.

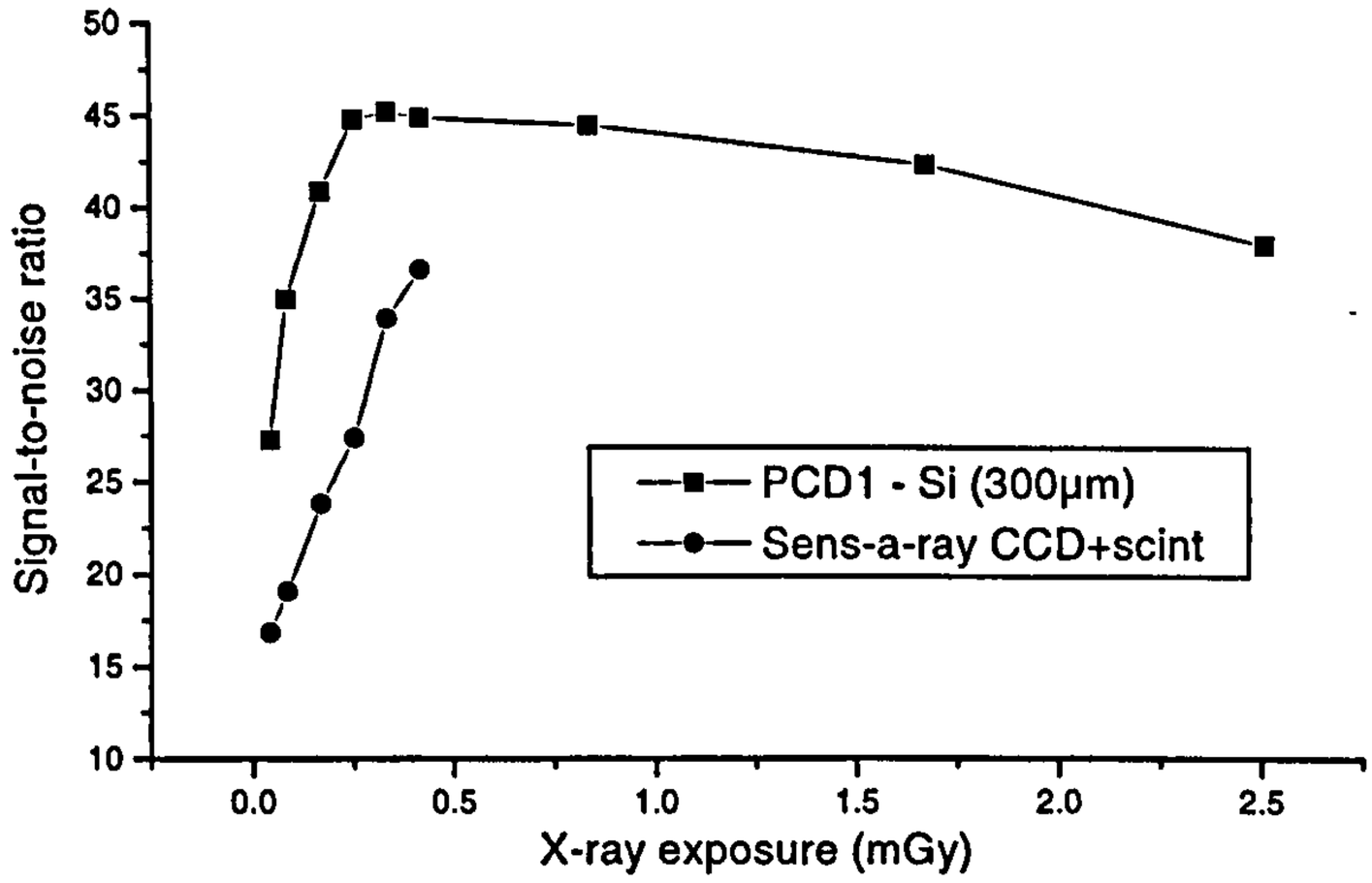

Figure 5.5: Signal to noise ratio for the PCD (squares) and the Sens-a-Ray (dots). SNR is defined for the background region using the flood image equation.

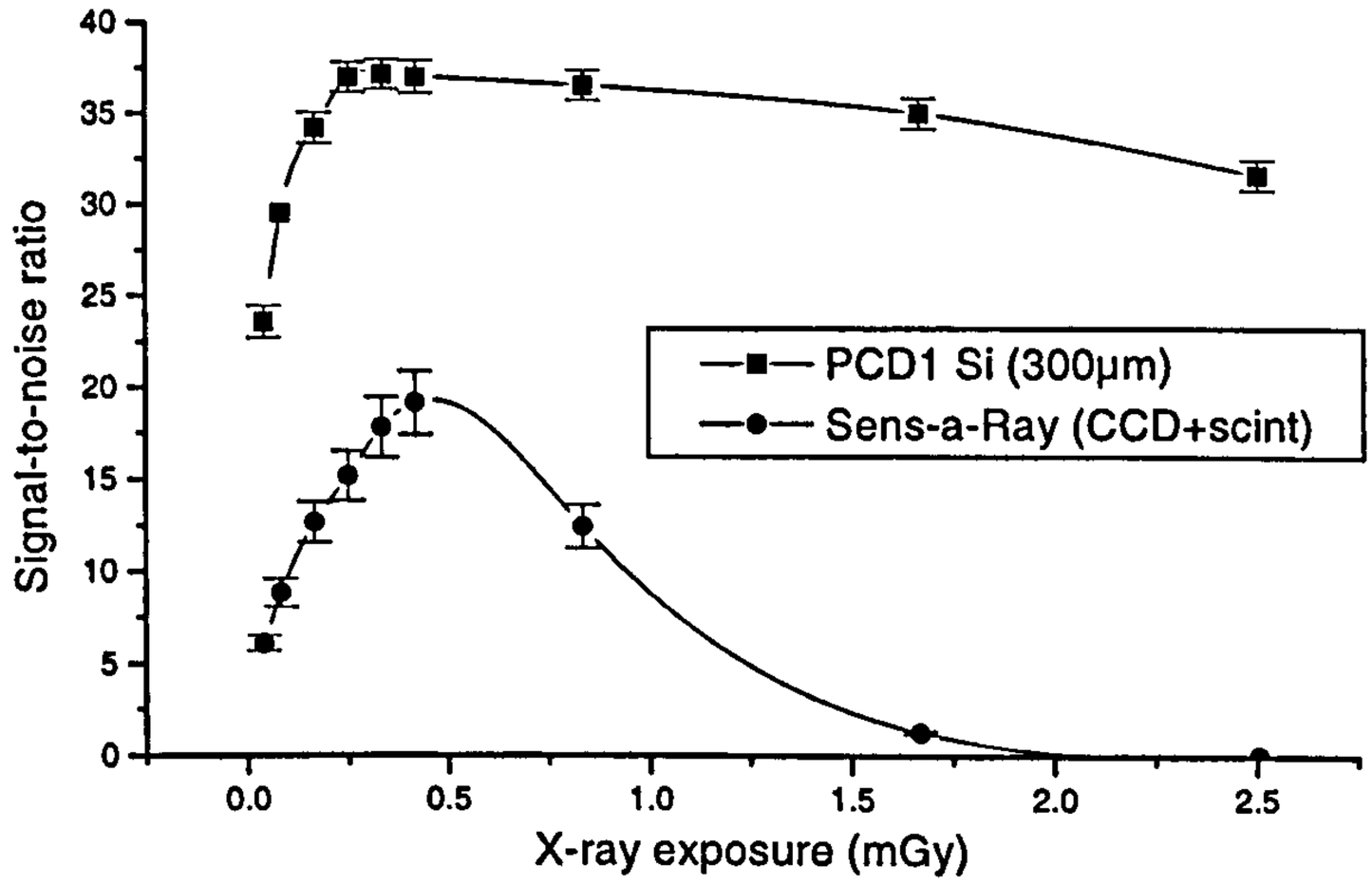

Figure 5.6: Signal to noise ratio for the PCD (squares) and the Sens-a-Ray (dots). The SNR is determined using the definition in equation 2.20.

The Sens-a-Ray shows a linear increase in SNR with dose, as expected, but saturates at 0.5 mGy. The PCD shows a higher SNR than the Sens-a-Ray at every exposure level, and indeed a linear response up to a value of 46 at 0.4 mGy before dropping slightly at higher doses. This sensitometric response is seen every time the PCD is illuminated with a high flux of photons, and may be a property of the X-ray tube or the readout electronics. The Sens-a-Ray saturates above this point, so is not seen to be susceptible to this phenomenon.

Object SNR

Using the definition given in equation 2.20, figure 5.6 shows the SNR for the tooth phantom as a function of dose. The Sens-a-Ray response is still above the acceptable threshold (SNR = 5) up to about 0.5 mGy, but gradually drops to zero as the sensor saturates. The PCD response is similar to the flood SNR of figure 5.5, and is well above the threshold criterion at all exposure levels. Note the values of SNR are lower using the object SNR definition (equation 2.20) as all imaged objects will scatter the incident radiation and increase the noise levels. These results demonstrate the superior dynamic range of the photon counting system and show a higher SNR for low dose.

5.4.1 Low contrast object imaging

A comparison of the contrast as a function of dose was made with a mammographic CDMAM-phantom plate [73] which consists of an aluminium base with gold discs of diameters 0.10 mm to 3.20 mm and thicknesses 0.05 μm to 1.60 μm. The discs are arranged in a matrix of 16 rows and 16 columns, with logarithmically increasing thickness across the rows and logarithmically increasing diameter across the columns. Each cell contains two identical discs, one in the centre and one in a randomly chosen corner.

Figure 5.7 shows the contrast achieved with both systems at four different gold disc thicknesses. An image was made of each cell using the two systems and the discs located in the image. After the application of a 3 x 3 median

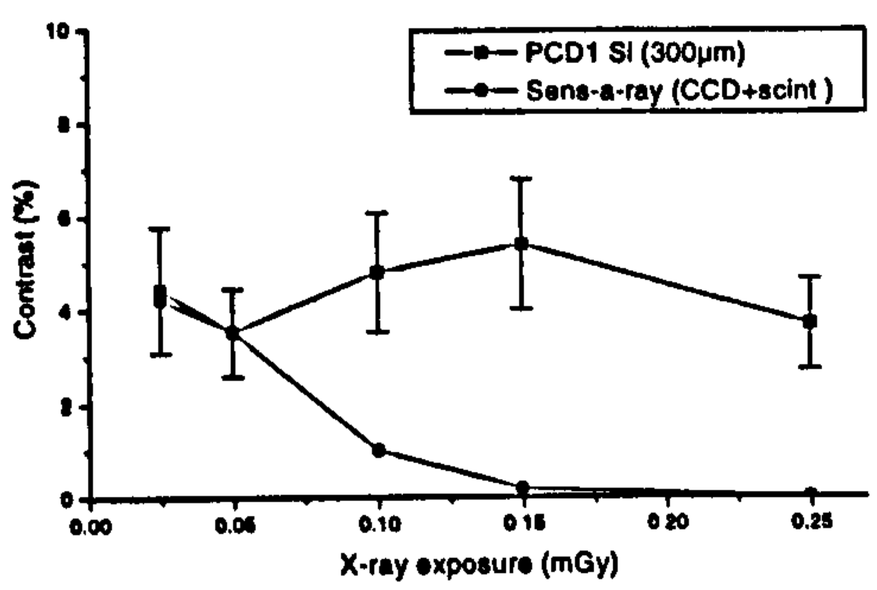

(a) 0.50μm thick

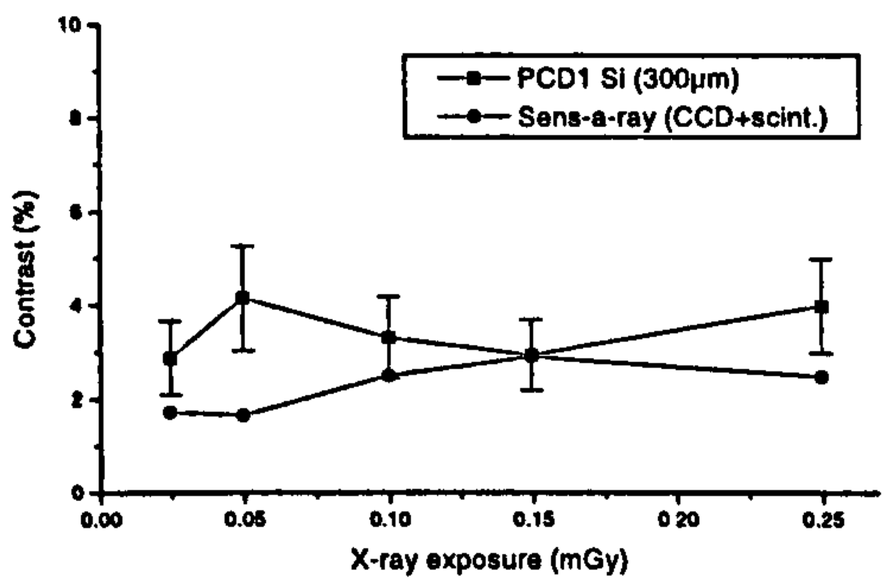

(b) 1.00μm thick

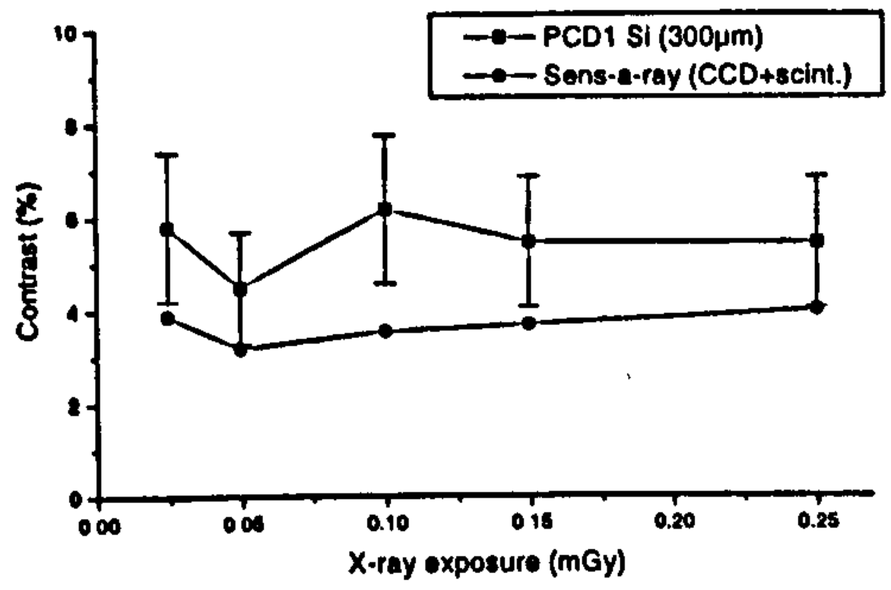

(c) 1.25μm thick

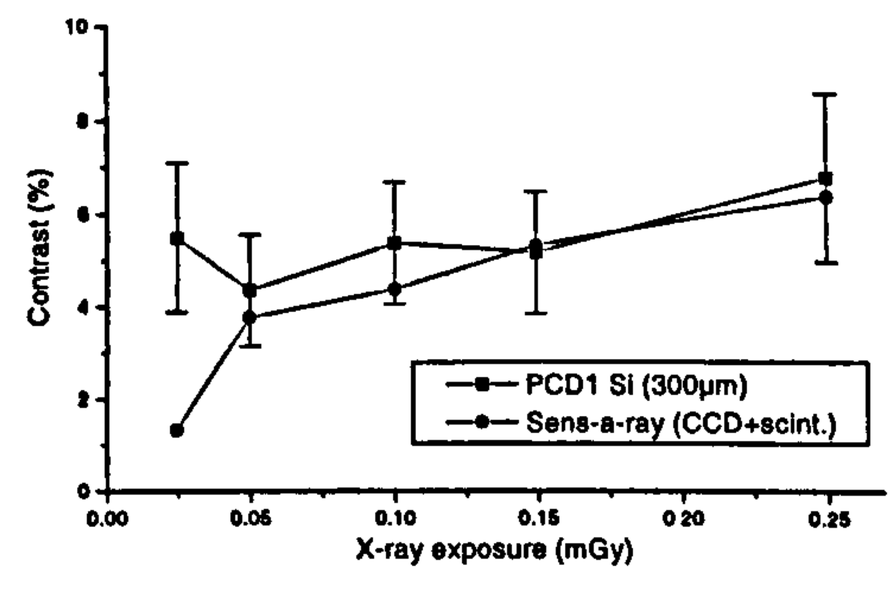

(d) 1.60μm thick

Figure 5.7: Contrast achieved with different thicknesses of phantom gold disc as a function of dose. The error in the Sens-a-Ray measurement is not visible on this graph due to the higher number of pixels counting the gold disc regions.

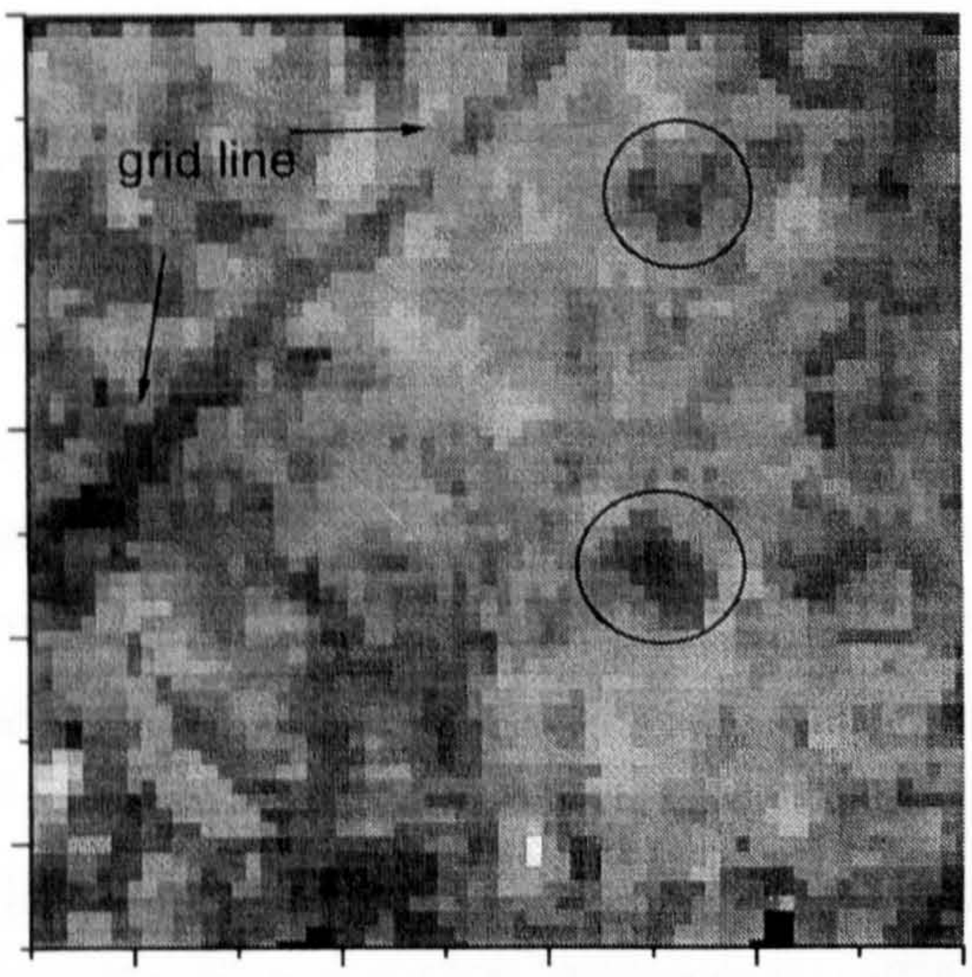

Figure 5.8: Image of the 1.25μm thick (1mm diameter) gold discs of the mammography phantom cell taken with the PCD at 0.25 mGy (60kVp). The gold discs are marked with circles, and the grid line separators are also visible.

filter, the mean number of counts within the disc areas were calculated. Since the disc size is very small compared to the sensor area, the background region was taken to be the whole sensor. The error in the PCD system is quite large, possibly due to pick up from the X-ray tube firing and also the small size of the discs, however the contrast is typically higher for the PCD than the Sens-a-Ray. Figure 5.8 shows the PCD image obtained with a pair of 1.25μm thick gold discs. The two discs are marked with circles, and the grid lines separating adjacent phantom cells are also visible. It can be seen in figure 5.7(a) that the PCD manages to retain contrast at 0.5μm thickness, whereas the Sens-a-Ray measured contrast quickly drops to zero, due possibly to saturation at such a low object contrast (i.e. almost a flood image). The two systems however show comparable contrast at larger disc thicknesses.

In general, the contrast values measured are very low. The mammographic phantom is optimised for 20kVp X-rays, so we can assume there is a contribution from the higher energy photons (more than 15keV) which is degrading the contrast values. The poor spatial resolution of the PCD1 make it difficult to measure a significant amount of pixels below the gold discs, hence the large error bars. This may also account for the Sens-a-Ray showing a more uniform response for higher disc thicknesses. A K X-ray source (Ag) was used to attempt to image the phantom with no success. An X-ray exposure of a matter of days may be needed per disc to acheive reasonable statistics.

5.4.2 Bar/space test pattern imaging

The lowest dose possible with the X-ray gun is 1.8mR (15.6μGy). A bar/space pattern [74] with lead bars at increasing spatial frequency was imaged with both systems at this dose, as shown in figure 5.9. The Sens-a-Ray shows a maximum contrast between light and dark of about 4 gray levels, with good spatial resolution. The PCD shows a higher contrast (over 300 counts) at poorer spatial resolution due to the large pixel size.

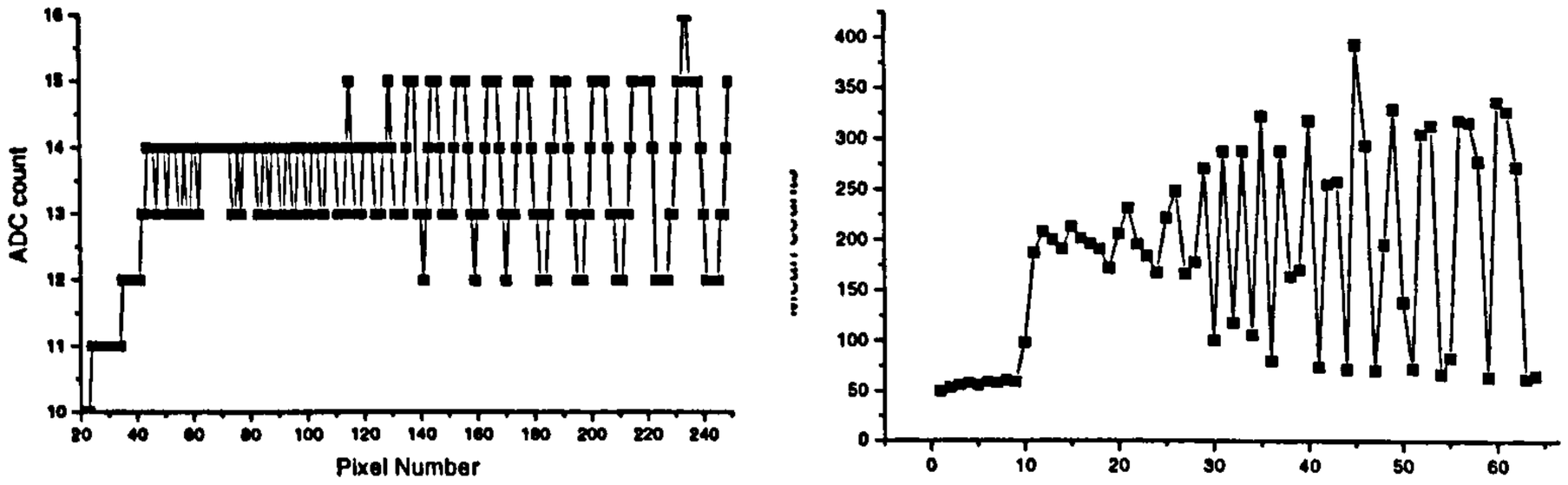

(a) Sens-a-Ray profile

(b) PCD profile

Figure 5.9: Response of both systems to a bar/space pattern with increasing spatial frequency.

5.5 Remarks

The complex, onboard logic of CMOS active pixel sensors has allowed single photon counting devices to be realised. The theoretical advantages in terms of SNR and contrast improvements have been discussed. A comparison between two systems operating under two different detection modes has been made, and while it is not a direct, quantitative comparison of the two methods, it demonstrates experimentally the motivation behind the implementation of single photon counting as a preferred radiation detection method for soft X-rays.

Chapter 6

Conclusions

A single photon counting hybrid semiconductor pixel detector has been presented in this thesis as an alternative to current technology for low dose, low energy X-ray imaging such as diagnostic radiology and synchrotron applications. The device has been realised from work done by the CERN RD-19 collaboration for the ATLAS detector at the LHC. The detector comprises a pixellated CMOS readout chip with active pixel logic bump-bonded to a reverse biased semiconductor diode. The readout chip senses electron-hole pairs generated by incident radiation in the semiconductor, and this signal is shaped and counted by a scaler provided the signal is above an externally set threshold. This threshold allows Compton background to be excluded, allowing certain types of energy-dependent radiology such as subtraction angiography to be performed. The separate optimisation of detector and readout chip allows different semiconductors to be used as a detection medium, and the leakage current insensitive threshold means effectively no dark current, resulting in better contrast at low dose.

The Photon Counting Chip (PCC1) is a 64x64 matrix of square photon counting pixels of side 170μm. The chip provides detector leakage current compensation and a 3-bit threshold fine tune. Each pixel contains an input from the detector bump-pad and an external input through a test capacitor. To measure the performance of the PCC1, a pulse generator was used to

inject signals into each pixel, in this case, 1000 test pulses of varying height. The minimum threshold achieved is 1400e- (5.1keV in Si) with a variation of 350e-. The variation of 350e- was improved to 80e- with the application of the 3-bit threshold fine-tune. The chip was pulsed at a speed of up to 2MHz with no loss of performance, and the ENC (dominated by the comparator noise) was measured to be 170e-.

The PCC1 has been successfully bump-bonded to detectors fabricated on silicon and SI-LEC GaAs. The I-V characteristics show the SI-LEC GaAs breaking down between 200 and 250V with a leakage current of about 5μA. The silicon device operates at 80V with a leakage current of about 200nA. The presence of a SI-GaAs detector moves the minimum threshold up to over 20mV (2300e-), whereas the silicon detector has a much smaller effect due to the low noise of the reverse biased junction. The absolute value of test input capacitance was measured with a Ag K X-ray source (22keV) for a silicon detector as 10fF, which is low compared to the CERN measured value of 24.7fF for a SI-GaAs detector. A detection efficiency of 49% was measured for the SI-GaAs detector at 20mR (160μGy) compared with 28% for silicon, with the low absorption efficiency of silicon above 20keV explaining the drop in statistics.

The fixed pattern noise of a SI-GaAs detector was measured, with a signal-to-noise ratio of 6.7 in a flood image. Using a gain map correction algorithm, this SNR was improved to 13.5, meaning some of the material inhomogeneities inherent in GaAs may be compensated for. Areas of a partly damaged GaAs detector were observed to be working with noise levels close to the quantum noise limit. An MTF of 4.4 lp/mm at the 30% level was measured by the Freiburg group.

Wafer probing studies prior to device assembly show that the classification of readout chips is highly dependent on probe card contact height, which may have resulted in rejection of good chips. Bump-bonding technology is still offered by few companies, but with improving yields.

To investigate other applications of hybrid pixel detector technology, the

PCD was used to observe the powder diffraction pattern obtained from a potassium niobate sample illuminated with a synchrotron radiation source (Daresbury Lab., UK). A comparison was made between the existing scintillator laboratory setup, the PCD (SI-LEC GaAs) and previous results obtained in an identical experiment using the Omega3 detector. To demonstrate large area imaging, the PCD measured a 20keV XRD pattern over 10^o in 0.3^o steps compared to the 0.01^o step required for the scintillator. This resulted in a factor of 5 improvement in the pattern acquisition speed. The profile of the triple peak in the diffraction pattern compared in terms of peak-to-valley ratio show the Omega3 detector resolving the peaks best, due to the high spatial resolution of one dimension of the pixel geometry. The PCD yielded similar peak resolution to the scintillator. A loss of statistics was observed using the 20keV beam which is attributed to a drop in the absorption cross-section at 17keV, corresponding to the K-edge absorption energy for niobium.

The PCD offers improvements in acquisition speed and image step size, however the spatial resolution places a limit on the narrowest observable peak. The MEDIPIX2 chip at 55 μm pitch will allow finer detail to be resolved.

The CCD based technology of modern digital imaging systems operates in charge integrating mode. Charge integrating devices suffer from non-linear response, blooming at high dose and leakage current background "fog" at low dose. A qualitative mathematical treatment of the properties of photon counting and integrating is formulated, with photon counting offering improved image quality in terms of signal-to-noise ratio and object contrast. Using a commercial dental X-ray sensor (the Sens-A-Ray) as a typical charge integrating device, a comparison was made between the photon counting PCD and the Sens-A-Ray illuminated by a commercial X-ray tube operating at 60kVp. The PCD shows a linear response across the whole dynamic range in terms of intensity, signal-to-noise ratio (maximum 45 for a flood image) and object contrast (82% for a molar root phantom). A mammo-

graphic phantom was imaged to investigate low contrast response. The PCD showed slightly higher contrast values than the Sens-A-Ray, but with larger errors due to the small amount of pixels covering the phantom disc regions. Overall, the PCD is seen to give overall a more linear response at very low doses, which is desirable for medical imaging.

The MEDIPIX2 chip will address the shortcomings of the PCC1 chip, the biggest improvements being spatial resolution (55μm), 3-side buttable chips (for large area tiled images) and negative signal sensitivity at the readout chip, allowing more efficient materials such as CdZnTe to be used for low noise, high efficiency digital imaging.

The future and MEDIPIX2

The MEDIPIX collaboration has expanded to 13 institutions across Europe based on the success of the PCC1 chip and subsequent assemblies. The PCC2 (or MEDIPIX2) will offer the following advantages over the PCC1:

- A pixel size of 55μm $\times$ 55 μm.
- A matrix of 256 $\times$ 256 pixels per chip.
- Deep submicron CMOS process (0.25μm).
- Lower AND upper threshold window (2 comparators).
- Sensitive to positive AND negative signal (more choice of material, particularly CdZnTe).
- Leakage current compensation addressable on a pixel-by-pixel basis to compensate for material inhomogeneities.
- Increased comparator range will provide a linear response across a larger range of energies. This allows the same threshold mask to be applied at different global threshold settings.
- 13 bit counter with overflow bit (almost double the dynamic range of PCC1).
- 3-side buttable (chips may be tiled together to increase area).

This thesis has presented some of the properties and shortcomings of the PCC1 which have formed some of the motivations for the new PCC2 readout chip. With the use of high quality materials such as CdZnTe and EPI-GaAs, the efficiency of the device across a broader X-ray range is a promising possibility. The potential of single photon counting arrays is huge and may find new applications in more diverse fields in industry, such as radioactive source monitoring and digital cameras, where CCDs and charge integration are still the standard technology.

List of publications

As author:

- "Applications of pixellated GaAs X-ray detectors in a synchrotron radiation beam" *Nucl. Instr. and Meth. in Phys. Res.* **A460** (2001) 185-190 *Presented at 1st International Workshop on Radiation Imaging Detectors, Sundsvall, Sweden 13th-17th June 1999.*

- "Photon counting vs. charge integration - experimental studies with a GaAs hybrid pixel detector" *submitted to NIMA. Presented at 2nd International Workshop on Radiation Imaging Detectors, Freiburg im Breisgau, Germany, 2nd-6th July 2000.*

As contributer:

- "X-ray imaging with photon counting hybrid semiconductor detectors" *Nucl. Instr. and Meth.* **A434** (1999) pp. 38-43 *Presented at 6th International Workshop on Gallium Arsenide Detectors and Related Compounds, Praha-Průhonice, Czech Republic, June 22nd-26th 1998.*

As co-author:

- "Performance of a 4096 pixel photon counting chip" *Proc. SPIE* **Vol. 3445** (1998) 298-304.

- "X-ray imaging using a hybrid photon counting GaAs pixel detector" *Nucl.Physics B (Proc.Suppl.)* **78** (1999) 491-496.

- "Characterisation of a single photon counting pixel system for imaging of low contrast objects" *Nucl. Instr. and Meth. in Phys.Res.* **A458** (2001) 352-359.

- "Dose-dependent X-ray measurements using a 64x64 hybrid GaAs pixel detector with photon counting" *Nucl. Instr. and Meth. in Phys.Res.* **A460** (2001) 91-96.

- "Measurements with Si and GaAs pixel detectors bonded to photon counting readout chips" *submitted to NIMA. Presented at 2nd International Workshop on Radiation Imaging Detectors, Freiburg im Breisgau, Germany, 2nd-6th July 2000.*

Bibliography

[1] A.M. Litke, "An advanced pixel detector" *Nucl. Instr. and Meth.* **A386** (1997) 167-171

[2] H. Geiger and A. Werner, *Z. Physik* **21** (1924) 187

[3] E. Rutherford, "Radiations from Radioactive Substances" *Cambridge University Press, 1930* pp. 548-549

[4] A. Breskin, "Photon detectors for the 21st century" *Nucl. Instr. and Meth.* **A387** (1997) 1-18

[5] S. Webb, "The Physics of Medical Imaging" *Institute of Physics Publishing* 1988

[6] C. Da Via', "Semiconductor pixel detectors for imaging applications" *PhD Thesis* University of Glasgow, Glasgow and CERN, Geneva (1997)

[7] M. Caria, "Current trends on design and assembly of pixel detector systems in biomedicine and high-energy physics" *Nucl. Instr. and Meth.* **A447** (2000) 167-177

[8] "ATLAS Technical Proposal" *CERN/LHCC/94-43* 15 December 1994

[9] "Use of pixel detectors in elementary particle physics" *Nucl. Instr. and Meth.* **A305** (1991) 497-503

[10] G.F. Knoll, "Radiation Detection and Measurement" (3rd Edition) *John Wiley and Sons* pp. 497-501

[11] M. Campbell et al., "A 10MHz micropower CMOS front end for direct readout of pixel detectors" *Nucl. Instr. and Meth.* **A290** (1990) 149

[12] E. Fossum, "CMOS active pixel image sensors" *Nucl. Instr. and Meth.* **A395** (1997) 291-297

[13] M. Campbell et al., "Development of a pixel readout chip compatible with large area coverage" *Nucl. Instr. and Meth.* **A342** (1994) 52

[14] G. Humpston et al., "Advanced flip-chip solder bonding" *Nucl. Instr. and Meth.***A395** (1997) 375-378

[15] E.H.M. Heijne et al., "R & D proposal: Development of hybrid and monolithic silicon micropattern detectors" *CERN Internal Report* **CERN DRDC/90-81** 15 December 1990

[16] E.H.M. Heijne et al., "The silicon micropattern detector: a dream?" *Nucl. Instr. and Meth.* **A273** (1988) 615-619

[17] L.H.H. Scharfetter, "Active Pixel Detectors for the Large Hadron Collider" *PhD. Thesis* Leopold Franzens University, Innsbruck, Austria and CERN, Geneva, Switzerland (1997)

[18] S.M. Sze, "Semiconductor Devices: Physics and Technology" *John Wiley and Sons* Chapter 1

[19] S.M. Sze, "Physics of Semiconductor Devices" *John Wiley and Sons* (1981) Chapter 1

[20] W. Shockley, "Electrons and Holes in Semiconductors" *D. Van Nostrand inc.* (1950) pp. 67-69

[21] S. Ramo, "Currents Induced by Electron Motion" *Proceedings of the I.R.E.* September 1939 pp.584-585

[22] G. Cavalleri, "On the induced charge in semiconductor detectors" *Nucl. Instr. and Meth.***21** (1963) 177-178

[23] J.C. Bourgoin et al., "Native defects in gallium arsenide" *J. Appl. Phys.* **64** (9) Nov 1988

[24] G.F. Knoll, "Radiation Detection and Measurement" (2nd Edition) *John Wiley and Sons* pp. 435

[25] R. Adams, "Growth of high purity GaAs using low-pressure vapour-phase epitaxy" *Nucl. Instr. and Meth.* **A395** (1997) 125-128

[26] R. Adams, "Preliminary results for LP VPE X-ray detectors" *Nucl. Instr. and Meth.* **A395** (1997) 129-131

[27] A. Meikle (private communication) *University of Glasgow, Glasgow, UK.* August 1998

[28] A. Workman and D.S. Brettle, "Physical performance measures of radiographic imaging systems" *Dentomaxillofacial Radiology* **Vol. 26** (1997) pp. 139-146

[29] C. Fröjdh and P. Nelvig, "Performance criteria for x-ray imaging sensors" *Physica Medica* **Vol. XIV** Supplement 2, Sept. 1998 pp. 10-12

[30] "Medical Imaging - The Assessment of Image Quality" *International Commission on Radiation Units and Measurements* **ICRU Report 54** pp. 11-13

[31] "Modulation Transfer Function of Screen-Film Systems" *International Commission on Radiation Units and Measurements* **ICRU Report 41** pp. 6

[32] U. Welander et al., "Basic technical properties of a system for direct acquisition of digital intraoral radiographs" *Oral Surg Oral Med Oral Pathol* **Vol. 75** (1993) pp. 506-516

[33] R. Irsigler et al., "X-ray Imaging Using a 320 x 240 Hybrid GaAs Pixel Detector" *IEEE Trans. Nucl. Sci.* **46** (1999) 507-512

[34] V. Kaftandjian, "A Comparison of the Ball, Wire, Edge, and BAr/Space Pattern Techniques for Modulation Transfer Function Measurements of Linear X-Ray Detectors" *Journal of X-ray Science and Tech.* **6** (1996) pp. 205-221

[35] S. Manolopoulos, "Modulation Transfer Function" *internal document - PPE Group, University of Glasgow* (1996)

[36] U. Welander et al., "Absolute measures of image quality for the Sens-a-Ray direct digital intraoral radiography system" *Oral Surg Oral Med Oral Pathol* **Vol. 80** (1995) pp. 345-350

[37] J. Sandrik and R. Wagner, "Absolute measures of physical image quality: Measurement and application to radiographic magnification" *Med. Phys.* **Vol. 9(4)** July/Aug 1982 pp. 540-549

[38] **Faselec AG**(subsidiary of Philips Electronics), Binzstrasse 44, 8045 Zurich, Switzerland

[39] C. Schwarz et al., "X-ray Imaging Using a Hybrid Counting GaAs Pixel Detector" *Nuclear Physics B (proc. suppl.)* **78** (1999) 491-496

[40] "Medipix Specifications" *CERN internal document* January 1997

[41] Horowitz and Hill, "The Art of Electronics" *Cambridge* (1980) pp. 438

[42] M. Campbell et al., "A readout chip for a 64×64 pixel matrix with 15-bit single photon counting" *IEEE Trans. Nucl. Sci.* **45** (1998) 751-754

[43] S. Stumbo et al., "MEDIPIX: a VLSI chip for a GaAs pixel detector for digital radiology" *Nucl. Instr. and Meth.* **A422** (1999) 201-205

[44] S.R. Amendolia et al., "Medipix Readout Software (MEDISOFT)" *C language and LabWindows code* **INFN Napoli** (May 1997)

[45] "MRS VME board", INFN Pisa and LABEN S.p.A., S.S. Padana Superiore 290, 20090 Vimodrone (Milano), Italy

[46] G. Bardelloni et al., "MEDIPIX-1 re-Usable Read Out System (MUROS1)" *NIKHEF, Dept of Electronics Technology, PO Box 41882, Amsterdam* March 2000

[47] Planmeca Prostyle Intra, PLANMECA Oy, Helsinki, Finland

[48] C. Fröjdh, "Photon flux to Roentgens" *XIMAGE internal document*

[49] S. Manolopoulos et al., "X-ray imaging with photon counting hybrid semiconductor detector" *Nucl. Instr. and Meth.***A434** (1999) pp. 38-43

[50] B. Mikulec, "Single Photon Detection with Semiconductor Pixel Arrays for Medical Imaging Applications" *PhD. Thesis***CERN-THESIS-2000-021** CERN, Geneva, Switzerland. June 2000

[51] E.H.M. Heijne et al., "LHC1: A Semiconductor Pixel Detector Readout Chip with Internal, Tunable Delay Providing a Binary Pattern of Selected Events" *Nucl. Instr. and Meth.***A383** (1996) pp. 55-63

[52] E. Pernigotti et al., "Performance of a 4096 Pixel Photon Counting Chip" *Proc. SPIE* **Vol. 3445** (1998) 298-304

[53] M. Alietti et al., "Performance of a New Ohmic Contact for GaAs Particle Detectors" *Nucl. Instr. and Meth.* **A362** (1995) 344-348

[54] Variable Energy X-ray Source 4352LV (10mCi, 370MBq, Am241), *Amersham International plc, Little Chalfont, Buckinghamshire, UK*

[55] B. Mikulec et al., "Characterisation of a single photon counting pixel system for imaging of low-contrast objects" *submitted to NIM, 2000*

[56] C. Fröjdh, "Criteria for evaluation of sensor prototypes in the XIMAGE-project" *Internal Report, REGAM* **1999-02-11**

[57] R. Irsigler et al., "Gain and offset compensation for 320x240 GaAs X-ray Imaging Pixel Detectors" *submitted to NIM, 2000*

[58] C. Schwarz et al., "Comparison of hybrid GaAs and Silicon pixel detectors bonded to photon counting chips" *Presented at 2nd International Conference on Radiation Imaging Detectors, Freiburg, July 2000* Submitted to NIMA.

[59] R. Irsigler et al., "Evaluation of 320x240 pixel LEC GaAs Schottky barrier X-ray imaging arrays, hybridized to CMOS readout circuit based on charge integration" *Nucl. Instr. and Meth.* **A434** (1999) 24-29

[60] S. Manolopoulos et al, "X-ray powder diffraction with hybrid semiconductor pixel detectors" *Journal of Synchrotron Radiation* **6** (1997) 112-115

[61] "An Introduction to Synchrotron Radiation" *Australian Synchrotron Research Program* http://www.ansto.gov.au/natfac/asrp4.html December 2000

[62] F.A. Dilmanian et al., "Computed tomography of x-ray index of refraction using the diffraction enhanced imaging method" *Phys. Med. Biol.* **45** (2000) 933-946

[63] G.N. Greaves and I.H. Munro, "Synchrotron Radiation Sources and their Applications" *Proc. of 30th Scottish Universities Summer School in Physics* Aberdeen, September 1985

[64] H.P. Myers, "Introductory Solid State Physics" *Taylor and Francis* **(1991)** 61

[65] "Station 9.1 Specifications" *Daresbury Laboratory Web page* http://srs.dl.ac.uk/XRD/9.1/ **July 1996**

[66] J. Watt et al., "Applications of pixellated GaAs X-ray detectors in a synchrotron radiation beam" *Nucl. Instr. and Meth.* **A460** (2001) 185-190 *Proc. of 1st International Workshop on Radiation Imaging Detectors, Sundsvall, Sweden, June 13-17 1999.*

[67] J.H. Hubbell and S.M. Seltzer, "Tables of X-ray Mass Attenuation Coefficients and Mass Energy Absorption Coefficients" http://physics.nist.gov/PhysRefData/XrayMassCoef/cover.html

[68] D. Taeymans, "CMOS v CCD - what we can expect" *Image Processing*October 1997

[69] P. Nelvig, "Sens-A-Ray: A new system for direct digital intraoral radiography" *Oral Surg. Oral Med. Oral Pathol.* **74** (1992) pp. 818-23

[70] E. Pernigotti, "Comparison between integrating readout systems and single photon counting systems for digital mammography" *Physica Medica*Vol.XIV Suppllement 2, Sept. (1998) 20-22

[71] M. Sandborg, "Calculation and analysis of DQE for some image detectors in mammography" *Department of radiation Physics, Linköping University Sweden* **Report 86** (March 1998) ISSN 1102-1799/ISRN ULI-RAD-R–86–SE

[72] M.S. Passmore et al., "Contrast in ideal integrating and photon counting systems" *submitted to NIM A* (2000)

[73] Contrast Detail MAMmography phantom, Department of Diagnostic Radiology, University Hospital Nijmegen, St. Radboud, Netherlands (1988-1992)

[74] Bar/Space pattern No.56, PTW Freiburg, Loerracherstrasse 7, D-79115 Freiburg